Document Version
Final published version

Citation (APA)
Cho, C. (2026). *Luminescent Greenhouse Coating: Investigating the potential of luminescent materials in greenhouse applications*. [Dissertation (TU Delft), Delft University of Technology]. https://doi.org/10.4233/uuid:dc326082-8f39-40ed-aa7d-d30b5e64ced9

LUMINESCENT GREENHOUSE COATING

Investigating the potential of luminescent materials in greenhouse applications

Chun-Ting Cho

Propositions

accompanying the dissertation

Luminescent Greenhouse Coating
Investigating the potential of luminescent materials in greenhouse applications

by

Chun-Ting Cho

1. Food security, defined as “when all people, at all times having physical and economic access to sufficient safe and nutritious food that meets people’s dietary needs and food preferences for an active and healthy life”, makes it impossible to achieve.
2. The agronomic benefits of ambient solar ultraviolet radiation are outweighed by its harmful effects; therefore, UV may be excluded from sunlight and supplied only on-demand through artificial lighting in greenhouses.
This proposition pertains to Chapter 2 of this dissertation.
3. Tuning particle size is more practical for optimizing light scattering than altering refractive index for greenhouse luminescent coatings.
This proposition pertains to Chapter 4 of this dissertation.
4. In Mediterranean greenhouse horticulture, optimising spectral quality is more critical for crop performance than maximising overall light transmittance.
This proposition pertains to Chapter 5 of this dissertation.
5. Hortiscatter metric defined in NEN-2675 is impractical for routine use because its measurement protocol is complex and shows low inter-laboratory reproducibility.
6. Maximizing resource efficiency and yield should come before broad sustainability goals in greenhouses.
7. Trusting intuitive judgments blindly is as flawed as dismissing them entirely.
8. Physics students should undergo more extensive pre-work lab safety training than students from chemistry disciplines, because the standard curriculum of physics disciplines offers less exposure to chemical hazards.
9. "Black tea" is not a "black" tea, but a "red" tea, although it looks "brown".
10. Squats can solve mental issues. If not, do 10 more.

These propositions are regarded as opposable and defendable, and have been approved as such by the promotors prof. dr. P. Dorenbos and dr. E. van der Kolk.

Luminescent Greenhouse Coating

Investigating the potential of luminescent materials in greenhouse applications

Luminescent Greenhouse Coating

Investigating the potential of luminescent materials in greenhouse applications

Dissertation

for the purpose of obtaining the degree of doctor
at Delft University of Technology,
by the authority of the Rector Magnificus Prof.dr.ir. H. Bijl,
chair of the Board of Doctorates,
to be defended publicly on
Friday 13th of March 2026 at 12:30 o'clock.

by

Chun-Ting CHO

Master of Science in Advanced Materials and Processes,
Friedrich-Alexander-Universität Erlangen-Nürnberg, Nürnberg, Germany,
born in Tainan, Taiwan.

This dissertation has been approved by the promotors.

Composition of the doctoral committee:

Rector Magnificus,	chairperson
Dr. E. van der Kolk,	Delft University of Technology, promotor
Em. Prof. dr. P. Dorenbos,	Delft University of Technology, promotor

Independent members:

Prof. dr. F.C. Grozema,	Delft University of Technology
Prof. dr. P. Schall,	University of Amsterdam
Dr. M. Debije,	Eindhoven University of Technology
Dr. S. Hemming,	Wageningen University and Research
Dr. G.B.F. Bosco,	Fotoniq bv, the Netherlands
Prof. dr. ir. A.G. Denkova,	Delft University of Technology, reserve member

Keywords: Spectral conversion coating, hemispherical light transmittance greenhouse, divalent europium, host-absorption phosphor, scattering

Printed by: [Data tbd]

Front & Back: Greenhouses with photosynthetically active radiation.

ISBN [Data tbd]

Contents

1

Introduction

1.1. Food insecurity and solutions

Food insecurity has been a long-lasting topic on the table of the United Nations. Since 1927, the world population has risen from about 2 billion to 8 billion and is expected to continue growing in the coming decades. Thanks to the Industrial Revolution, advanced technology, and public effort, the production of food, such as corn, wheat, and rice, has been enhanced to support the world population. However, according to the 2024 report of the Food and Agriculture Organization of the United Nations, nearly 281 million people are encountering high levels of food insecurity [1]. The reasons are various, for example, waste, poor supply chain, regional conflict, extreme weather, and economic shocks. Among all the reasons, extreme climate conditions account for over 72 million people in 18 countries facing high levels of food insecurity, which was 56 million in 2022. The four critical factors for food security are presented in Fig. 1.1.

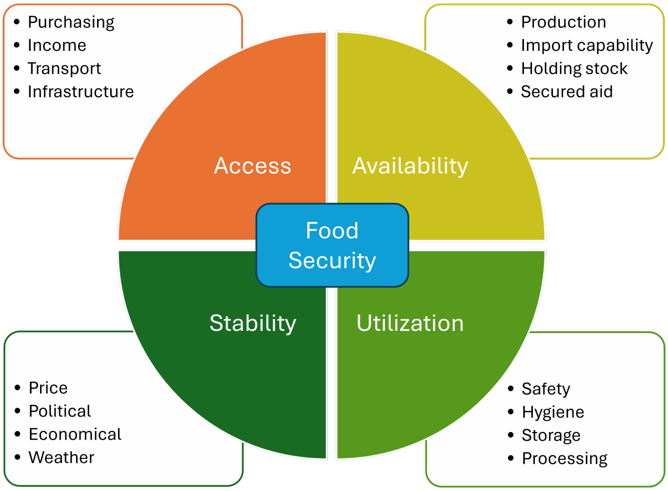

Figure 1.1: The four factors of food security. Figure was reproduced from Carthy et al. [2].

One of the most straightforward ways to address food insecurity for a rapidly expanding global population is to increase crop production. However, current food production systems are already operating under severe stress, and further expansion may not be sustainable because we have over-exploited natural resources; for example, an estimated 17% of the Amazon rainforest has already been degraded [3]. In addition, industrialization, environmental pollution, and climate change are reducing the amount of available land area for agriculture [4, 5]. It is widely acknowledged that food insecurity cannot be solved by a single solution. In response, international organizations have recommended several strategies, including policies to reduce food waste, preserve resources, improve current production, transportation, storage systems, and better communication along the value chain between farmers and end consumers [6].

Several measures are proposed specifically to address the food insecurity arising from climate change. Strengthening the sustainability of agriculture is a major focus, which includes conservation agriculture, crop diversification, and organic farming. Other measures, such as sustainable land management, soilless planting, water conservation, and efficient irrigation techniques can all be helpful for enhancing the resilience of crops to climate change. Lastly, the use of artificial intelligence, big data, and advanced sensor systems can help monitor the growing conditions of crops in real time, providing immediate adjustments for higher crop yields [7–13].

Greenhouses are a promising solution for addressing food insecurity arising from climate change, as they offer a shielded environment that protects crops from extreme weather conditions and provide a higher crop yield compared to open-field farming. There are various types of greenhouses. In tropical regions, the greenhouses are usually built with plastic covers. In northern areas like the Netherlands and England, greenhouses are often made with glass panels, which protect the crops from strong winds, snow, and frost. Apart from providing protection, greenhouses also provide a suitable platform for applying advanced technologies such as precision nutrition control, climate system, pest control, lighting systems, automation, and AI monitoring systems. The various features of greenhouses can help increase crop yields more effectively [14, 15]. Beyond advanced greenhouse technologies, light is important to plant growth because it directly drives photosynthesis and influences crop yield. In greenhouses, “light management” involves regulating the spectral quality, intensity, and duration (photoperiod) of incoming light, along with the optical properties of the glazing and supplemental lighting systems.

1.2. Light management in greenhouses: Spectrum, Transmittance, and Scattering

1.2.1. Air mass spectrum and sunlight trajectory

To establish a unified standard for evaluating solar cell performance, the air mass coefficient system was introduced, abbreviated as “AM” followed by a number. AM0 refers to the solar energy spectrum outside the atmosphere, which means zero atmosphere. AM1 refers to the solar spectrum passing through one atmosphere layer at sea level, which is often used to characterize the performance of solar cells in the tropical and equatorial regions. However, sunlight rarely traverses exactly one atmosphere in all situations.

Sunlight's spectrum varies with weather conditions, as well as the latitude and altitude of the observation point. In the morning and evening, the penetrating path of sunlight is much longer than at noon. Weather conditions, such as sunny or cloudy skies, also influence the air mass. In addition, because the major population of the world lives in the temperate zone, the average term of AM1.5, corresponding to a solar zenith angle of 48.2°, can better represent the average length of sunlight trajectory and is often used in research to characterize the performance of solar cells. Figure 1.2 illustrates the AM0 and AM1.5 solar spectrum reproduced from the data in Gueymard et al. [16]. The Earth orbits the Sun and also rotates on its own axis. As mentioned, the trajectory of sunlight varies according to different latitudes and the altitude of the observation point. Figure 1.3 illustrates that at high-latitude regions like the Netherlands and England, the sunlight never reaches the ground at a perpendicular angle.

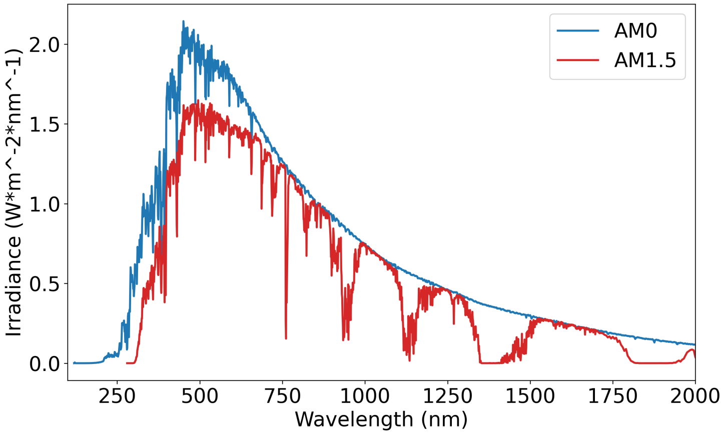

Figure 1.2: The AM0 and AM1.5 solar spectrum.

Beyond photovoltaics, horticulture also relies heavily on the solar spectrum, as sunlight is a free and indispensable resource for plant growth. The two fields draw on many of the same principles. For example, both greenhouse roofs and solar panels are installed at region-specific tilt angles based on the sun's trajectory. In the Netherlands, solar panels achieve the highest power output when oriented south at a tilt angle of about 37°, while greenhouse roofs are often tilted 20–30° to maximize sunlight capture [17].

1.2.2. Hemispherical light transmittance

Because sunlight rarely enters the greenhouse roofs at a perpendicular angle, characterizing the performance of greenhouse roof only with "perpendicular transmittance (or direct transmittance)", which is often used in the physics field and only measured with the light incident at a perpendicular angle (0° angle of incidence), does not accurately reflect real-world conditions. To address this limitation, researchers from Wageningen University and Research introduced the concept of "hemispherical light transmittance (T_{HEM})", which integrates the angular transmittance from 0° to 90° angle of incidences, providing a more comprehensive and accurate method to characterize the transmittance property

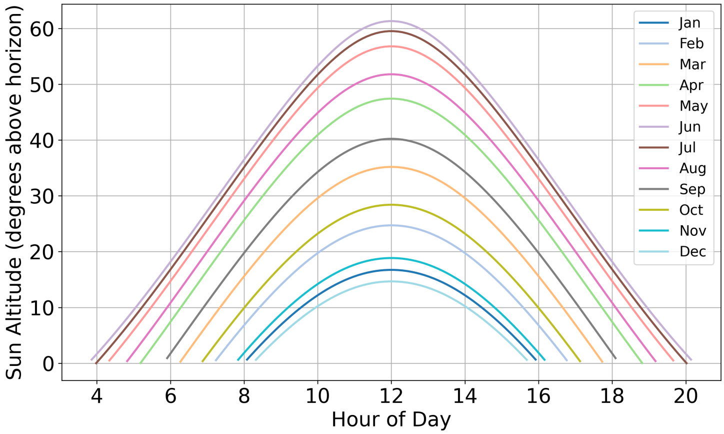

Figure 1.3: The sun trajectory in the high latitude (52°N) region.

of the greenhouse roof materials. Hemispherical light transmittance is considered more representative compared to the direct transmittance for the users in horticulture.

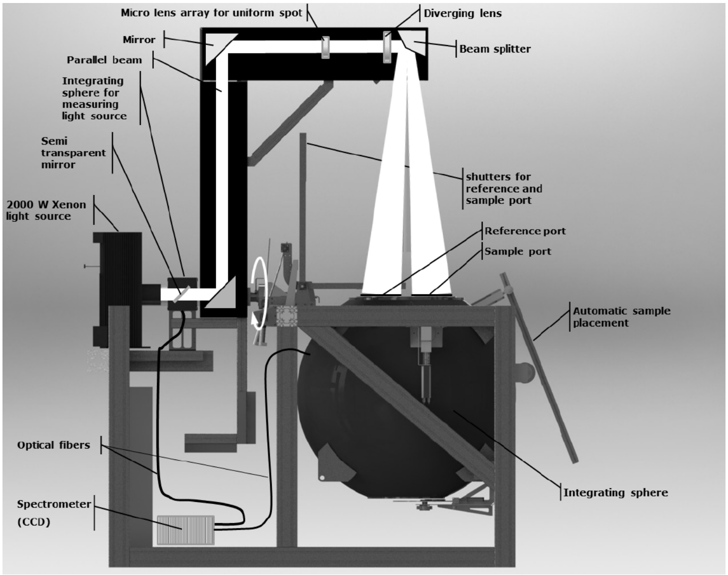

Figure 1.4: WUR Transvision system. Image from Swinkel et al. [19].

The latest procedures and requirements for measuring hemispherical light transmittance are regulated by the Netherlands Normalisatie Instituut in the document NEN-2675-2018 [18]. Currently, there is only one accredited institute (according to Raad voor Accreditatie) that can carry out the measurement of hemispherical light transmittance, with a system called “Transvision” at Wageningen University and Research (WUR) Light

Lab. The system utilizes a high power xenon lamp with two reflective mirrors to split the incident light, and a 1.5 m integrating sphere (with 2 openings) is used as the signal collector, as shown in Fig. 1.4 [19]. The WUR Transvision system is recognized as the industry standard for measuring hemispherical transmittance of greenhouse glazing materials [20]. According to Marcelis et al., 1% extra hemispherical light transmittance enhances 0.5% to 1% extra crop yield [21]. Therefore, the manufacturers and owners of greenhouses significantly value this specific optical property.

1.2.3. Hortiscatter

Besides light transmittance, Dutch plant biologists and growers also value how sunlight is scattered onto leaves. Photosynthesis does not increase linearly with sunlight flux; beyond a certain intensity, additional light does not enhance photosynthesis and effectively goes to waste. In low-scattering conditions, such as on a cloudless day, sunlight enters the greenhouse directly and primarily illuminates the top layers of leaves, causing them to reach photosynthetic saturation while lower leaves receive insufficient light. By increasing the scattering of sunlight, illumination is distributed more evenly, allowing more leaves to operate at optimal photosynthetic efficiency [22–24]. As a result, greenhouse owners often use scattering coatings or specialized roof structures (this dissertation focuses on scattering coatings) to enhance light distribution.

To quantify a covering material's ability to scatter light, researchers introduced the concept of Hortiscatter (S_H), which is defined and regulated under NEN-2675-2018. A 0% S_H means that all transmitted light rays keep their original direction, while a 100% S_H means that the scattering distribution of the light rays follows a perfect Lambertian distribution. In the case of a Lambertian scattering, an observer looking at the scattering source from a fixed distance, perceives constant brightness, i.e., the radiance is constant, from all possible viewing angles. The hortiscatter indicates the extent to which a scattering distribution resembles Lambertian scattering. According to Wageningen University & Research (WUR), a Hortiscatter level of about 10% can boost crop yield by approximately 1.8 - 2.2% [25]. However, increasing scattering often lowers overall light transmittance (T_{HEM}), as some incident light is reflected outwards. Our ray tracing monte-carlo simulation shows that as particle size increases from a few nanometers to a few micrometers, T_{HEM} rises while S_H decreases, revealing a trade-off that makes it difficult to maximize both simultaneously (Figure 1.5). Although NEN-2675-2018 specifies procedures for measuring S_H, there is currently no reliable system that can measure this parameter consistently, so Hortiscatter is not investigated further in this dissertation.

1.3. Light-driven plant physiology: PAR, UV, and NIR

1.3.1. Photosynthesis effect and photosynthetically active radiation (PAR)

Plants require light, carbon dioxide, water, and nutrients for photosynthesis and growth. Through photosynthesis, CO_2 is converted into organic compounds, contributing to biomass accumulation and, under certain conditions, to carbon sequestration. The energy from sunlight is primarily absorbed by chlorophyll, a specialized pigment found in

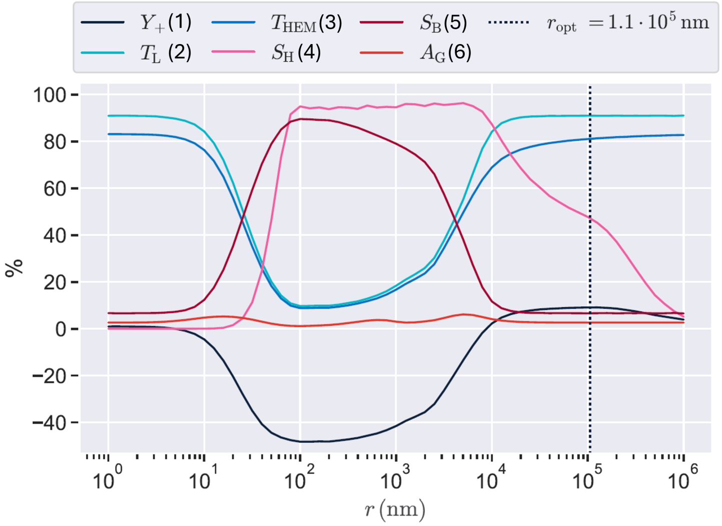

Figure 1.5: The figure presents the dependence of various quantities of interest on particle size (r) calculated via a ray tracing monte-carlo simulation. The dark blue line represents the extra yield (Y_+, 1), the turquoise line represents perpendicular transmittance (T_L, 2), the blue line represents hemispherical transmittance (T_{HEM}, 3), the pink line represents hortiscatter (S_H, 4), and the raspberry line represents backscatter (S_B, 5). The red line represents glass absorption (A_G, 6). This work was done by Benjamin Slotboom using LightTools, and has not been published yet.

plants, cyanobacteria, and algae. Chlorophyll is a tetrapyrrole-based organic molecule with several structural variants (chlorophyll a, b, c_1, c_2, d, and f), each differing in the composition and arrangement of side chains as shown in Fig 1.6. These structural differences influence their absorption spectra, allowing organisms to optimize light capture in different environments [26]. Among them, chlorophyll a and b are the main pigments in plants [27].

The biological process of absorbing photon energy by chlorophylls and converting it into organic molecules that store chemical energy is called photosynthesis. The general equation of photosynthesis was first proposed by Cornelis Bernardus van Niel and later became the current form of the equation shown in Eq. 1.1. Photosynthesis consists of two stages, the light-dependent reaction and the light-independent reaction. In the light-dependent reaction, chlorophyll converts photon energy into chemical energy by consuming water molecules. In this process, oxygen, reduced nicotinamide adenine dinucleotide phosphate (NADPH), and adenosine triphosphate (ATP) which store the chemical energy, are formed. NADPH and ATP produced in the light-dependent reaction serve as essential energy carriers for the light-independent reaction, where carbon dioxide is converted into carbohydrates. Together, these reactions form a series of electron transport processes as shown in Fig. 1.7 [28].

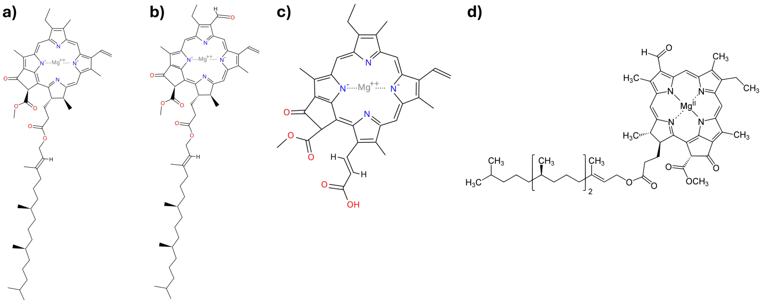

Figure 1.6: The chemical structure of a) chlorophyll a, b) chlorophyll b, c) chlorophyll c_1, d) chlorophyll d.

$$6\,CO_2 + 6\,H_2O = C_6H_{12}O_6\,(\text{glucose}) + 6\,O_2. \tag{1.1}$$

Expanding on the light-dependent reaction, there are two photosystems: photosystem I (PSI) and photosystem II (PSII). Each photosystem contains a combination of pigments, including chlorophyll a, chlorophyll b, carotenoids, and other accessory pigments. When a photon is absorbed by a pigment, an electron is excited to a higher energy level and transferred through an electron transport chain. In this chain, electrons move from PSII to PSI in a stepwise manner, driving the synthesis of ATP and NADPH as shown in 1.7. Electron transport occurs within both PSI and PSII through specialized reaction centers.

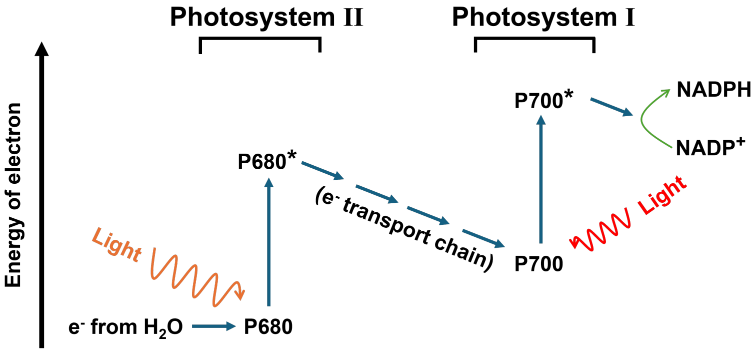

Figure 1.7: The chain reaction of photosystem I and photosystem II.

Each reaction center contains chlorophyll a and accessory pigments that help tune its absorption spectrum. In PSI, the reaction center is called P700 because it absorbs light most efficiently at 700 nm, while in PSII, the reaction center is P680, with a peak absorption at 680 nm (in the red light region). After absorbing the corresponding photon, an electron is excited and transferred through the electron transport chain, ultimately reducing $NADP^+$ to NADPH. The absorption spectral range of the chlorophyll pigments responsible for photosynthesis defines the part of the solar spectrum that is called photosynthetically active radiation (PAR). The spectrum range of PAR highly overlaps with the human visual spectrum, ranging from 400 nm to 700 nm. Photons with longer wavelengths (over 700 nm) lack sufficient energy to drive photosynthesis, although the far-red (700 - 750 nm) photons can impact plant growth and photosynthesis [29]. The shorter-wavelength photons (below 400 nm) can be harmful to plant cells due to their high energy, though most are filtered out by the atmosphere. Each photosynthetic pigment has a different absorption spectrum within the PAR range. Chlorophyll a has its strongest absorption at 440 nm, with a secondary peak at 680 nm. Chlorophyll b absorbs most efficiently at 470 nm and 650 nm, while carotenoids primarily absorb light between 400 nm and 550 nm. A chloroplast contains multiple pigments. The combined absorption spectra of all pigments within the chloroplast influence the plant's overall photosynthetic efficiency. The combined absorption spectrum of all pigments determines the plant's "action spectrum", which reflects the photosynthetic rate at different wavelengths of light. As shown in Fig. 1.8, the action spectrum exhibits peaks in both the red and blue regions, which explains why plant leaves appear green, since green wavelengths are least absorbed and mostly reflected.

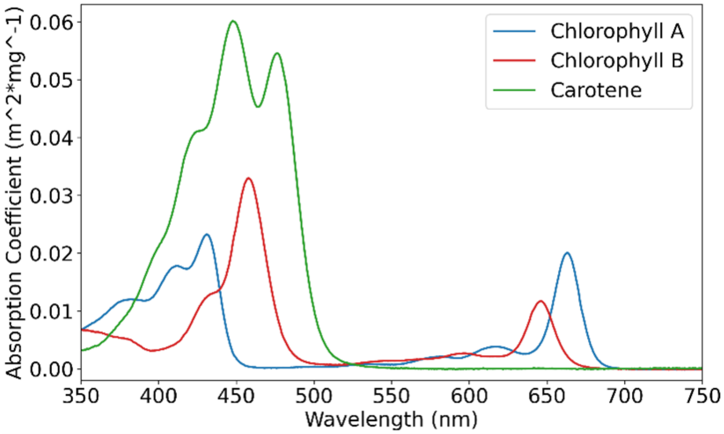

Figure 1.8: The absorption coefficient of chlorophyll a, b, and carotene. Data from Clementson et al. [30].

Generally, blue and red light play a crucial role in plant growth and development. Blue light (450-495 nm), for instance, promotes a more compact lettuce, enhances pigment concentration in lettuce [31], and supports the highest vitamin C content of Chinese cabbage [32]. Red light (620-700 nm), has been shown to increase tomato yield [33], and promote reproductive growth of Chinese cabbage [32]. It also reduces nitrate concentration in lettuce, marjoram, and green onions [34]. Additionally, red light enhances vitamin C content in green vegetables such as spinach and rocket [35]. However, this does not mean that green light is insignificant. Studies suggest that green light (495-570 nm) can support overall growth in lettuce [36]. For instance, baby leaf lettuce benefits from green light exposure, leading to increased vitamin C and tocopherol homologues [37].

1.3.2. Extension of PAR into ultraviolet and near infrared range

Since the early 2000s, some researchers have advocated for including far-red light (FR) (700-750 nm) and ultraviolet (UVA: 315-400 nm) radiation into the photosynthetically active radiation (PAR) spectrum (traditionally defined as 400-700 nm). Some key reasons for incorporating FR light include: it enhances total biomass accumulation in lettuce [38], improves the canopy gross photosynthesis rate of lettuce and tomato [39], and increases fruits production in paprika [40]. Young plants with a reduced amount of FR light lower whole-plant CO_2 assimilation rates at low light intensity through reduced leaf area [41]. Recent findings indicate that FR light can be as efficient for driving photosynthesis as light within the traditional PAR range [39]. However, FR light also has drawbacks. For example, prolonged FR exposure reduces carotenoid level in thale cress [42], and long-term FR exposure decreases tomato leaf resistance to Botrytis cinerea infections [43]. Other effects of adding FR light includes excessive stem elongation of petunia [44], increasing biomass, and lowering phytochemical concentrations of baby leaf lettuce [45].

The potential benefits of UVA light include increased fresh and dry weight of tomato under moderate UVA exposure [46] and improved biomass and bioactive compound accumulation in kale [47]. Additionally, UVA exposure stimulates the production of UV-protective pigments in Arabidopsis thaliana [48] and enhances the growth and nutritional quality of lettuce [49]. UVA has beneficial effects on the below-ground biomass production of the lavender under low water availability [50]. However, UVA radiation is not universally beneficial. Excessive UVA exposure can cause DNA damage and disrupt physiological processes [51]. For instance, UVA inhibits cucumber growth by reducing leaf and stem biomass [52]. Similarly, in wheat, UVA exposure reduces plant height, leaf area, and total biomass in wheat, cotton, sorghum, and amaranth [53].

Responses to UVA can vary significantly depending on plant species and genotype. The impact of adding UVA is different for Chandausi wheat and Purna wheat [54, 55]. Moreover, the effects of UVA exposure depend on its intensity and the background irradiance of the environment [55]. The effect of UVA and FR light vary across plant species and genotypes, and environmental conditions can further modify their influence. Due to their mixed effect, both positive and negative, the inclusion of UVA and FR in the PAR spectrum remains a topic of ongoing debate.

1.4. Luminescent materials

Luminescent materials are abundant in our daily lives, such as LED lighting, television displays, lasers, data communications, and even brighteners in detergents. The fundamental working principle of luminescent materials involves the absorption of high-energy radiation followed by the emission of low-energy light. Luminescent materials can be applied to a greenhouse as a potential booster to enhance PAR photon flux by solar spectrum conversion. Fan et al. have reported a comprehensive review of the spectral conversion type, like UV-to-green, blue-to-red, and the respective potential phosphors for each type [56]. In this section, we provide a general introduction to luminescent materials. The specific luminescence mechanism varies depending on the excitation source, leading to classifications such as photoluminescence, cathodoluminescence, and chemiluminescence. Chemiluminescence results from chemical reactions that release energy in the form of light. Cathodoluminescence, often seen in old cathode-ray tube (CRT) displays, is excited by an electron beam. Photoluminescent materials, the focus of this dissertation, is then triggered by high-energy electromagnetic (EM) waves, such as ultraviolet (UV) light [57]. Photoluminescent materials, commonly called phosphors, absorb incident photons either via host-lattice transitions or activator-ion transitions (e.g., transition metals or lanthanides), thereby promoting electrons from the ground state to higher-energy excited states. After excitation, electrons undergo a series of non-radiative relaxation processes, such as lattice vibrations (phonon interactions) and thermal dissipation, before settling into the lowest energy level of the excited state. From this state, electrons return to the ground state via either radiative relaxation (photon emission) or additional non-radiative pathways (heat). The primary objective in phosphor applications is to maximize radiative relaxation, as this directly contributes to light emission intensity. However, non-radiative relaxation is inevitable and can significantly impact luminescence efficiency [58].

The non-radiative relaxation, often referred to as quenching, happens due to two primary mechanisms: temperature quenching or concentration quenching. Temperature quenching arises when thermal energy enables electrons to escape the excited state through non-radiative crossover points in the potential energy surface of the material. This occurs when the excited and ground state potential energy curves overlap at higher vibrational levels, leading to energy loss as heat rather than photon emission. Concentration quenching occurs when excessive activator ions (e.g., Eu^{2+}, Ce^{3+}) in the host lattice promote energy migration between adjacent activator sites. This energy transfer leads to non-radiative losses before photon emission can occur. The competition between the radiative and non-radiative relaxation determines the emission performance of the phosphor and is defined as quantum efficiency (or quantum yield), which is calculated by the ratio of emitted photons to absorbed photons.

The excitation mechanisms of inorganic phosphors range from 3d→3d transition in the transition metal elements, 4f→4f transition and 4f→5d transition in the lanthanide elements, charge transfer transition, and VB→CB transition, depending on the activator ions and host materials. Two transitions particularly relevant to this dissertation, the 4f→5d activator transition and the host CB→VB transition, are briefly introduced below.

4f→5d transition

The 4f→5d transition is an allowed transition and significantly more intense than the 4f→4f transition. The 5d orbitals is not shielded by $5s^2$ and $5p^6$ orbitals, making them highly sensitive to the crystal field environment. As a result, the emission spectrum of 4f→5d transitions typically appears as a broad band, in contrast to the sharp-line emissions of 4f→4f transitions. A characteristic example of a lanthanide ion featuring 4f→5d transitions is divalent europium (Eu^{2+}) and trivalent cerium (Ce^{3+}), which is widely used in luminescent materials [59, 60]. The properties and applications of Eu^{2+}-doped phosphors will be further discussed in this dissertation.

CB→VB transition

CB→VB transition involves electronic transitions between the valence band (VB) and the conduction band (CB) of the host material, rather than localized transitions within activator ions, such as 4f→4f or 4f→5d transitions in the lanthanide elements. Similar to insulators and semiconductors, electrons in the host material are confined to the valence band and require sufficient energy to be excited to the conduction band. The minimum excitation energy for host absorption is therefore determined by the bandgap energy of the material. Typical host absorption phosphors include ZnS:Ag and ZnO:Zn [61]. Upon excitation, electrons are generated in the conduction band and holes in the valence band. These mobile carriers are then sequentially trapped by defect sites, whose charge transition levels (CTLs) lie within the bandgap. Taking ZnS:Ag phosphor as an example, a free hole from the valence band is captured by the Ag dopant, which acts as an acceptor. The recombination of the electron from the conduction band with the hole trapped at the acceptor CTL releases energy as a photon. This process, known as donor-acceptor pair recombination, precisely corresponds to the 451 nm emission of ZnS:Ag phosphor.

Because of the spectral-conversion capability, luminescent materials can be applied as sprayable coatings on greenhouse glazing to modify the light spectrum entering the greenhouse. A key advantage of sprayable coatings is that they can be applied or removed on existing greenhouse glazing as needed, depending on the grower's requirements.

1.5. Research objective and dissertation outline

This dissertation investigates the use of photoluminescent materials as luminescent additives for greenhouse coating applications and addresses three main challenges. Firstly, although photoluminescent materials are well-studied and widely applied in lighting technology, their use in greenhouses to convert incoming UV into photosynthetically active radiation (PAR) remains largely unexplored, with limited practical demonstrations of phosphor-based coatings for this purpose. Secondly, there is no clear and standardized measurable quantities for quantifying how effectively these coatings perform spectral conversion. Thirdly, the current characterization method for hemispherical light transmittance requires a sample area of at least 200 cm^2, posing a significant obstacle for research groups working with functionalized roof samples and thereby hindering the development of advanced greenhouse roofing technologies.

A successful greenhouse luminescent coating should be cheap and scalable; therefore, in **Chapter Two**, an inexpensive, mass-producible silicate phosphor co-doped with Eu^{2+} and Al^{3+} is investigated. Its key photoluminescent properties, including emission, excitation, and decay spectra are characterized. A new metric, termed PAR enhancement, is introduced to quantify the ability of luminescent coatings to convert UV light to PAR. In this chapter, the first greenhouse-oriented luminescent coating based on this phosphor is fabricated, and its UV-to-PAR performance is assessed, tackling the first and second challenges.

To assess luminescent coating samples developed for greenhouse applications, a tabletop system is constructed to characterize the hemispherical light transmittance of laboratory sized samples in **Chapter Three**. The instrument is created by scaling down the reference system at Wageningen University & Research, and a systematic study of design parameters, including edge thickness, port diameter, and beam size, identifies optimal configurations for researchers who wish to evaluate small, functionalized roofing samples.

A further demonstration of the feasibility of phosphors for greenhouse applications is presented in Chapter Four and Five. In **Chapter Four**, luminescent coatings formulated with two commercial phosphors are examined: an activator-absorption phosphor ($BaMgAl_{10}O_{17}$:Eu^{2+}) and a host-absorption phosphor (ZnS:Ag). Their optical properties, including hemispherical light transmittance, absorption strength, PAR enhancement, and diffuse reflectance, are reported. The effects of coating thickness, particle mass loading, and phosphor refractive index are analyzed, and the differences between activator-absorption and host-absorption phosphors are discussed.

In **Chapter Five**, an activator-absorption phosphor, $Sr_2Si_5N_8$:Eu^{2+}, which absorbs not only UV radiation but also the blue band within the PAR spectrum, is applied in the luminescent coating. This work qualitatively studies the influence of using a phosphor that absorbs part of the PAR spectrum, focusing on total transmitted PAR and the spectral quality achieved by applying such a phosphor as a luminescent coating.

References

[1] Food Security Information Network, FSIN and Global Network Against Food Crises, Tech. rep. (2024).

[2] U. Carthy, I. Uysal, R. Badia-Melis, S. Mercier, C. O'Donnell, A. Ktenioudaki, Corrigendum to 'Global food security – Issues, challenges and technological solutions', Trends in Food Science and Technology 123 (2022) 404.

[3] E. Berenguer, D. Armenteras, A.C. Lees, et al., Drivers and ecological impacts of deforestation and forest degradation in the Amazon, Acta Amazonica 54 (2024).

[4] M. Muluneh, Impact of climate change on biodiversity and food security: a global perspective — a review article, Agriculture and Food Security 10 (2021) 1–25.

[5] H. El Bilali, I. Bassole, L. Dambo, S. Berjan, Climate change and food security, Agriculture and Forestry 66 (2020) 197–210.

[6] J. Maggio, T. Criekinge, Global Food Security 2030: assessing trends with a view to guiding future EU policies., Tech. rep. (2015).

[7] A. Nyong, T. Ngankam, T. Felicite, Enhancement of resilience to climate variability and change through agroforestry practices in smallholder farming systems in Cameroon, Agroforestry Systems 94 (2020) 687–705.

[8] A. Zsogon, L. Peres, Y. Xiao, J. Yan, A. Fernie, Enhancing crop diversity for food security in the face of climate uncertainty, Plant Journal 109 (2022) 402–414.

[9] U. de Corato, Towards new soil management strategies for improving soil quality and ecosystem services in sustainable agriculture: Editorial overview, Sustainability 12 (2020) 1–5.

[10] N. Khan, R. Ray, G. Sargani, M. Ihtisham, M. Khayyam, S. Ismail, Current progress and future prospects of agriculture technology: Gateway to sustainable agriculture, Sustainability 13 (2021) 1–31.

[11] E. Bakzelj, T. Quested, The role of reducing food waste for resilient food systems, Ecosystem Services 45 (2020) 101–140.

[12] J. Osumba, J. Recha, G. Oroma, Transforming agricultural extension service delivery through innovative bottom-up climate-resilient agribusiness farmer field schools, Sustainability 13 (2021).

[13] A. Toromade, D. Soyombo, E. Kupa, T. Ijomah, Reviewing the impact of climate change on global food security: Challenges and solutions, International Journal of Applied Research in Social Sciences 6 (2024) 1403–1416.

[14] X. Blasco, M. Martınez, J. M. Herrero, C. Ramos, J. Sanchis, Model-based predictive control of greenhouse climate for reducing energy and water consumption, Computers and Electronics in Agriculture 55 (2007) 49–70.

[15] C. Maraveas, D. Piromalis, K. G. Arvanitis, T. Bartzanas, D. Loukatos, Applications of IoT for optimized greenhouse environment and resources management, Computers and Electronics in Agriculture 198 (2022).

[16] C. Gueymard, D. Myers, K. Emery, Proposed reference irradiance spectra for solar energy systems testing, Solar Energy 73 (2002) 443–467.

[17] G. Swinkels, F. Kempkes, S. Hemming, Using a ray-tracing model to design a greenhouse with maximized transmission during winter, International Symposium on Applications of Modelling as an Innovative Technology in the Horticultural Supply Chain-Model-IT 1154 (2015) 179–184.

[18] Nederlands Normalisatie-instituut, NEN 2675+C1 Greenhouse glass - Determination of optical properties of greenhouse covering materials and screens, Tech. rep. (2018).

[19] G. Swinkels, Transvision: A light transmission measurement system for greenhouse covering materials, Acta Horticulturae 956 (2012) 563–568.

[20] S. Hemming, G. L. Swinkels, A. J. Van Breugel, V. Mohammadkhani, Evaluation of diffusing properties of greenhouse covering materials, Acta Horticulturae 1134 (2016) 309–316.

[21] L. Marcelis, A. Broekhuijsen, E. Meinen, E. Nijs, M. Raaphorst, Quantification of the growth response to light quantity of greenhouse grown crops, Acta Horticulturae 711 (2006) 97–103.

[22] T. Li, E. Heuvelink, T. A. Dueck, J. Janse, G. Gort, L. F. Marcelis, Enhancement of crop photosynthesis by diffuse light: Quantifying the contributing factors, Annals of Botany 114 (2014) 145–156.

[23] T. Li, Q. Yang, Advantages of diffuse light for horticultural production and perspectives for further research, Frontiers in Plant Science 6 (2015) 1–5.

[24] N. Victoria, E. Romero, B. van Breugel, C. Stanghellini, S. Hemming, Can extreme light diffusion still increase crop growth in greenhouses?, Acta Horticulturae 1423 (2025) 79–86.

[25] G. van Steekelenburg, S. Hemming, E. Kaiser, E. Heuvelink, Quantifying the effects of hortiscatter in greenhouse cover materials on crop yield, Acta Horticulturae 1423 (2025) 87–94.

[26] G. Vernon, The chlorophylls, Academic Press New York and London, 2014.

[27] J. Palta, Leaf chlorophyll content, Remote Sensing Reviews 5 (1990) 207–213.

[28] R. Clayton, Photosynthesis: Physical Mechanisms and Chemical Patterns, Cambridge University Press, 1980.

[29] S. Zhen, M. van Iersel, B. Bugbee, Photosynthesis in sun and shade: the surprising importance of far-red photons, New Phytologist 236 (2022): 538-546.

[30] L. Clementson, B. Wojtasiewicz, Dataset on the absorption characteristics of extracted phytoplankton pigments, Data in Brief 24 (2019).

[31] D. Sergejeva, I. Alsina, M. Duma, L. Dubova, I. Augspole, I. Erdberga, K. Berzina, Evaluation of different lighting sources on the growth and chemical composition of lettuce, Agronomy Research 16 (2018) 892.

[32] H. Li, C. Tang, Z. Xu, X. Liu, X. Han, Effects of different light sources on the growth of non-heading Chinese cabbage (Brassica campestris L.), Journal of Agricultural Science 4 (2012).

[33] N. Lu, T. Maruo, M. Johkan, M. Hohjo. S. Tsukagoshi, Y. Ito, T. Ichimura, Y. Shinohar, Effects of supplemental lighting with light-emitting diodes (LEDs) on tomato yield and quality of single-truss tomato plants grown at high planting density, Environment Control in Biology 50 (2012).

[34] G. Samuoliene, A. Urbonaviciute, P. Duchovskis, Z. Bliznikas, P. Vitta, A. Zukauskas, Decrease in nitrate concentration in leafy vegetables under a solid-state illuminator, HortScience 44 (2009) 1857–1860.

[35] Z. Bliznikas, A. Zukauskas, Effect of supplementary pre-harvest LED lighting on the antioxidant and nutritional properties of green vegetables, Acta Horticulturae 939 (2012).

[36] M. Johkan, K. Shoji, F. Goto, S. Hahida, T. Yoshihara, Effect of green light wavelength and intensity on photomorphogenesis and photosynthesis in Lactuca sativa, Environmental and Experimental Botany 75 (2012) 128–133.

[37] G. Samuoliene, R. Sirtautas, A. Brazaityte, P. Duchovskis, LED lighting and seasonality effects antioxidant properties of baby leaf lettuce, Food Chemistry 134 (2012) 1494–1499.

[38] M. Lee, K. Son, M. Oh, Increase in biomass and bioactive compounds in lettuce under various ratios of red to far-red LED light supplemented with blue LED light, Horticulture Environment and Biotechnology 57 (2016) 139–147.

[39] S. Zhen, B. Bugbee, Far-red photons have equivalent efficiency to traditional photosynthetic photons: Implications for redefining photosynthetically active radiation, Plant, Cell & Environment 43 (2020) 1259–1272.

[40] K. Park, D. Kwon, J. Lee, J. Son, Comparing photosynthesis, growth, and yield of paprika (Capsicum annuum L. 'Cupra') under supplemental sulfur plasma and high-pressure sodium lamps in growth chambers and greenhouses, Protected Horticulture and Plant Factory 27 (2018) 332–340.

[41] M. Lazzarin, K. Dupont, W. van Ieperen, L. Marcelis, S. Driever, Far-red light effects on plant photosynthesis: from short-term enhancements to long-term effects of artificial solar light, Annals of Botany 135 (2025) 589–602.

[42] J. Bou-Torrent, G. Toledo-Ortiz, M. Ortiz-Alcaide, N. Cifuentes-Esquivel, K. Halliday, J. Martinez-Garcıa, M. Rodriguez-Concepcion, Regulation of carotenoid biosynthesis by shade relies on specific subsets of antagonistic transcription factors and cofactors, Plant Physiology 169 (2015) 1584–1594.

[43] Y. Ji, T. Ouzounis, S. Courbier, E. Kaiser, P. Nguyen, H. Schouten, R. Visser, R. Pierik, L. Marcelis, E. Heuvelink, Far-red radiation increases dry mass partitioning to fruits but reduces Botrytis cinerea resistance in tomato, Environmental and Experimental Botany 168 (2019) 103889.

[44] T. Shibuya, M. Izumi, R. Endo, Effects of end-of-day far-red light and relative humidity on flowering and stem elongation of petunia (Petunia × hybrida) seedlings, Scientia Horticulturae 324 (2024) 112600.

[45] Q. Li, C. Kubota, Effects of supplemental light quality on growth and phytochemicals of baby leaf lettuce, Environmental and Experimental Botany 67 (2009) 59–64.

[46] T. Tezuka, T. Hotta, I. Watanabe, Growth promotion of tomato and radish plants by solar UV radiation reaching the Earth's surface, Journal of Photochemistry and Photobiology B: Biology 19 (1993) 61–66.

[47] J. Lee, M. Oh, K. Son, Short-Term Ultraviolet (UV)-A light-emitting diode (LED) radiation improves biomass and bioactive compounds of kale, Frontiers in Plant Science 10 (2019) 464319.

[48] D. Biswas, M. Jansen, Natural variation in UV-B protection amongst Arabidopsis thaliana accessions, Emir. J. Food Agric. 2012 24 (2012) 621–631.

[49] T. Hooks, J. Masabni, L. Sun, G. Niu, Effect of pre-harvest supplemental uv-a/blue and red/blue led lighting on lettuce growth and nutritional quality, Horticulturae 7 (2021) 80.

[50] M. Bernal, L. Llorens, J. Badosa, D. Verdaguer, Interactive effects of UV radiation and water availability on seedlings of six woody Mediterranean species, Physiologia Plantarum 147 (2013) 234–247.

[51] A. Stapleton, Ultraviolet Radiation and Plants: Burning Questions, The Plant Cell 4 (1992) 1353–1358.

[52] D. Krizek, R. Mirecki, S. Britz, Inhibitory effects of ambient levels of solar UV-A and UV-B radiation on growth of cucumber, Physiologia Plantarum 100 (1997) 886–893.

[53] S. Kataria, K. N. Guruprasad, S. Ahuja, B. Singh, Enhancement of growth, photosynthetic performance and yield by exclusion of ambient UV components in C3 and C4 plants, Journal of Photochemistry and Photobiology B: Biology 127 (2013) 140–152.

[54] S. Kataria, K. N. Guruprasad, Solar UV-B and UV-A/B exclusion effects on intraspecific variations in crop growth and yield of wheat varieties, Field Crops Research 125 (2012) 8–13.

[55] X. Sun, E. Kaiser, P. J. Aphalo, L. F. Marcelis, T. Li, Plant responses to UV-A1 radiation are genotype and background irradiance dependent, Environmental and Experimental Botany 219 (2024) 105621.

[56] Y. Fan, Y. Zhou, Z. Qiu, S. Lian, Photoluminescent materials for solar spectral conversion greenhouse films, Journal of Materials Chemistry C (2025) 5462–5482.

[57] K. Shinde, S. Dhoble, H. Swart, K. Park, Classification of Luminescence, 2008.

[58] G. Blasse, B. Grabmaier, Luminescent Materials, Springer Berlin, Heidelberg, 1994.

[59] Y. Kishimoto, X. Zhang, T. Hayakawa, M. Nogami, Blue light emission from Eu^{2+} ions in sol-gel derived Al_2O_3-SiO_2 glasses, Journal of Luminescence 129 (2009) 1055–1059.

[60] J. Van Krevel, H. Hintzen, R. Metselaar, A. Meijerink, Long wavelength Ce^{3+} emission in Y-Si-O-N materials, Journal of Alloys and Compounds 268 (1998) 272–277.

[61] L. Ozawa, M. Itoh, Cathode Ray Tube Phosphors, Chemical Reviews 103 (2003) 3835–3855.

2

The potential of SiO_2:Al^{3+},Eu^{2+} blue phosphor coatings in greenhouse application

Solar spectral conversion by a low-cost luminescent coating for greenhouse applications increases crop yield and can contribute to addressing the food crisis. A luminescent coating based on cheap SiO_2 particles doped with Eu^{2+} and Al^{3+} demonstrated extra photosynthetically active radiation (PAR) in this work. To optimize the efficiency of this phosphor for greenhouse applications, three phosphor series with varying Al/Eu content in SiO_2 were synthesized via a sol-gel approach and characterized by luminescence decay time, absorption, luminescent excitation, emission, and quantum yield measurements. With increasing the Eu%, at a fixed Al%, the decay time and quantum yield decreased while the emission shifted to the red. The effect can be explained by a more and more efficient resonance energy transfer to lower energy Eu^{2+} ions and quenching sites. While increasing the Al% at a fixed Eu%, the decay time and quantum yield increased, and the red-shift was reduced. Both effects can be explained by an enhanced Eu^{2+} solubility (reduced Eu clustering) through the Al^{3+} co-doping, causing the average Eu^{2+}-Eu^{2+} distance to be higher and the onset of concentration quenching to shift to a higher Eu%. Specifically, we found that for 1 mol% Eu^{2+}, a minimum of 4 mol% Al^{3+} was required to avoid concentration quenching. Two indicators were developed to quantify the UV-to-PAR conversion efficiency and to quantify the PAR transmission enhancement. Both indicators were determined in a real coating sample based on the optimized phosphor. The result showed that an additional PAR was provided by our luminescent coating. A general discussion about all factors that can bring the conversion efficiency of a phosphor coating closer to the theoretical maximum will be presented.

The content of this chapter is based on the following publication:
Chun-Ting Cho, Giacomo Bosco, Erik van der Kolk, Opt. Mater. 157 (2024) 116047.

2.1. Introduction

According to the 2023 report from the Global Network Against Food Crises, food insecurity is threatening more than 238 million people all over the world [1]. This crisis will become severe due to climate change causing extreme weather and, in the longer run, rising sea levels [2]. How to produce more food in less area is turning into a global economic issue. Greenhouses can provide a solution as they have a much higher production yield per surface area compared to open land growth, and provide independence from weather conditions.

The amount of light (flux) projected on plants has a large impact on the yield. The concept of "1% extra light leads to 1% extra crop yield" is widely accepted in the dutch horticulture field [3]. Greenhouse owners, therefore, often utilize artificial lighting, such as high-pressure sodium lamps and LEDs, not only to increase photon flux but also to adjust the light spectrum for specific growing stages [4–8]. As these techniques consume energy, it is worthwhile to consider a photoluminescent material that converts ultraviolet (UV) solar radiation to photosynthetically active radiation (PAR) as an alternative solution for spectral conversion or extra light since UV is unused in photosynthesis [9–11].

An economically viable spectral conversion coating must be based on a cheap phosphor. Silicon dioxide (SiO_2) is a popular host matrix in the industry due to its excellent chemical stability and low production cost. Doping with Eu^{2+} turns SiO_2 into a blue emitting phosphor that absorbs UV light but no PAR, seemingly ideal for UV to PAR conversion and a subsequent enhanced PAR transmission [12–14]. Unfortunately, a significant limitation observed in this material is that Eu^{2+} is limited to low doping concentration when incorporated into the SiO_2 host because lanthanide ions can only create their own crystallographic interstitial sites due to the size and charge mismatch. The resulting low solubility limit leads to a lower luminescent intensity due to concentration quenching, even more so due to clustering of lanthanide (Ln) ions [15–17]. For example, research from Lochhead et al. has shown that clustering of Eu^{3+} in SiO_2 already happens at 0.3 mol% [18]. Co-doping SiO_2 with ions like Al, P, Ba, or Mg has successfully been used to increase the solubility of Ln ions [19–22]. Co-doping with Al has appeared especially beneficial for increasing Eu^{2+} luminescent intensity [23–25].

The mechanism of how co-doping with Al^{3+} helps increase the solubility limit of trivalent lanthanides in the SiO_2 host was described by Lægsgaard using density function theory (DFT) to predict the local structure around Er^{3+} ions in silica-alumina oxide [26]. On the other hand, Funabiki et al. explained the co-doping theory from a thermodynamic point of view by the formation of a solvation shell [27]. The formation of the Al-Ln complex increases system entropy and suppresses Ln clustering. Nogami et al. proved that co-doping Al^{3+} in SiO_2 enhances the luminescent intensity of Eu^{2+} by 250 fold [24]. Kishimoto et al. studied the Eu^{2+} quantum efficiency while tuning the Al and Eu content between 0-10% and 0-5%, respectively. They concluded that 1 wt% Eu_2O_3 in $1Al_2O_3$-$99SiO_2$ glass gave the highest quantum efficiency of 48% [25].

Because a greenhouse coating requires the highest possible UV absorption in a coating of limited practical thickness, we report in this work a synthesis that increases absorption by raising Eu^{2+} doping content without lowering the quantum efficiency and subsequently applying the best phosphor particles in a real greenhouse coating. To achieve this, three sample series with a varying Eu%, a varying Al%, and a fixed Al/Eu ratio were synthesized via a base-catalyzed sol-gel method [28, 29]. Due to the lack of published work quantifying the efficiency of a greenhouse coating, two efficiency indicators are presented [30, 31]. The first is to quantify the UV to PAR conversion efficiency, and the second is the PAR transmission enhancement. The results allowed us to discuss relevant processes that determine the success of a spectral-converting greenhouse coating.

2.2. Material and method

2.2.1. Phosphor preparation

All samples were synthesized via the sonochemical sol-gel method. A stoichiometric amount of aluminum isopropoxide $Al(O\text{-}i\text{-}Pr)_3$ (Sigma-aldrich, ≥ 98%) was added into pure ethanol, and europium nitrate $Eu(NO_3)_3$ (ABCR, 99.9%) was added into deionized (DI) water respectively, according to the molar ratio of the sample composition. After the precursors were completely dissolved, the two solutions were added into tetraethyl orthosilicate TEOS (ABCR, 99%) solution, the source of Si, with pure ethanol. The resultant mixture was then immersed in an iced sonication bath with the addition of ammonia hydroxide NH_4OH (Sigma-aldrich, 28%) as a reaction catalyst to control particle shape and accelerate the reaction. The phosphor particles were washed with ethanol and DI water three times to remove non-reacted residuals and then dried in a 60 °C oven overnight to remove DI water and ethanol. The dried sample was then heated at 500 °C in the air for six hours to remove the volatile and organic residues, and under 1100 °C for three hours with 7% H_2-N_2 gas to reduce the trivalent Eu to the divalent state.

2.2.2. Sample series

The elemental composition of all samples synthesized in this study was characterized by energy-dispersive X-ray spectroscopy incorporated in an SEM (JSM-IT100, JEOL). They are presented in the form of $SiO_2{:}Al_xEu_y$, where x and y represent the molar percentage (mol%) of Al^{3+} and Eu^{2+}, respectively, to all cations (Si + Al + Eu). For instance, sample $SiO_2{:}Al_{0.04}Eu_{0.01}$ consists of 4 mol% Al^{3+}, 1 mol% Eu^{2+}, and 95 mol% Si. The synthesized samples are categorized into 3 groups: I) fixed 4 mol% Al^{3+} concentration (Eu = 0.5, 1, 2, 3 mol%), II) fixed 1 mol% Eu^{2+} concentration (Al = 1, 2, 3, 4, 10 mol%), and III) fixed Al/Eu content ratio of 4 (Eu = 1, 3, 5 mol%).

2.2.3. Luminescent coating production

The coating consists of a dispersing agent, defoamer, acrylic resin, thickeners, and our optimized phosphor. The loading of phosphors was 8 mass% with a wet thickness of 100 µm and applied on a 1 mm sapphire substrate by a bar-coater (TQC film applicator, Industrial Physics). A no-phosphor coating was produced following the same recipe but without the phosphor.

2.2.4. Characterization methods

The crystal structure of the samples was checked with x-ray powder diffraction (X'Pert Pro, PANalytical) by using Cu K $\alpha 1$ radiation. The particle morphology was characterized by a transmission electron microscope (JEM1400, JEOL) and a scanning electron microscope (JSM-IT100, JEOL). The photoluminescence excitation and emission spectra were recorded by a photomultiplier tube (R7600U-20, Hamamatsu) connected to a monochromator (SP2300, Princeton Instruments). A xenon lamp connected to a monochromator (Gemini 180, HORIBA) was used as an excitation light source. All the tested samples were under excitation of 275 nm UV for the measurement of the photoluminescence spectrum (PL), while the photoluminescence excitation spectrum (PLE) was recorded by monitoring emission at 475 nm. The decay spectra were obtained under 275 nm excitation and recorded by a digitizer (DT5730, CAEN) with a pulsed laser (NT230, EKSPLA) as the excitation light source.

The photoluminescence quantum yield (PLQY) of phosphor samples η (%) was determined by integrating over the sample and LED emission wavelength range in an integrating sphere (Labsphere) using a 340 nm LED (M340L4, Thorlabs) excitation light source and a spectrometer (QE65Pro, Ocean Insight) according to the formula:

$$\eta = \frac{\int E_s(\lambda)d\lambda}{\int [R_r(\lambda) - R_s(\lambda)]d\lambda} \tag{2.1}$$

$R_r(\lambda)$ and $R_s(\lambda)$ are the calibrated reflection spectra of the non-absorbing reference reflector (PTFE, MicroFlon S-203, Shamrock) and the Eu-doped sample under 340 nm excitation, while $E_s(\lambda)$ is the calibrated emission spectrum of the Eu-doped sample. A commercial phosphor $BaMgAl_{10}O_{17}:Eu^{2+}$ (BAM:Eu, Phosphor Technology) with a reported 90% PLQY was measured in this set-up, and the PLQY of 86.9% was obtained.

2.2.5. UV to PAR performance indicators

The absorption spectrum $A_s(\lambda)$ (%) and internal UV-to-PAR conversion efficiency η_{coating} (%) of the luminescent coating were characterized by projecting a deuterium light source (AvaLight-DH-S, Avantes) perpendicularly onto the sample. An integrating sphere (Labsphere) was placed behind the sample substrate to collect the transmitted light, as shown in Fig. 2.1. The absorption spectrum $A_s(\lambda)$ and UV-to-PAR conversion efficiency η_{coating} can both be approximated by the formulas:

$$A_s(\lambda) = 1 - \frac{I_{\text{coating}}(\lambda)}{C_{\text{Ref}} * I_{\text{substrate}}(\lambda)} \tag{2.2}$$

$$\eta_{\text{coating}} = \frac{\int_{400}^{700} [I_{\text{coating}}(\lambda) - C_{\text{Ref}} * I_{\text{substrate}}(\lambda)]d\lambda}{\int_{250}^{400} [C_{\text{Ref}} * I_{\text{substrate}}(\lambda) - I_{\text{coating}}(\lambda)]d\lambda} \tag{2.3}$$

$I_{\text{substrate}}(\lambda)$ and $I_{\text{coating}}(\lambda)$ are the calibrated intensity spectra of the sapphire substrate and the luminescent coating sample on the sapphire substrate collected by the spectrometer connected to the integrating sphere, respectively.

C_{Ref} is a constant that corrects for the difference in reflection with and without coating (caused by surface reflection and diffuse reflection by the particles). The value can be calculated from the transmittance of the coating sample relative to the non-coated sapphire substrate at a wavelength where there is no emission and absorption. A high C_{Ref}

value means a small reflection from the coating surface. We make an approximation that C_{Ref} is constant from 250 nm to 800 nm.

In our measurement configuration, the following equation holds: 1=A+T+R+W, in which W equals the wave-guided fraction escaping through the sample edges. Although we measured the backward reflection R (through diffuse reflectance measurement) and transmission T, we cannot reliably measure W. Therefore, we have introduced a more practical and reliable metric C_{Ref} that takes into account the influence of both the backward scattering and waveguiding effects on the loss of incident PAR photon flux. C_{Ref} was determined within a near-infrared (NIR) spectral range, 700-750 nm, unaffected by both emission and absorption. By applying C_{Ref}, the influence of backward scattering and waveguiding effects (R+W) can be removed from the calculations of $A_{coating}(\lambda)$ and $\eta_{coating}$. The value can be calculated from the transmittance of the coating sample relative to the non-coated sapphire substrate at a wavelength where there is no emission and absorption. A high C_{Ref} value means a small scattering effect from the coating surface. An assumption of constant backward scattering and waveguiding effects between 250 to 900 nm was made.

To quantify the contribution to extra PAR from the coating sample, we defined the concept of PAR enhancement (%) according to the formula:

$$\text{PAR enhancement} = \frac{\eta_{\text{coating}} * \int_{250}^{400} [A_s(\lambda) * I_{\text{solar}}(\lambda)] d\lambda}{\int_{400}^{700} I_{\text{solar}}(\lambda) d\lambda} \tag{2.4}$$

The values of $A_s(\lambda)$ and $\eta_{coating}$ are obtained from the equations 2 and 3. $I_{solar}(\lambda)$ is the AM1.5 solar spectrum in unit of photons derived from ASTM G173-03 Reference Spectra [32]. The calculation of PAR enhancement excludes the influence of the lamp spectrum and utilizes the AM1.5 solar spectrum as a reference, which provides a closer approximation to real-world conditions.

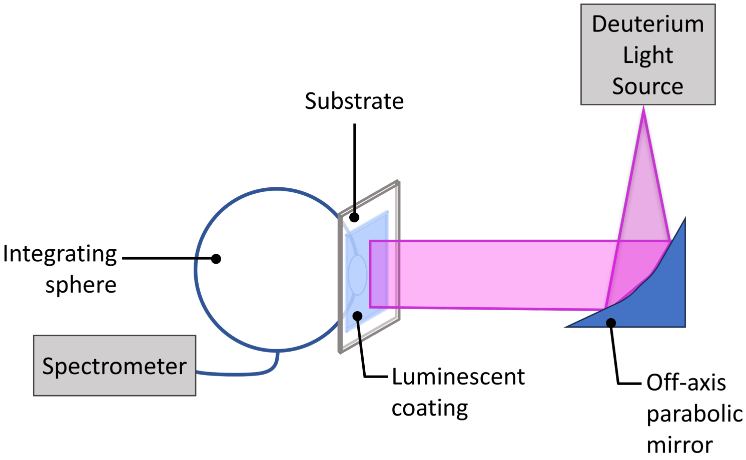

Figure 2.1: Illustration of UV to PAR indicators measurement.

2.3. Results and discussions

2.3.1. Crystal structure and morphology

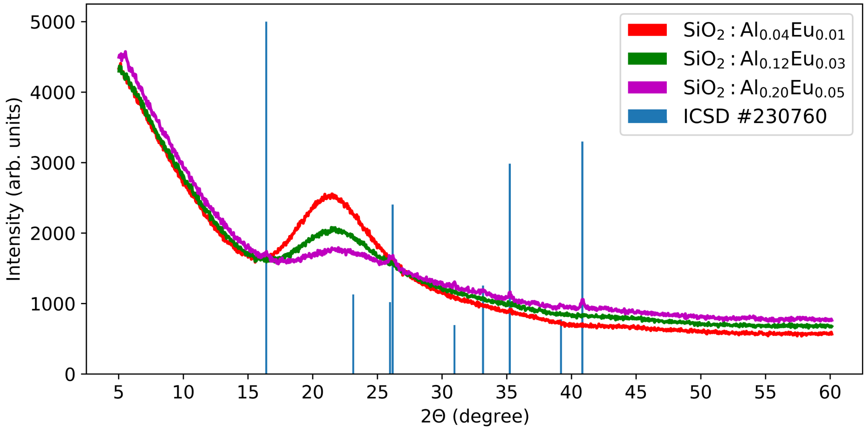

Figure 2.2: Recorded XRD pattern of sample SiO_2:$Al_{0.04}Eu_{0.01}$, SiO_2:$Al_{0.12}Eu_{0.03}$, SiO_2:$Al_{0.20}Eu_{0.05}$, and the crystalline silica-alumina oxide reference (ICSD #230760).

Fig. 2.2 contains the recorded XRD patterns of SiO_2:$Al_{0.04}Eu_{0.01}$, SiO_2:$Al_{0.12}Eu_{0.03}$, and SiO_2:$Al_{0.20}Eu_{0.05}$. Crystalline features were present only in the highest-doped sample SiO_2:$Al_{0.20}Eu_{0.05}$, matching the crystalline features of a silica-alumina oxide reference (ICSD #230760) indicated by the blue vertical lines, due to high Al^{3+} content in the sample. The rest of the synthesized samples showed only a broad peak at 23 degrees, representing the typical amorphous structure of SiO_2 [33].

The morphology of low-doped and high-doped samples recorded by SEM and TEM is shown in Fig. 2.3. The size and shape of the low-doped sample were in line with expectations of the base-catalyzed sol-gel approach and confirmed in Fig. 2.3d [29]. Such morphology disappeared and was replaced by large, sharp-edged particles when dopant/co-dopant content increased (Fig. 2.3b and c). The particle size increased from a hundred nanometers (SiO_2:$Al_{0.04}Eu_{0.01}$) to 200 μm (SiO_2:$Al_{0.20}Eu_{0.05}$). The SEM images indicate a strong particle agglomeration and irregular shape in the highest-doped sample.

2.3.2. Luminescence emission, excitation, and absorption spectra

All samples demonstrated a typical photoluminescence excitation spectrum of Eu^{2+} and a broad emission peak, which are attributed to the *4f-5d* transition of Eu^{2+} [13, 14, 24]. No characteristic *4f-4f* line emission of Eu^{3+} was found in any of the emission spectra, indicating that Eu^{3+} was not presented in our samples.

A clear red-shift of the emission peak was observed with increasing Eu^{2+} content in the group I samples (Fig. 2.4b). This phenomenon is caused by a resonance energy transfer between Eu^{2+} ions [34–36]. The SiO_2 host provides a series of possible sites instead of one specific site for Eu^{2+} due to its amorphous nature and also due to the fact that there is no ion with a similar size and charge that Eu^{2+} can replace. The energy released by a

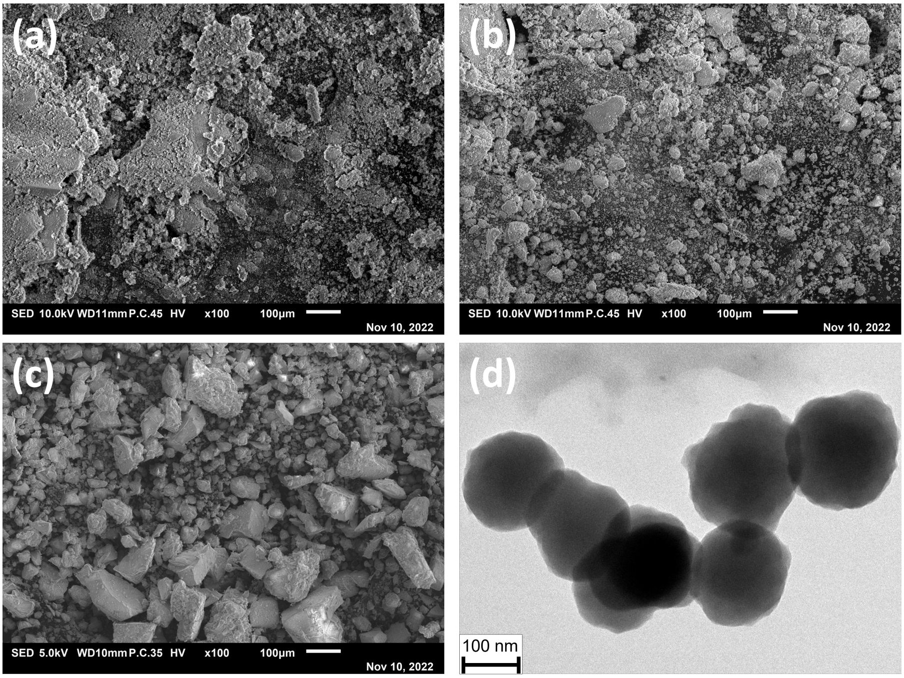

Figure 2.3: Morphology of (a) SiO_2:$Al_{0.04}Eu_{0.01}$, (b) SiO_2:$Al_{0.12}Eu_{0.03}$, (c) SiO_2:$Al_{0.20}Eu_{0.05}$. (d) TEM image of the sample SiO_2:$Al_{0.04}Eu_{0.01}$.

donor Eu^{2+} ion with higher energy 5d states, preferably transfers to an acceptor Eu^{2+} ion with lower energy 5d states because of a good spectral overlap between emission of high-energy sites and absorption of low-energy sites. In addition, the energy transfer becomes more efficient when more absorbing centers are presented [37]. As a result, the energy is transferred to Eu^{2+} ions with a lower energy 5d state after multiple transfer steps, leading to the observed red-shift of the emission spectra toward a higher Eu^{2+} content.

The same type of red-shift was observed in the emission of the fixed-Eu content group (Fig. 2.4c) following the trend of decreasing Al^{3+} content. The shift is related to the solubility of Eu^{2+} ion in the amorphous SiO_2 host [25–27]. With increasing Al^{3+} content, the distribution of Eu^{2+} ion becomes more homogeneous (clustering is reduced), leading to a longer average distance between Eu^{2+} ions and less energy transfer since the efficiency of energy transfer strongly depends on the atomic distance. Consequently, the resonance energy transfer was suppressed at high-Al content, resulting in a less pronounced red-shift.

In contrast to most of the samples with a similar PLE spectrum as SiO_2:$Al_{0.04}Eu_{0.01}$, the excitation edge of SiO_2:$Al_{0.20}Eu_{0.05}$ showed a more pronounced shift to a longer wavelength (Fig. 2.4a) due to a high Al^{3+} content and the solvation shell effect [27]. The red-shift of emission peak in the fixed Al/Eu group (Fig. 2.4d) was a collective result of mechanisms described previously.

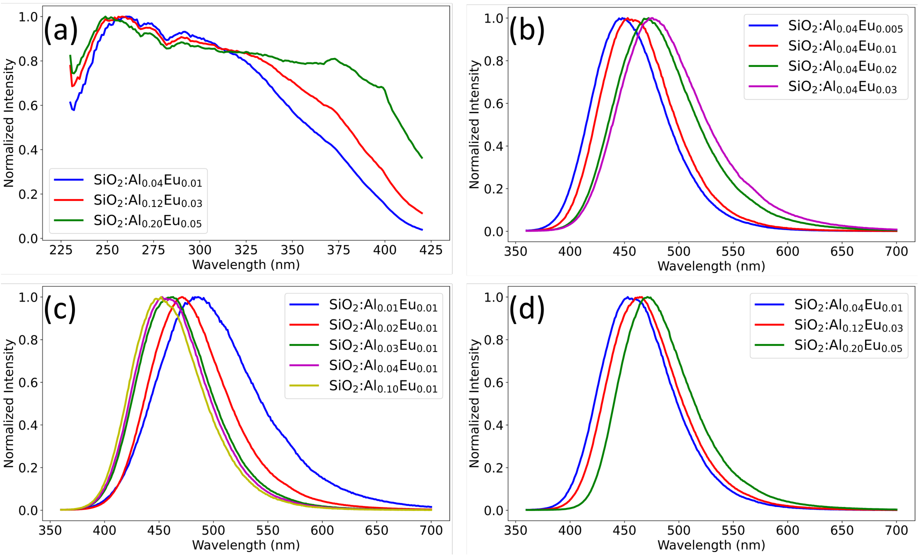

Figure 2.4: Photoluminescence excitation (PLE) and photoluminescence (PL) spectra of samples monitored at 475 nm emission and under 275 nm excitation, respectively. (a) PLE spectra of the fixed Al/Eu ratio group. (b) PL spectra of the fixed-Al group. (c) PL spectra of the fixed-Eu group. (d) PL spectra of the fixed Al/Eu ratio group.

2.3.3. Time-resolved decay characterization

In the fixed-Al group (Fig. 2.5a), the decay time decreased from 1.72 μs to 1.29 μs with increasing Eu^{2+} content due to triggering off concentration quenching effect. The decay spectra of the fixed-Eu group (Fig. 2.5b) helped find the minimum Al^{3+} content required to avoid shortening luminescent decay time and concentration quenching. Adding more Al^{3+} than 4 mol% had only a slight impact on the decay curve, indicating that the solubility of Eu^{2+} ions had been improved to a maximum. These decay curves clearly showed that 4 mol% Al^{3+} is the minimum required amount to dissolve 1 mol% of Eu^{2+} and avoid the Eu^{2+} clustering as well as the unwanted concentration quenching.

Note that when monitoring 475 nm, both the emission of the activator (low-energy Eu^{2+} sites) and the sensitizer (high-energy Eu^{2+} sites) were observed. The relative intensities changed with Eu^{2+} and Al^{3+} content. It is beyond the scope of this work to quantitatively model the complex transfer processes, especially because the nature and number of the Eu^{2+} site distribution is unknown. It is, however, instructive to investigate qualitatively the wavelength dependence of the decay and rise time because it becomes possible to more exclusively monitor the emission of the activator or the sensitizer. The results of such measurements are shown in Fig. 2.6.

We expect the high-energy Eu^{2+} ions to act as the sensitizers of the low-energy Eu^{2+} ions, which means that the decay time of the short-wavelength emission (high-energy sites) must be short, and a rise time in long-wavelength emissions should be seen. This is indeed observed in Fig. 2.6a-c. For the low-Al content samples SiO_2:$Al_{0.01}Eu_{0.01}$, the rise

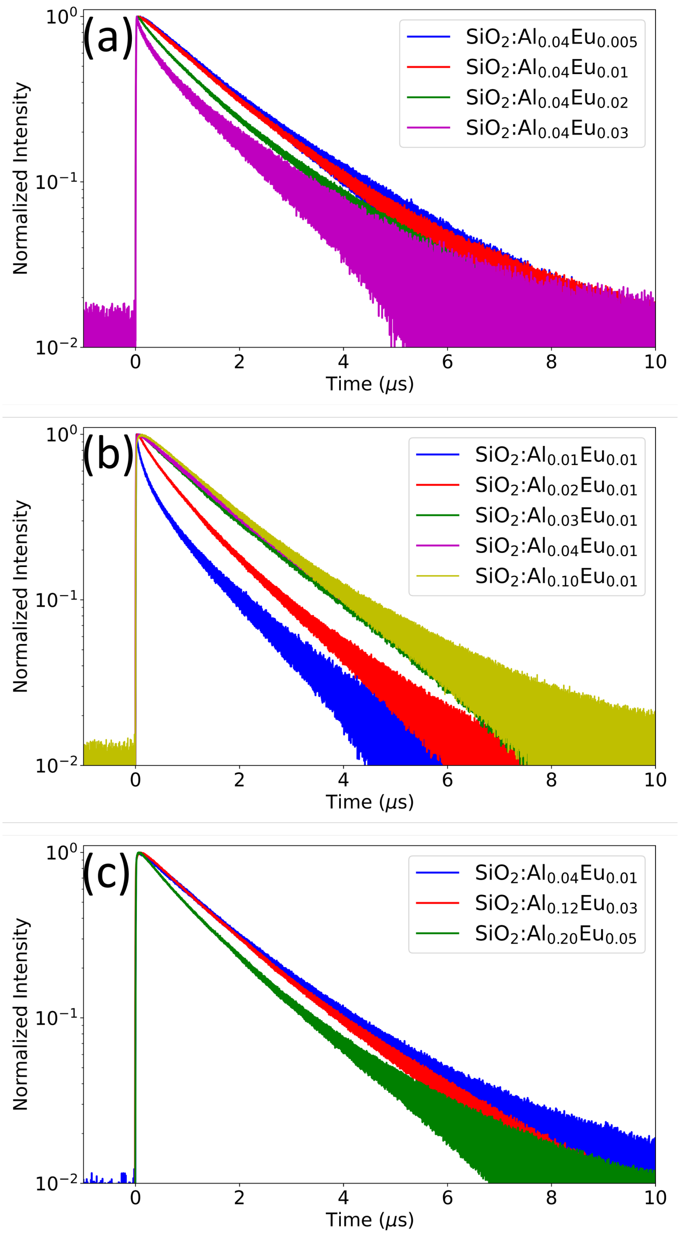

Figure 2.5: Decay signal of samples under 275 nm pulse laser excitation and monitored at 475 nm emission. (a) Group I with fixed-Al content. (b) Group II with fixed-Eu content. (c) Group III with fixed Al/Eu ratio.

time could not be seen as the decay times were short due to the earlier described efficient energy transfer and concentration quenching in the Eu^{2+} clusters. In high-Al samples, the rapid quenching of short-wavelength emissions diminished due to increased atomic distance between Eu^{2+} ions, resulting in an inefficient energy transfer from the high-energy sites to the low-energy sites and a longer decay time.

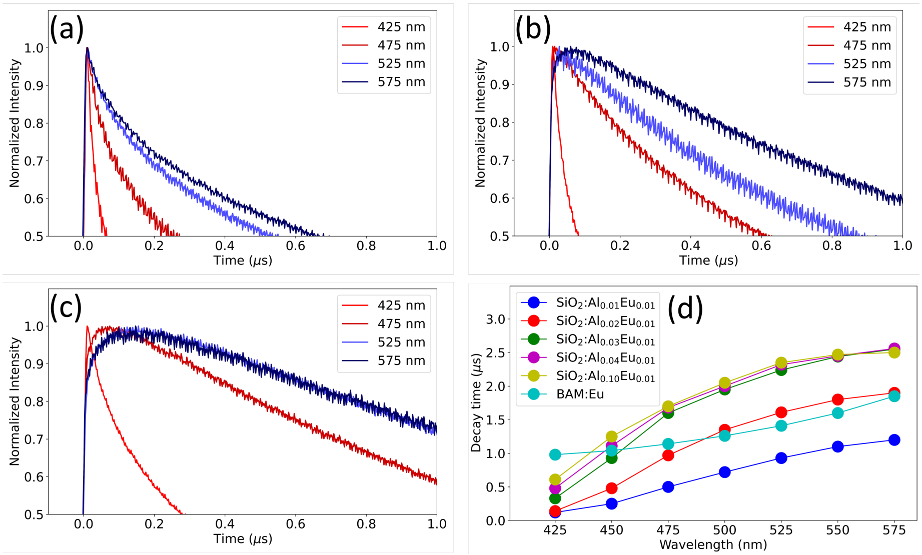

Figure 2.6: Wavelength-dependent decay signal under 275 nm pulse laser excitation of (a) SiO_2:$Al_{0.01}Eu_{0.01}$, (b) SiO_2:$Al_{0.02}Eu_{0.01}$, and (c) SiO_2:$Al_{0.04}Eu_{0.01}$. (d) The decay time of the fixed-Eu series and the reference sample BAM:Eu monitored at various emission wavelengths.

The 1/e decay time values of samples in the fixed-Eu group, monitored at wavelengths ranging from 425 nm to 575 nm are summarized in Fig. 2.6d and compared with BAM:Eu sample. The decay time generally increased with increasing monitored emission wavelength, confirming the earlier explained mechanism of energy transfer among Eu^{2+} ions. The decay time at 425 nm of low-Al samples was one-tenth of that at 575 nm, and one-fourth for the highest-Al sample. The wavelength-dependent phenomenon was also presented in BAM:Eu, but less pronounced than in our samples. The possible reason is that $BaMgAl_{10}O_{17}$ provides fewer sites to Eu^{2+} than amorphous SiO_2 [38].

2.3.4. Photoluminescent quantum yield

Fig. 2.7 displays the as-measured reflection of 340 nm LED excitation and the respective emission spectra of all samples using an integrating sphere. The absorption of excitation light correlated positively with the Eu^{2+} content in the samples, independent from the Al^{3+} content. The shift in emission peaks of each group exhibited the same pattern as Fig. 2.4. Note that Fig. 2.7 presents the as-measured spectra instead of calibrated spectra for better visualization. The PLQY calculated based on the calibrated spectra revealed the same trend as observed in the decay spectra. The PLQY value dropped toward a higher Eu^{2+} content from 69% to 21% (group I with fixed-Al content) and dropped toward a lower Al^{3+} content from 74% to 9% (group II with fixed-Eu content). The PLQY of the samples with the fixed Al/Eu ratio (group III) changed marginally from 65% to 72%.

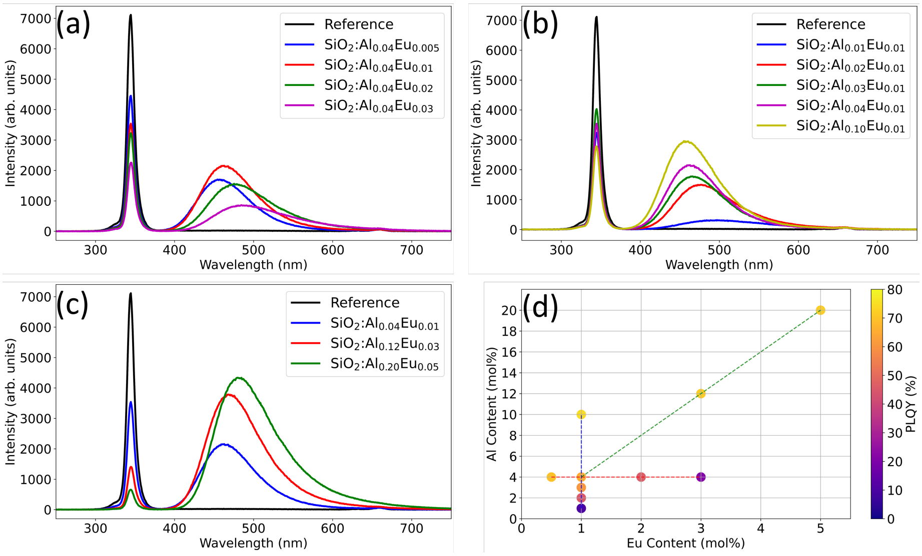

Figure 2.7: As-measured UV absorption and emission spectra and photoluminescent quantum yield. (a) Group I with fixed-Al content. (b) Group II with fixed-Eu content. (c) Group III with fixed Al/Eu ratio. (d) Photoluminescent quantum yield of samples grouped by dashed lines: red (group I), blue (group II), green (group III).

2.3.5. Luminescent coating performance

Eq. 2.2, 2.3, 2.4 were developed to quantify the UV to PAR converting efficiency and the PAR enhancement of the luminescent coating and to determine its performance for greenhouse applications. According to Eq. 2.3, the maximum of η_{coating} is 50% if the selected phosphor has 100% PLQY since only half of the emitted PAR is collected by the integrating sphere located behind the coated samples, where the greenhouse would be located. Furthermore, the maximum attainable PAR enhancement is 3.5% if all UV photons below 400 nm in the AM1.5 solar spectrum are converted into PAR and taking into account the 50% η_{coating}.

Based on the PLQY, absorption strength, and emission range, the phosphor SiO_2:$Al_{0.12}Eu_{0.03}$ was selected to produce a luminescent coating that is presented in Fig. 2.8. The absorption of UV and emission of PAR from the luminescent coating are demonstrated by the transmittance spectra shown in Fig. 2.9b, which were derived from the calibrated spectra of the sapphire substrate and the coated samples relative to the deuterium light source in Fig. 2.9a. The luminescent coating absorbed up to 420 nm, matching the excitation spectrum of the selected phosphor SiO_2:$Al_{0.12}Eu_{0.03}$ in Fig. 2.4d while

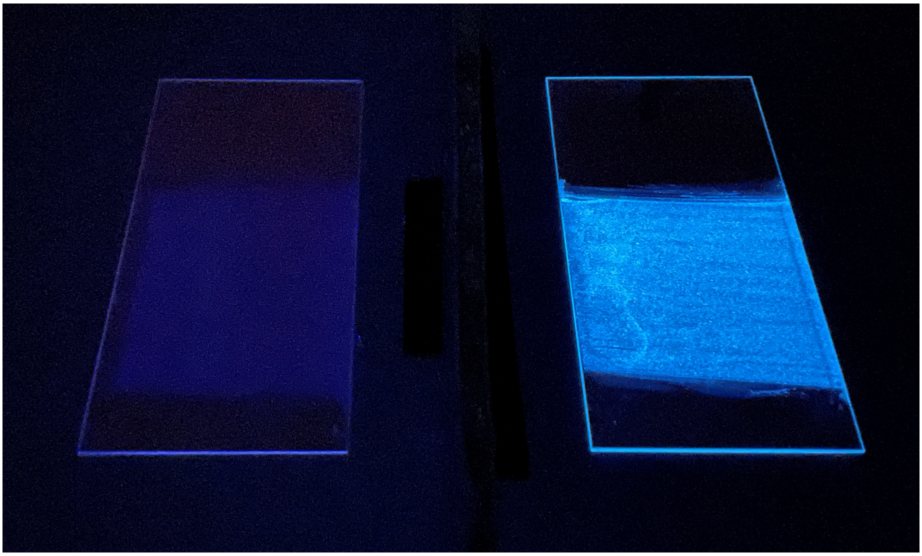

Figure 2.8: No-phosphor coating (left) and luminescent coating (right) under 340 nm LED torch.

the absorption below 250 nm was primarily attributed to the polymer matrix. The low transmittance of the luminescent coating outside the emission range (above 650 nm) resulted from the reflection at the coating surface, and hence, the C_{Ref} factor (0.96) was applied in Eq. 2.2 and 2.3. Note that the C_{Ref} is the transmittance of the luminescent coating relative to the non-coated sapphire substrate. The low refractive index of the acrylic-based matrix ($n = 1.49$) led to a higher transmittance of the no-phosphor coating than the non-coated sapphire substrate ($n = 1.76$). The dips at 480, 645, and 655 nm were due to the lamp features.

According to Eq. 2.3, we obtained a η_{coating} value of 26.2%, whereas a value of 35% was expected since the PLQY of the selected phosphor was 71.5% and only half of the emitted PAR was collected. We assumed the difference lay in the coating layer. First, the polymer matrix absorbed a minor fraction of UV, which was taken into account in the calculation. Second, part of the emitted light was guided to the edges of the coating layer and the substrate, not entering the integrating sphere. In addition, the phosphor absorbing up to 420 nm in the PAR range could also be a potential cause for the underestimated η_{coating}.

Fig. 2.9a shows a pronounced but unrealistic PAR enhancement from the luminescent coating due to the fact that the deuterium lamp contains a much higher quantity of UV radiation compared to PAR, which is not the case in the AM1.5 spectrum. Therefore, the AM1.5 spectrum was applied in the PAR enhancement calculation, which excluded the influence of the lamp spectrum. Based on Eq. 2.4, the luminescent coating achieved a 0.34% PAR enhancement, which is low compared to the theoretical maximum of 3.5%. The principal causes for the discrepancy were the less than 100% UV absorption shown in Fig. 2.9, the less than unity quantum efficiency, UV absorption by the polymer, and

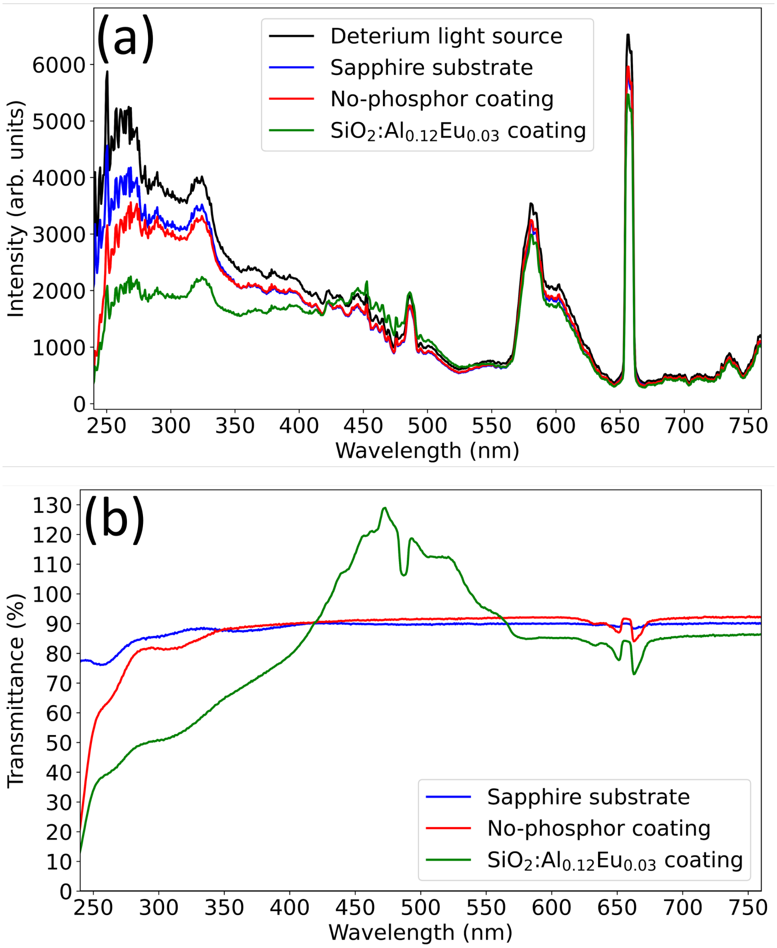

Figure 2.9: (a) The calibrated intensity spectra of deuterium light source, non-coated sapphire substrate, no-phosphor coating, and luminescent coating from a direct transmittance measurement. (b) The sample transmittance spectrum relative to the deuterium light source was derived from (a).

the previously described waveguiding effect.

This limited absorption was attributed to the content and excitation properties of Eu^{2+} in the phosphor. The absorption characteristics of the coating depend on intrinsic factors, such as the absorption mechanism of the selected phosphor, and extrinsic factors, such as particle loading and coating thickness. A band gap absorption material generally has a higher absorption strength than the allowed f-d transition, which is limited by the content of the activator. According to Lambert-Beer law, both a higher particle loading and a larger coating thickness can enhance the UV absorption of the coating

($A_s(\lambda)$) and, consequently, the PAR enhancement. However, the surface reflection will increase simultaneously, leading to an undesired low light transmittance in the greenhouse. Future research should focus on optimizing the balance between absorption, PAR emission, and surface reflection (including back-scattering) to further enhance system efficiency. Overall, our SiO_2:$Al_{0.12}Eu_{0.03}$ luminescent coating obtained one-tenth of the maximum attainable PAR enhancement.

2.4. Conclusion

SiO_2 phosphors with varying Eu^{2+}, varying Al^{3+}, and fixed Al/Eu ratio were successfully synthesized to study their potential use as a low-cost UV to PAR spectral conversion coating for greenhouses. A phosphor with a high absorption strength due to a three times higher Eu% and an almost two times higher quantum efficiency compared to the state-of-the-art was achieved by using a base-catalyzed sol-gel method.

Luminescence properties could be explained by assuming energy transfer from high-energy Eu^{2+} sites to low-energy Eu^{2+} sites in the amorphous SiO_2 lattice. For 1 mol% Eu^{2+}, a minimum of 4 mol% Al^{3+} is required to avoid Eu^{2+} clustering and minimize energy transfer that causes a red-shift and concentration quenching. The energy transfer phenomena were confirmed by a rise time in the decay curves of the low-energy Eu^{2+} emission and a short decay time of high-energy Eu^{2+} emissions.

A luminescent greenhouse coating based on the phosphor with a high absorption and quantum efficiency (SiO_2:$Al_{0.12}Eu_{0.03}$) was produced. Despite the optimized absorption and PLQY, the enhanced PAR transmission of the coating was small due to too low absorption of UV light. We conclude that more efficient spectra conversion coating should, therefore, be based on phosphors that inherently have a much stronger absorption compared to allowed f-d transitions of doping ions such as Eu^{2+}. This could be achieved by absorption in the host lattice of materials with band gaps close to 400 nm and strong emission in the PAR range.

References

[1] Food Security Information Network, FSIN and Global Network Against Food Crises. 2023 Mid-Year Update, Tech. Rep., Food Security Information Network, 2023.

[2] I. Mirón, C. Linares, J. Diaz, The influence of climate change on food production and food safety, Environmental Research 216 (2023) 1–6.

[3] L. Marcelis, A. Broekhuijsen, E. Meinen, E. Nijs, M. Raaphorst, Quantification of the growth response to light quantity of greenhouse grown crops, Acta Horticulturae 711 (2006) 97–103.

[4] M. Jones, Using light to improve commercial value, Horticulture Research 5 (2018).

[5] J. Nelson, B. Bugbee, Economic analysis of greenhouse lighting: Light emitting diodes vs. high intensity discharge fixtures, PLoS One 9 (2014).

[6] E. Kaiser, T. Ouzounis, H. Giday, R. Schipper, E. Heuvelink, L. Marcelis, Adding blue to red supplemental light increases biomass and yield of greenhouse-grown tomatoes, but only to an optimum, Frontiers in Plant Science 9 (2019) 1–11.

[7] C. Gómez, R. Morrow, C. Bourget, G. Massa, C. Mitchell, Comparison of intracanopy light-emitting diode towers and overhead high-pressure sodium lamps for supplemental lighting of greenhouse-grown tomatoes, HortTechnology 23 (2013) 93–98.

[8] S. Hemming, Use of natural and artificial light in horticulture - interaction of plant and technology, Acta Horticulturae 907 (2011) 25–35.

[9] K. McCree, The action spectrum, absorptance and quantum yield of photosynthesis in crop plants, Agricultural Meteorology 9 (1971) 191–216.

[10] K. Inada, Action spectra for photosynthesis in higher plants, Plant and Cell Physiology 17 (1976) 355–365.

[11] M. Chen, R. Blankenship, Expanding the solar spectrum used by photosynthesis, Trends in Plant Science 16 (2011) 427–431.

[12] D. Kim, Y. Jin, K. Jeon, S. Kim, S. Kim, O. Han, D. Seo, J. Park, Blue-silica by Eu^{2+}-activator occupied in interstitial sites, RSC Advances 5 (2015) 74790–74801.

[13] P. Dorenbos, Energy of the first $4f^7 \rightarrow 4f^6 5d$ transition of Eu^{2+} in inorganic compounds, Journal of Luminescence 104(2003) 239–260.

[14] M. Nogami, T. Yamazaki, Y. Abe, Fluorescence properties of Eu^{3+} and Eu^{2+} in Al_2O_3–SiO_2 glass, Journal of Luminescence 78 (1) (1998) 63–68.

[15] M. Nogami, Y. Abe, Properties of sol—gel derived Al_2O_3–SiO_2 glasses using Eu^{3+} ion fluorescence spectra, Journal of Non-Crystalline Solids 197 (1996) 73–78.

[16] N. Johnson, S. He, S. Diao, E. Chan, H. Dai, A. Almutairi, Direct evidence for coupled surface and concentration quenching dynamics in lanthanide-doped nanocrystals, Journal of the American Chemical Society 139 (2017) 3275–3282.

[17] S. Sen, J. Stebbins, Structural role of Nd^{3+} and Al^{3+} cations in SiO_2 glass: a ^{29}Si MAS-NMR spin-lattice relaxation, ^{27}Al NMR and EPR study, Journal of Non-Crystalline Solids 188 (1995) 54–62.

[18] M. Lochhead, K. Bray, Rare-earth clustering and aluminum codoping in Sol-Gel silica: investigation using europium(III) fluorescence spectroscopy, Chemistry of Materials 7 (1995) 572–577.

[19] K. Arai, H. Namikawa, K. Kumata, T. Honda, Y. Ishii, T. Handa, Aluminum or phosphorus co-doping effects on the fluorescence and structural properties of neodymium-doped silica glass, Journal of Applied Physics 59 (10) (1986) 3430–3436.

[20] Z. Pan, H. He, R. Fu, S. Agathopoulos, X. Song, Influence of Ba^{2+}-doping on structural and luminescence properties of Sr_2SiO_4:Eu^{2+} phosphors, Journal of Luminescence 129 (9) (2009) 1105–1108.

[21] M. Onani, P. Mushonga, L. Koao, F. Dejene, Luminescence properties of Eu- and Mg-codoped Sol-Gel glasses, ISRN Nanotechnology(2012) 1–5.

[22] H. Fneich, N. Gaumer, S. Chaussedent, W. Blanc, A. Mehdi, Europium-doped solgel SiO_2-based glasses: effect of the europium source and content, magnesium addition and thermal treatment on their photoluminescence properties, Molecules 23 (2018) 1768.

[23] P. Jaffe, Eu^{2+} luminescence in the ternary EuO-Al_2O_3-SiO_2 system, Journal of the Electrochemical Society 16 (1969).

[24] M. Nogami, Y. Abe, Enhanced emission from Eu^{2+} ions in sol-gel derived Al_2O_3–SiO_2 glasses, Applied Physics Letters 69 (1996) 3776–3778.

[25] Y. Kishimoto, X. Zhang, T. Hayakawa, M. Nogami, Blue light emission from Eu^{2+} ions in sol-gel-derived Al_2O_3–SiO_2 glasses, Journal of Luminescence 129 (2009) 1055–1059.

[26] J. Lægsgaard, Dissolution of rare-earth clusters in SiO_2 by al codoping: A microscopic model, Physical Review B: Condensed Matter 65 (2002) 174114.

[27] F. Funabiki, T. Kamiya, H. Hosono, Doping effects in amorphous oxides, Journal of the Ceramic Society of Japan 120 (2012) 447–457.

[28] A. Patra, E. Sominska, S. Ramesh, Y. Koltypin, Z. Zhong, H. Minti, R. Reisfeld, A. Gedanken, Sonochemical preparation and characterization of Eu_2O_3 and Tb_2O_3 doped in and coated on silica and alumina nanoparticles, Journal of Physical Chemistry B 103 (1999) 3361–3365.

[29] I. Rahman, P. Vejayakumaran, C. Sipaut, J. Ismail, C. Chee, Size-dependent physicochemical and optical properties of silica nanoparticles, Materials Chemistry and Physics 114 (2009) 328–332.

[30] S. Jakka, M. Silva, M. Soares, K. Pavani, Exploring the potential of Eu^{3+} and Mn^{4+} activated $LaAlO_3$ phosphors as red and far-red emitters for horticulture lighting, RSC Advances 13 (2023) 31314–31320.

[31] K. Mishra, C. Stanghellini, S. Hemming, Technology and materials for passive manipulation of the solar spectrum in greenhouses, Advanced Sustainable Systems 7 (2023).

[32] C. Gueymard, D. Myers, K. Emery, Proposed reference irradiance spectra for solar energy systems testing, Solar Energy 73 (2002) 443–467.

[33] X. Chen, J. Jiang, F. Yan, S. Tian, K. Li, A novel low temperature vapor phase hydrolysis method for the production of nano-structured silica materials using silicon tetrachloride, RSC Advances 4 (2014) 8703–8710.

[34] D. de Graaf, H.T. Hintzen, S. Hampshire, G. de With, Long wavelength Eu^{2+} emission in Eu-doped Y-Si-Al-O-N glasses, Journal of the European Ceramic Society 23 (2003) 1093–1097.

[35] P. Selvin, T. Rana, J. Hearst, Luminescence resonance energy transfer, Journal of the American Chemical Society 116 (1994) 6029–6030.

[36] C. Wang, T. Takeda, O. Ten Kate, R. Xie, K. Takahashi, N. Hirosaki, Synthesis and photoluminescence properties of a phase pure green-emitting Eu doped JEM sialon ($LaSi_{6-z}Al_{1+z}N_{10-z}O_z$, z˜1)) phosphor with a large red-shift of emission and unusual thermal quenching behavior, Journal of Materials Chemistry C 4 (2016) 10358–10366.

[37] E. Merkx, S. van Overbeek, E. van der Kolk, Functionalizing window coatings with luminescence centers by combinatorial sputtering of scatter-free amorphous SiAlON:Eu^{2+} thin film composition libraries, Journal of Luminescence 208 (2019) 51–56.

[38] K. Kim, Y. Kim, H. Chun, T. Cho, J. Jung, J. Kang, Structural and optical properties of $BaMgAl_{10}O_{17}$:Eu^{2+} phosphor, Chemistry of Materials 14 (2002) 5045–5052.

Appendix

Table 2.1: The luminescent coating production formulation.

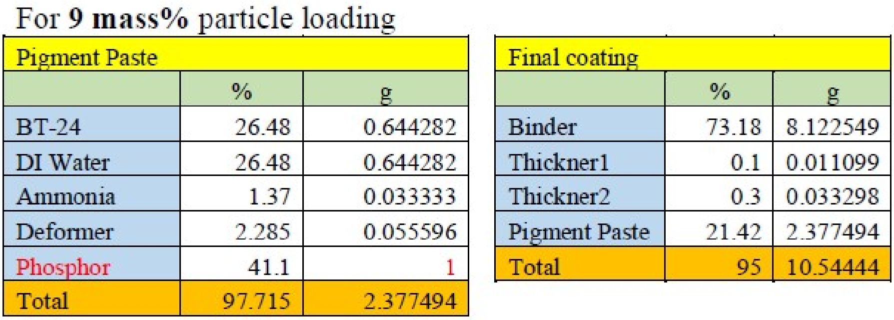

For 9 **mass%** particle loading

Pigment Paste		
	%	g
BT-24	26.48	0.644282
DI Water	26.48	0.644282
Ammonia	1.37	0.033333
Deformer	2.285	0.055596
Phosphor	41.1	1
Total	97.715	2.377494

Final coating		
	%	g
Binder	73.18	8.122549
Thickner1	0.1	0.011099
Thickner2	0.3	0.033298
Pigment Paste	21.42	2.377494
Total	95	10.54444

3

Design of tabletop hemispherical light transmittance characterization system for small scale samples

Greenhouse owners highly value the hemispherical light transmittance (T_{HEM}) of roofing materials because sunlight rarely projects at a perpendicular angle, especially in high-latitude regions. With growing interest in research of advanced multi-functional greenhouse roofing, a compact and efficient T_{HEM} characterization system for lab-scale samples is needed to promote research in the horticulture field. In this study, we developed a tabletop system capable of characterizing T_{HEM} of lab-scale samples with a size one-third of that required by the current characterization system. Key designing parameters, such as the beam cross-section area, port area, and port edge thickness were systematically varied to evaluate their impact on T_{HEM} characterization. The results indicated that the total port area should be limited to under 1% of the sphere surface area with minimized edge thickness since reflection from the edge area cannot be corrected by a double-beam measurement. Furthermore, the collimated beam cross-section area should exceed the port area by a factor of 1.5 to ensure that T_{HEM} remains unaffected by the sphere rotation center. The system provides a consistent and reliable method for T_{HEM} measurement and offers essential guidelines for future users to construct a similar setup.

The content of this chapter is based on the following publication:
Chun-Ting Cho, Johan de Haas, Erik van der Kolk, SMART AGR TECHNOL. 11 (2025) 100936.

3.1. Introduction

To tackle food shortage issues, controlled environment agriculture, such as greenhouses, has proved to be an efficient and secure way to produce food in a limited area while enhancing resource utilization and showing a strong toughness in extreme environments [1–4]. The amount of light transmitted into a greenhouse system has a large impact on every stage of plant growth and the final crop yield. Growers often assume that 1% extra light leads to 1% additional yield [5]. Although the greenhouse industry is more and more exploiting different artificial lighting methods to control the growing stage and maximize the yield, sunlight is by far the largest and free source of photosynthetically active radiation (PAR) [6–10].

Due to the natural solar trajectory during the day, the fraction of sunshine entering greenhouse coverings under a perpendicular angle is relatively small in high-latitude areas such as the United Kingdom and the Netherlands [11]. In addition, diffuse radiation dominates the total amount of daylight, especially in winter [12]. Therefore, the hemispherical light transmittance (T_{HEM}) of a greenhouse roofing is a more important optical property compared to the perpendicular light transmittance (or direct transmittance) for greenhouse owners and glass manufacturers. In 2008, Hemming et al. proposed a method to characterize T_{HEM} of greenhouse covering materials [12]. After the publication, a protocol for experimentally determining the hemispherical light transmittance was developed by Wageningen University and Research (WUR) [13, 14]. The protocol established the characterization principles, procedures, and standards for hemispherical light transmittance measurement. An experimental facility, Transvision, was constructed to measure T_{HEM} following these protocols. It features a high-power Xenon lamp to mimic the solar spectrum and a 1-meter integrating sphere to integrate all transmitted light, regardless of angle, allowing for the testing of large coated or non-coated sample plates with a minimum size of 200 cm² [15]. The AM1.5g solar spectrum is presented in the Appendix. Later, in 2018, this protocol was replaced by the Dutch Norm NEN-2675+C1:2018 (NEN-2675), which regulates the characterization method by the Netherlands government, providing more detailed characterization guidelines [16]. Hemming et al. characterized several conventional greenhouse roofing materials and reported the perpendicular transmittance and hemispherical light transmittance information of these materials using the Transvision system [17].

The interest in advanced greenhouse roofing with a wide range of functionalities such as solar spectral conversion [18–22], light scattering [23–26], and shading [27–30] has grown rapidly over the past decade. Nonetheless, it is challenging for research groups to build a 200 cm² homogeneous sample to test its T_{HEM} in the WUR Transvision system. This large-scale apparatus is accessible only to specialized laboratories, limiting public access to the resulting data and hindering broader acceptance. Therefore, there is a clear need for a tabletop T_{HEM} characterization setup suitable for lab-scale homogeneous samples smaller than 200 cm². However, experimental data indicates that simply scaling down optical setups introduces systematic uncertainties that were previously thought to be insignificant. Additionally, there is a lack of clear guidance on design parameters in the NEN-2675 document. For instance, the edge thickness of the integrating sphere sample port can influence the T_{HEM} value, but this issue is not addressed in NEN-2675.

In this paper, we present a tabletop hemispherical light transmittance characterization setup for a small-scale sample. We thoroughly detail its design parameters, including light beam cross-section area, integrating sphere port area and port-edge thickness, and discuss their influence on systematic uncertainties.

3.2. Experimental method

3.2.1. Equipment and benchmark sample

An overview of the most important components of the proposed T_{HEM} tabletop setup can be seen in Fig. 3.1, which schematically shows all components that are as follows: (i) a light source (ii) an achromatic lens (iii) a beam stopper (iv) an integrating sphere with a sample port, a reference port, and a baffle inside, (v) an optical fiber connected to a spectrometer, (vi) a rotation and a linear translation stage by which the angle of incidence and the position of the rotation axis can be controlled as indicated in the figure, and finally (vii) a test sample. These components are discussed in more detail below.

(i) A powerful 150W halogen lamp (64640 HLX, Osram) installed on a G6.35 lamp socket with an AC power supply was used as the light source in our setup. The lamp has a filament of 5.8 mm (width) × 2.9 mm (height). We chose a tungsten lamp instead of the xenon lamp because it has no sharp spectral features and has sufficient intensity between 400 nm and 700 nm needed for the calculation of T_{HEM}. (ii) A doublet achromatic lens (14 cm in diameter, 1900 mm focal length, Edmund Optics) served to collimate the light emitted from the lamp, ensuring a parallel beam necessary for accurate measurement. Due to the lamp filament not being a point source, a perfect 0° divergence cannot be achieved. For all the tests in this study, the default beam divergence was set to the minimum (~0°). (iii) The beam stopper located behind the achromatic lens served to control the beam diameter. (iv) A home-built 30 cm diameter integrating sphere allowed for easily interchanging ports with varying diameters. The interior of the sphere was coated with diffusive barium sulfate (Gigahertz-Optik). The interiors of all exchangeable ports were also coated with barium sulfate. Besides the exchangeable port, the integrating sphere has an additional port referred to as “reference port” for the double beam measurement, as explained later in more detail in section 3.2.2. (v) An optical fiber (FC-UVIR600-1, Avantes) connected the spectrometer port to the spectrometer (QE65Pro, Ocean Optics) to measure the light intensity captured by the integrating sphere. (vi) The rotation stage (HDR50, Thorlabs) served to automatically rotate the integrating sphere so that the incident angle of the beam could be controlled from 0° to 75°. A linear translation stage was installed to adjust the position of the rotation axis. (vii) A 4 mm thick Optiwhite (Pilkington) glass with a reported direct transmittance of 92% and hemispherical light transmittance of 84% (measured by WUR Transvision system) was used as the benchmark sample for all the measurements in this research. In our system, a beam splitter to project the light beam on the reference port is not needed. Instead, we manually rotated the whole integrating sphere by 90° to exchange the position of the sample port and the reference port.

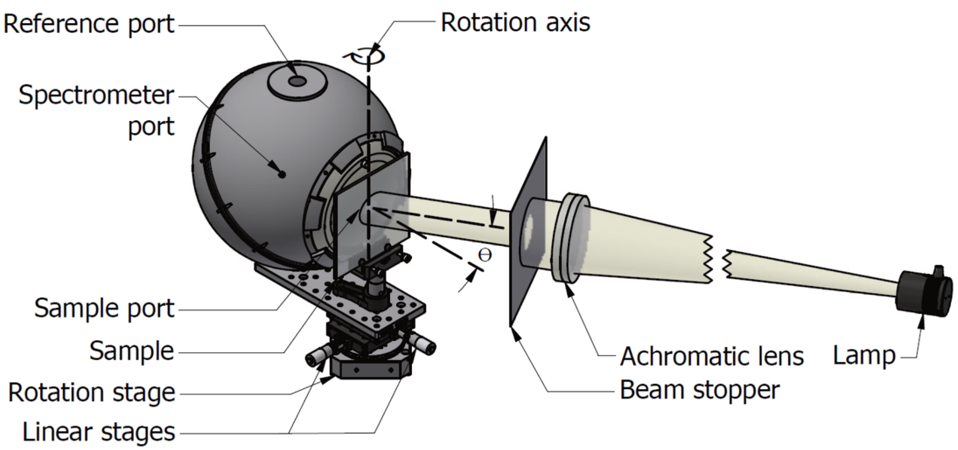

Figure 3.1: Illustration of the whole tabletop hemispherical light transmittance characterization setup.

3.2.2. Measurement procedure

According to NEN-2675, the transmittance measurement of samples is performed for at least eight incident angles (θ = 0°, 15°, 30°, 40°, 45°, 50°, 60°, and 75°), with each measurement referred to as an angular-spectral transmittance ($T_{\lambda,\theta,\phi}$) for a fixed azimuthal angle ϕ (in standard spherical coordinates) and a wavelength range between 400 nm and 700 nm [16]. The transmittance of a material is defined as the ratio of the transmitted light intensity (Fig. 3.2a) to the incident light intensity (Fig. 3.2b). The latter is recorded without a sample and is referred to as the reference or lamp measurement. The transmittance measurement performed with an integrating sphere usually overestimates the transmittance. This is because a fraction of the light that enters the integrating sphere (in the reference measurement without a sample) exits the sphere through the sample port after many diffuse reflections within the sphere. This fraction is, however, not the same when a sample is present due to the reflections at the sample surface that do not occur without the sample located in front of the measuring port. This difference can be quantified and thereby corrected through a so-called double-beam measurement (Fig. 3.2c and d) as described in the NEN-13468-2-2021 document [31]. The measurement steps for a comprehensive T_{HEM} characterization are described below and shown in Fig. 3.2.

(a) Sample port is illuminated with sample in the sample port. The measured light intensity is $I_{\lambda,\theta,\phi,1}$.

(b) Sample port is illuminated without sample in the sample port. The measured light intensity is $I_{\lambda,\theta,\phi,2}$.

(c) Reference port is illuminated without sample in the sample port. The measured light intensity signal is $I_{\lambda,\theta,\phi,3}$.

(d) Reference port is illuminated with sample in the sample port. The measured light intensity is $I_{\lambda,\theta,\phi,4}$.

All measured light intensities are corrected to exclude dark noise from the background. Based on measurements (a) through (d), the corrected angular-spectral transmittance $T_{\lambda,\theta,\phi}$ is as below:

$$T_{\lambda,\theta,\phi} = \frac{I_{\lambda,\theta,\phi,1}}{I_{\lambda,\theta,\phi,2}} \times \frac{I_{\lambda,\theta,\phi,3}}{I_{\lambda,\theta,\phi,4}} \tag{3.1}$$

The term $I_{\lambda,\theta,\phi,3}/I_{\lambda,\theta,\phi,4}$ is referred to as the double-beam coefficient which corrects for the over-estimated transmittance described above.

Note that the double-beam coefficient strongly depends on the probability that light scattered around within the integrating sphere exits the sphere through the sample port. A larger port represents a larger probability of light escaping. This probability is independent of where light first hits the integrating sphere after entering through the sample port. However, we hypothesize that this probability is much higher for light that strikes the edge of the sample port after entering through the sample port, potentially reaching an escape probability as high as 50%, which is much higher than that of light hitting the sphere's inner surface after entering through the sample port. We will show that, indeed, these so-called edge thickness effects are not corrected for by a double-beam experiment and, therefore, must be minimized.

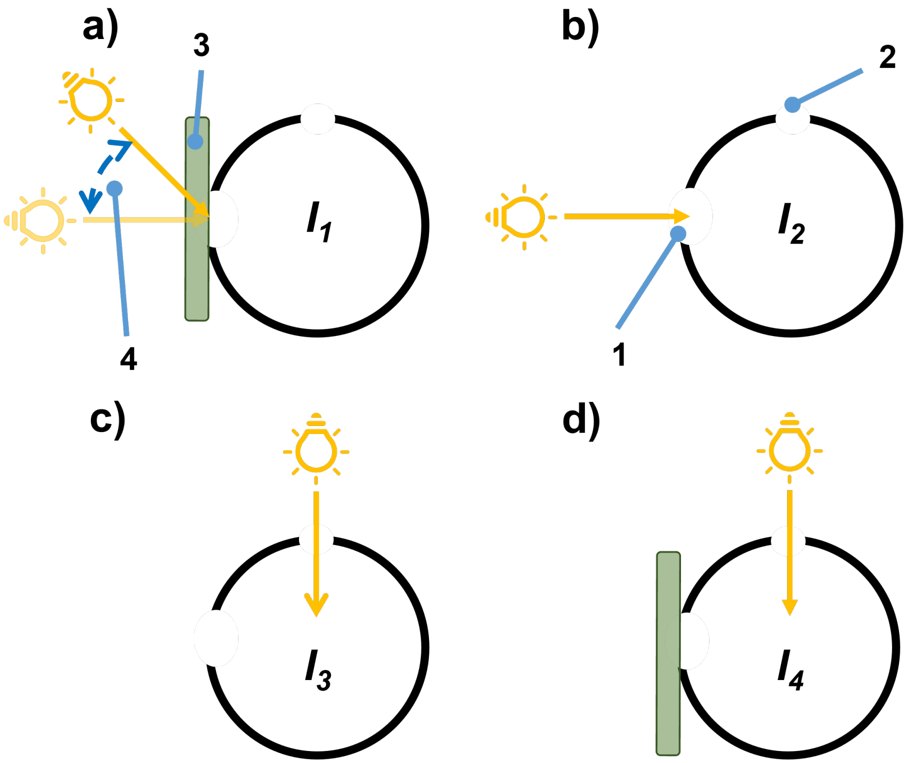

Figure 3.2: Illustration of measurement steps a to d. 1: the sample port. 2: the reference port. 3: sample. 4: the angle of incidence θ.

3.2.3. Calculation of hemispherical light transmittance T_{HEM}

The hemispherical light transmittance T_{HEM} is calculated by the angle-dependent transmittance $T_{\theta,\phi}$ through numerical integration over the wavelength of the previously described angular-spectral transmittance $T_{\lambda,\theta,\phi}$:

$$T_{\theta,\phi} = \frac{\int_{400}^{700} A_\lambda \times T_{\lambda,\theta,\phi} d\lambda}{\int_{400}^{700} A_\lambda d\lambda} = 0.00045 \times \int_{400}^{700} A_\lambda \times T_{\lambda,\theta,\phi} d\lambda \tag{3.2}$$

Where A_λ is the product of the relative spectral density of solar radiation and relative plant sensitivity function in the PAR range that is defined by the NEN-2675. The hemispherical light transmittance T_{HEM} is calculated from the angle-dependent transmittance $T_{\theta,\phi}$ according to the equation:

$$T_{HEM} = \frac{\int_0^{2\pi} \int_0^{\pi/2} T_{\theta,\phi} \times S_{\theta,\phi} \times sin(\theta) \times cos(\theta) d\theta d\phi}{\int_0^{2\pi} \int_0^{\pi/2} S_{\theta,\phi} \times sin(\theta) \times cos(\theta) d\theta d\phi} \tag{3.3}$$

In this formula, ϕ represents an azimuthal angle (in standard spherical coordinates) and $S_{\theta,\phi}$ represents a solar luminance distribution function. We assume the "standard uniform sky" (for which S = 1) is applied. It can be defined otherwise in case the luminance distribution changes with latitude and azimuth. Note that the azimuthal angle ϕ is not relevant in our study due to the glass sample used being homogeneous without anisotropic surface modification. In the case of an inhomogeneous sample, measurements need to be taken at different azimuthal angles ϕ as defined in NEN-2675.

3.2.4. Beam profile

The beam profile of the light source was measured using an optical fiber (FC-UVIR600, Avantes) with a 100 um pinhole in front connected to a spectrometer (QE65Pro, Ocean Optics). The inlet of the optical fiber faced the light source, and its position was controlled by an automated linear translation stage (DDS100, Thorlabs) moving horizontally across the centerline of the beam to measure the profile.

3.2.5. Design parameters

To determine the required dimensions of our tabletop T_{HEM} characterization system, several design parameters were tested to establish that T_{HEM} remains independent within a certain range of specific parameters, indicating the absence of systematic uncertainties. These parameters are discussed below. Note that NEN-2675 implicitly suggests the rotation center of the integrating sphere (as shown by the rotation axis in Fig. 3.1) should align with the sample port plane. We performed a simple test to determine the position of the rotation center, which shows no difference when applying a highly collimated light beam that is larger than the port area, as demonstrated in the Appendix.

Port-to-sphere surface area ratio

The port area introduces a systematic error, resulting in an overestimation of T_{HEM}, as explained in section 3.2.2. This error can be corrected by using the double-beam coefficient. The goal of this section is to validate the correction function of the double-beam coefficient. Three interchangeable ports with different diameters (25, 50, and 100 mm) were produced. The ratios of the total port area to the total sphere surface area (referred to as the "port-to-sphere surface area ratio") are 0.35%, 0.87%, and 2.95%, respectively.

Port edge thickness

Prior to this study, we observed that the "edge thickness" of the sample port, as illustrated in Fig. 3.3, influenced the T_{HEM} value. When a light beam with a high angle of incidence (large value for θ strikes the integrating sphere with a thick edge, a large fraction of light first undergoes a Lambertian reflection at the edge area before reaching the inner sphere surface. Due to the location of the edge area being very close to the port opening, approximately half of the reflected light (assuming an ideal Lambertian scattering surface) escapes through the port when no sample is present. In contrast, when light first hits the sphere's inner surface rather than the edge area, the probability of it leaving the port is proportional to the ratio of the port area to the total sphere inner surface area, which is in the order of a few % [32]. This phenomenon introduces uncertainties in T_{HEM} calculation, which grow larger when the edge area increases, as further explained in Fig. 3.4.

To investigate the impact of port edge thickness on the T_{HEM} value, four interchangeable ports (the sample port in Fig. 3.1) with varying edge thicknesses (0.4, 1, 2, and 6 mm) and a fixed port diameter of 25 mm were produced. The design details are provided in Fig. 3.3. The reference port has a diameter of 25 mm and an edge thickness of 0.4 mm.

Beam-to-port area ratio

The direction of light propagation changes upon entering a medium with a different refractive index, such as from air (n = 1) to glass (n = 1.5), due to refraction. The refraction within the glass results in a lateral shift in the light path [33]. In addition, the circular illumination area (referred to as "beam cross-section area") of a collimated incident beam (at $\theta = 0°$) expands into an elliptical shape at higher angles of incidence. The semi-major axis length of the ellipse is inversely proportional to $\cos(\theta)$, while the semi-minor axis remains the same as the radius of the original beam. Based on the area equations for

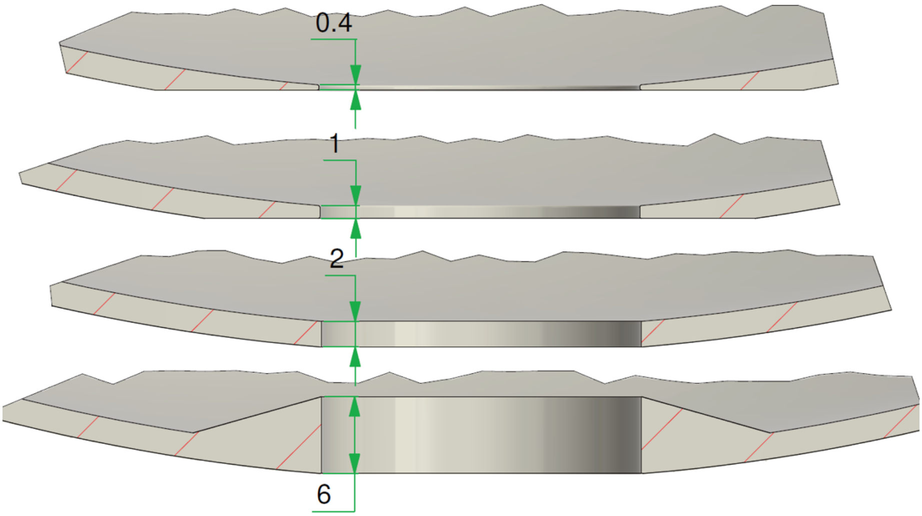

Figure 3.3: Illustration of the sample port edge with different thicknesses, 0.4, 1, 2, 6 mm on a 25 mm diameter port.

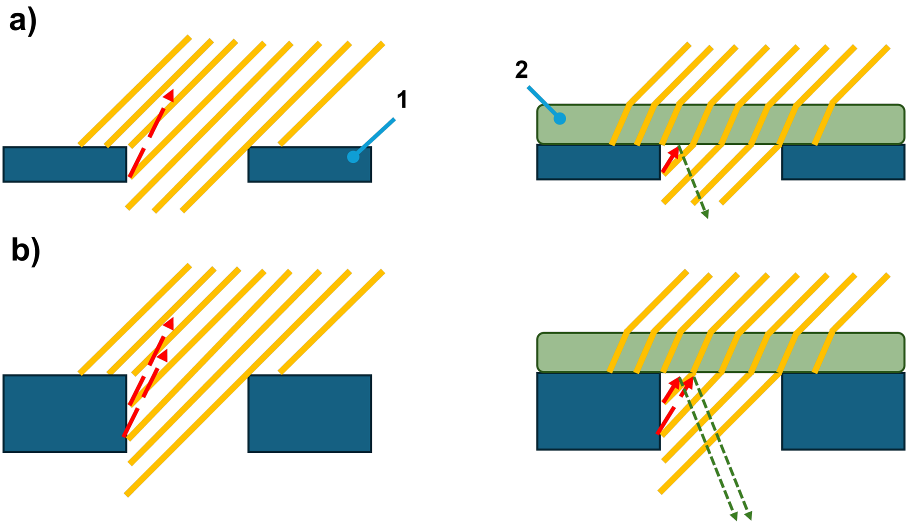

Figure 3.4: Illustration of edge reflection on ports. 1: port edge. 2: sample. a) Small edge thickness. b) Large edge thickness. At large angles of incidence θ, a large fraction of light hits the port edge instead of entering the sphere. Red arrows represent light reflected from the edge area, while green arrows represent light reflected back from the sample into the sphere.

an ellipse and a circle, the area of the expanded ellipse follows an inverse relationship with $\cos(\theta)$ as $A' = A/\cos(\theta)$, where A is the original circular illuminating area of the beam when the incident angle is 0°, and A' is the expanded illuminating area at a given incident angle. This area-expansion effect, combined with the aforementioned lateral shift in light, impacts the T_{HEM} to an extent depending on the area ratio between the beam and the port, which is referred to as “beam-to-port area ratio”.

When applying a beam with a beam cross-section area that is approximately the same size as the port area, a systematic error can occur. This is because the fractions of light entering the sphere with and without the sample differ due to the lateral shift effect discussed previously, which means some portions of the light can be blocked by the sphere wall, as shown in Fig. 3.5a. Utilizing a collimated light beam with a cross-section area that is sufficiently larger than the port area can minimize this problem since the fraction of light after the lateral shift is the same with and without a sample as shown in Fig. 3.5b. This is also discussed in the NEN-2675 document, stating that: the illuminating area should be at least 15% larger than the size of the sample port.

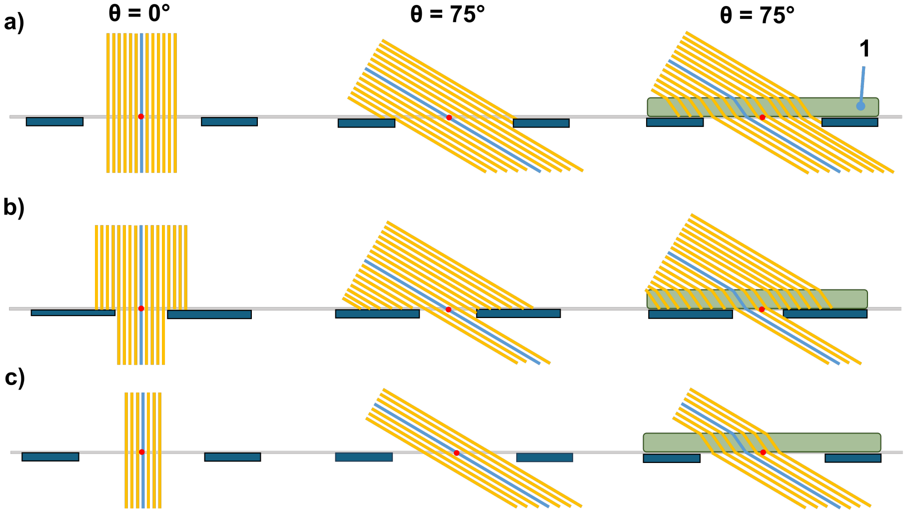

Figure 3.5: Illustration of conditions of different beam cross-section area to port area at 0° and 75° angle of incidence. 1: sample. a) The beam cross-section area is smaller than the port. b) The beam cross-section area is much larger than the port. c) The beam cross-section area is much smaller than the port.

Swinkels discussed the possibility of using a beam that is much smaller than the port area [15]. The issue of the sphere receiving different fractions of light could be potentially minimized if all the light exiting the glass sample were collected by the integrating sphere; in other words, no light is blocked by the sphere wall, as shown in Fig. 3.5c. In the results, we show that this might be true but only when the divergence of the beam is sufficiently small (~0°).

To determine the required beam-to-port area ratio for our tabletop characterization system, we applied different-sized beam stoppers to adjust the beam cross-section area and tested these beams with ports of varying diameters. This allowed us to evaluate the combined influence of beam cross-section area and port area on the T_{HEM} value. The ratio of the beam cross-section area to the port area, referred to as “beam-to-port area ratio”, serves to be a practical parameter for future users designing setups to accurately measure T_{HEM}.

3.3. Results and discussions

3.3.1. The influence of port-to-sphere surface area ratio

To ensure a fair comparison of the influence of varying port areas, the measurements were conducted at a beam-to-port area ratio of 144% for the three ports with a small port edge thickness of 0.4 mm. The significance of the double-beam coefficient in T_{HEM} characterization is illustrated in Fig. 3.6, which compares T_{HEM} values with and without applying the double-beam coefficient.

When applying the double-beam coefficient, the T_{HEM} values decreased only slightly from 85.5% to 85.1% as the port area increased, remaining within the ±1% acceptance range defined by NEN-2675. In contrast, the T_{HEM} without applying a double-beam coefficient ($I_{\lambda,\theta,\phi,3}/I_{\lambda,\theta,\phi,4} = 1$ in equation) increased from 86.2% to 91.4%. The result indicated that the double-beam coefficient effectively corrects the overestimation of T_{HEM}.

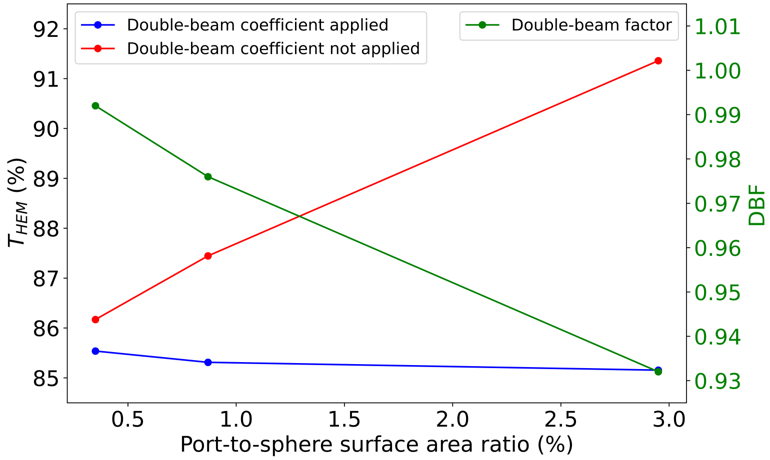

Figure 3.6: The T_{HEM} of the 25 mm, 50 mm, and 100 mm ports with and without the correction of double-beam coefficient, and the double-beam factor (DBF). The ratio of total port area to sphere surface area for 25 mm, 50 mm, and 100 mm ports is 0.35%, 0.87%, and 2.95%, respectively. All the ports have an edge thickness of 0.4 mm. The applied beam-to-port area ratio is 144%.

The influence of applying the double-beam coefficient was quantified by the term “double-beam factor (DBF)”, which is a wavelength- and angular-integrated double-beam coefficient derived from Eq. 3.1 by setting $I_{\lambda,\theta,\phi,1}/I_{\lambda,\theta,\phi,2} = 1$. The DBF indicates the extent of correction conducted by the double-beam measurement: a DBF of 1 means no correction, while smaller DBF values indicate a greater extent of correction. Due to equipment limitations, a further increase in the port area was not feasible in this study. However, the result demonstrated a trend of T_{HEM} following NEN-2675 regulation, which states that the total port area should not exceed 3% of the total sphere surface area. To preserve the functionality of the integrating sphere with a minimal correction factor, we recommend keeping the total port area below 1% of the total sphere surface area. Note that the double-beam coefficient for the three ports with different diameters is independent of the angle of incidence (θ) as demonstrated in the Appendix.

3.3.2. The influence of port edge thickness

In section 3.2.5, we explained that light directly hitting the edge of the sample port introduces a systematic error in T_{HEM} that cannot be corrected by a double-beam factor. Therefore, we expected the systematic error to increase with the edge thickness. To evaluate this, a 40 mm beam was applied to 25 mm ports, each with different edge thicknesses (0.4, 1, 2, 6 mm).

As shown in Fig. 3.7, T_{HEM} increases from 85.5% to 88.5% (blue curve, with double-beam correction) and from 86.1% to 89.0% (red curve, without double-beam correction) when the edge thickness increases from 0.4 mm to 6 mm. The result demonstrated that the double-beam coefficient could not correct the T_{HEM} for different edge thicknesses as in Fig. 3.6. This is confirmed by the green curve in Fig. 3.7, which shows just a minor change in the DBF value when varying the edge thickness from 0.4 mm to 6 mm showing that the DBF is independent of the edge thickness.

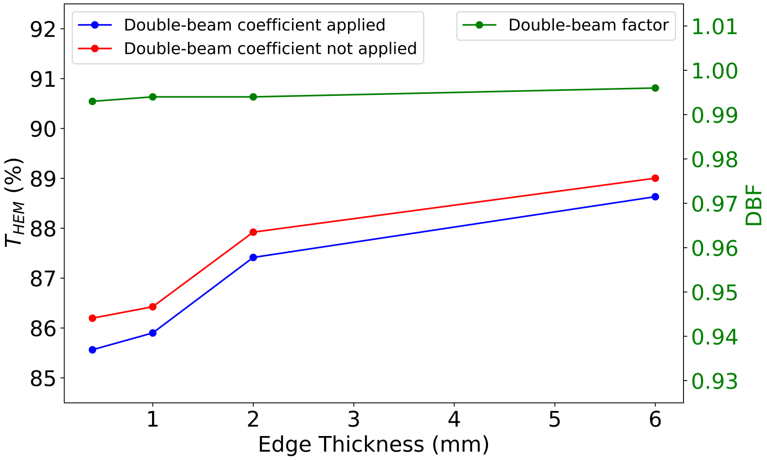

Figure 3.7: The T_{HEM} of 25 mm ports with edge thickness 0.4, 1, 2, and 6 mm ports with and without the correction of double-beam coefficient, and the double-beam factor (DBF). A 40 mm beam was applied to the ports.

A deeper understanding of the influence of the edge thickness on T_{HEM} is presented in Fig. 3.8. The angular transmittance of the ports with the thinnest edge (0.4 and 1 mm) shows a decrease with increasing incident angles as predicted by Fresnel's equations, as illustrated by the red curve in Fig. 3.8b. A similar result was obtained by Hemming et al. [34]. However, the angular transmittance for the 2 mm and 6 mm port edge thicknesses shows an increase (up to 3%) in transmittance as a function of the angle between $\theta = 30°$ and 50° compared to $\theta = 0°$, which contradicts Fresnel's equations. The observed higher transmission for larger angles can only be explained by the effect of the increased edge surface, as discussed previously. Based on this observation, we recommend designing

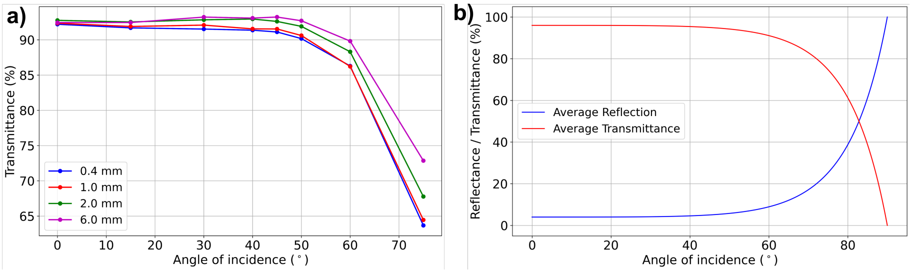

Figure 3.8: a) The angular transmittance of 25 mm ports with edge thicknesses 0.4, 1, 2, and 6 mm. b) The transmittance and reflectance of light entering the air (n = 1) from Optiwhite (n = 1.5) based on Fresnel equations.

the port edges as thin as possible, in this study, less than 1 mm for a 25 mm port. This edge effect is negligible for the WUR Transvision system since the port diameter of the Transvision system is large (170 mm) compared to the thickness of the integrating sphere edge (which can be up to 10 mm). While we acknowledge that additional experiments, particularly those systematically varying port-edge thickness across a broader range of port diameters, could further reinforce our findings, the current results provide sufficient guidance for designing a down-scaled system.

3.3.3. The influence of beam-to-port area ratio

In this section, we present the results of the beam-to-port area ratio test conducted on three different sizes of ports (25 mm, 50 mm, and 100 mm) with an edge thickness of 0.4 mm. Fig. 3.9 illustrates the T_{HEM} as a function of the beam-to-port area ratio for the three ports. The T_{HEM} values for 25 mm and 50 mm ports remained stable when the beam cross-section area exceeded the port area by a factor of 1.5 (150% beam-to-port area ratio). However, when the T_{HEM} was measured with a smaller beam-to-port area ratio (<150%), the results showed a decreasing trend due to some fractions of the light being blocked by the sphere wall, as discussed in section 3.2.5. Specifically for the 25 mm port, the result of the 4% beam-to-port area ratio beam gave a 5.5% difference in T_{HEM} compared to the T_{HEM} above 150% beam-to-port area ratio, while the other two ports gave only a difference of about 1-1,5% as can be seen in Fig. 3.9b.

The fact that there is a difference, and more generally, that the T_{HEM} value at small ratios is not the same as the value measured at large ratios, is attributed to the light beam not being perfectly collimated and lacking a block-shaped beam profile. This shortcoming is more pronounced for beams with smaller diameters. The beam profile deviating from a perfect block-shape is illustrated by the yellow area in Fig. 3.10. Especially for smaller diameter beams, the low-intensity illuminating ring (blue area) surrounding the uniform block-shaped beam (yellow area) is relatively large. As shown in Fig. 3.10, light passing through a 5 mm beam stopper contains a larger fraction of the imperfect illuminating region compared to the central collimated area than light passing through a 10 mm beam stopper. According to Snell's law, a 75° incident angle refracts to 40° inside the

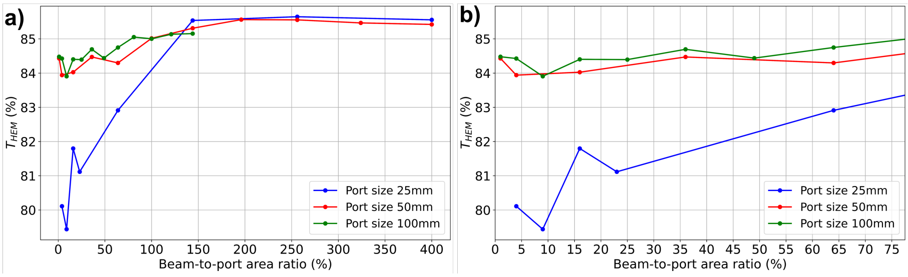

Figure 3.9: a) The T_{HEM} of various beam-to-port area ratios on the exchangeable ports of 25 mm, 50 mm, 100 mm. b) The zoom-in of a). All the ports have an edge thickness of 0.4 mm.

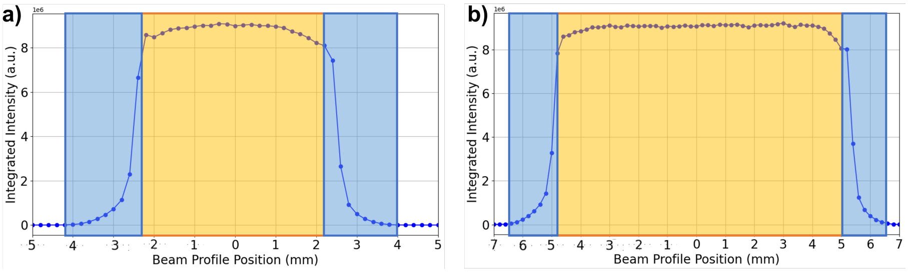

Figure 3.10: The beam profile of a) light passing through a 5 mm beam stopper and b) light passing through a 10 mm beam stopper. The central part of the beam with homogeneous light intensity is marked with yellow color. The imperfect illuminating region of the beam is marked with blue color.

glass, while the critical angle for total internal reflection (TIR) from air (n = 1) to Optiwhite glass (n = 1.5) is 41.9°. We believe that the imperfect illuminating region contains non-collimated beams that exceed the TIR angle after refraction in the glass, leading to reduced transmittance at $\theta = 75°$ for the 25 mm port compared to the larger ports with the same beam-to-port area ratio (Fig. 3.11), resulting in the great difference in the T_{HEM} values. Additionally, we note that multiple reflections at such large angles of incidence might lead to the reduced transmittance if part of the beam undergoes higher-order reflections in the 25 mm port. However, this alone cannot fully explain why no difference was observed in the larger ports (Fig. 3.11b).

Based on the observation, the concept of using a beam much smaller than the port area, with a sufficiently low beam divergence, may be feasible for achieving the same T_{HEM} as applying a beam that is 50% larger than the port area. However, achieving such low divergence is particularly challenging when working with small beam diameters and basic optical components, such as the extended light source used in our study. The result indicated that the beam cross-section area should exceed the port area (over 150%) to obtain a steady result in this study. Based on this observation, we recommend applying a beam with the cross-section area being at least 50% larger than the port area for a stable result.

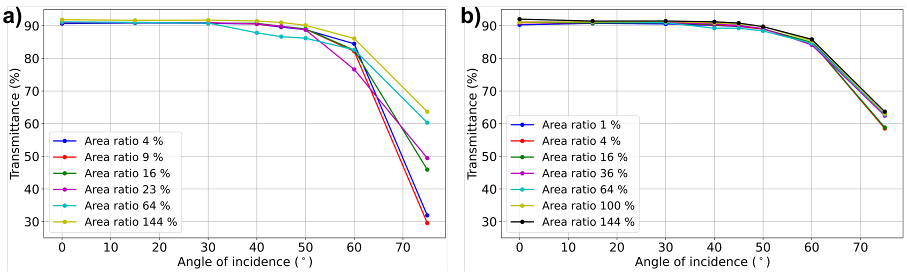

Figure 3.11: The angular transmittance of different beam-to-port area ratio of a) 25 mm port. b) 50 mm port.

3.3.4. Repeatability test

Based on the results of the tests above, we determined the optimal parameters for our desktop system and conducted a repeatability test. The applied parameters were the 25 mm diameter port with 0.4 mm thickness, a 40 mm diameter beam with ~0° beam divergence, and the rotation center aligned with the same plane as the sample port. Table 3.1 shows the angular transmittance of 4 mm Optiwhite characterized by WUR Transvision system and by our system based on a 20x repeatability test of removing and repositioning the sample. Figure 3.11 shows the standard deviation result of our test. The standard deviation of our setup is comparable to that of WUR Transvision system. Our results demonstrated that the spread in T_{HEM} is within ±1%, which falls within the acceptable range regulated by NEN-2675.

Table 3.1: Comparison of angular transmittance, standard deviation, and T_{HEM} of Optiwhite glass characterized by WUR Transvision system and by our setup.

Angle of incidence (θ)	**0°**	**15°**	**30°**	**40°**	**45°**	**50°**	**60°**	**75°**	**T_{HEM}**
WUR Transvision									
Transmittance (%)	91.61	91.57	91.29	90.52	89.92	88.97	84.04	61.03	84.32
Std. (%)	0.045	0.058	0.087	0.029	0.078	0.013	0.041	0.043	0.008
This work									
Transmittance (%)	92.11	91.72	91.69	91.37	90.89	90.02	85.96	63.61	85.49
Std. (%)	0.068	0.049	0.073	0.086	0.088	0.081	0.134	0.120	0.05

3.3.5. Required sample dimension

Based on the area-expansion equation mentioned in section 3.2.5, the semi-major axis of the expanded ellipse becomes 3.86 times the original radius of the incident beam at a 75° angle of incidence, and the semi-minor axis of the ellipse remains unchanged at

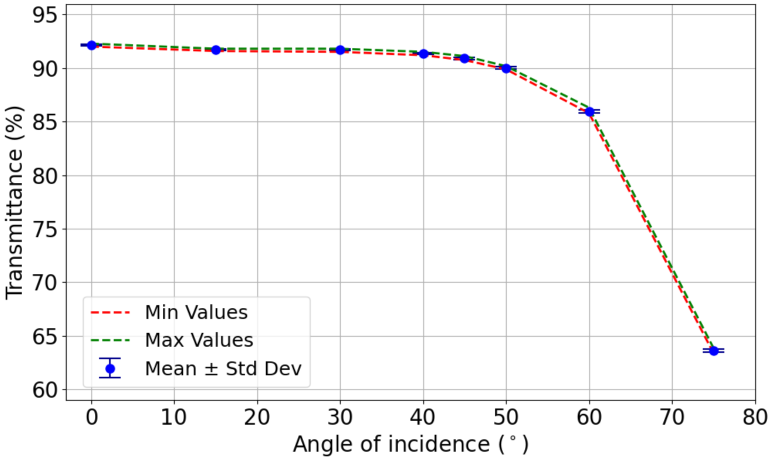

Figure 3.12: The angular transmittance and standard deviation analysis of 20 tests on the Optiwhite sample using the optimal parameters.

the original beam radius. For a 40 mm incident beam, the minimum required length of the sample is four times the diameter (160 mm), while the minimum width can be 45 mm, which is slightly larger than the beam diameter to be illuminated by the full incident beam. Thus, the minimum required sample is one-third (72 cm^2) of the required dimension of the WUR Transvision system. A smaller sample dimension can be achieved if a smaller beam is used. It is important to note that the target samples characterized by this setup should be homogeneous and free of distinct repeating patterns.

3.4. Conclusion

A compact, tabletop system has been successfully developed to characterize the hemispherical light transmittance (T_{HEM}) of lab-scale samples. A commercial product with known T_{HEM} was used to benchmark the influence of these design parameters. Key findings indicated that the port edge thickness should be minimized to reduce edge reflection effects, and the port area should be kept below 1% of the total sphere surface area to ensure accurate measurements. Furthermore, the applied beam cross-section area should exceed the port area by at least 150% to maintain measurement stability. Results further highlight the importance of maintaining a low beam divergence (close to 0°) and aligning the rotation center with the plane of the sample port to minimize potential discrepancies, particularly for small beam diameters. The minimum required sample length should be four times the applied beam cross-section area, while the width should be sufficient to ensure a full beam illumination. These findings provide essential design guidelines for building customized tabletop characterization systems, enabling research groups to characterize small-scale samples efficiently and reproducibly. By making T_{HEM} characterization more accessible to research groups, this system can accelerate the development of advanced optical coatings. In the long run, such innovations can be transferred to commercial greenhouse roofing products, benefiting greenhouse farmers through improved light management and potentially higher crop yields.

References

[1] D. Zhou, H. Meinke, M. Wilson, L. Marcelis, E. Heuvelink, Towards delivering on the sustainable development goals in greenhouse production systems, Resources, Conservation and Recycling 169 (2021).

[2] P. Zabel, M. Bamsey, D. Schubert, M. Tajmar, Review and analysis of over 40 years of space plant growth systems, Life Sciences in Space Research 10 (2016) 1–16.

[3] C. Maraveas, Environmental sustainability of greenhouse covering materials, Sustainability 11 (2019).

[4] R. Giacomelli, Gene A., Greenhouse covering systems, HortTechnology (1993).

[5] L. Marcelis, A. Broekhuijsen, E. Meinen, E. Nijs, M. Raaphorst, Quantification of the growth response to light quantity of greenhouse grown crops, Acta Horticulturae 711 (2006) 97–103.

[6] M. Jones, Using light to improve commercial value, Horticulture Research 5 (2018).

[7] J. Nelson, B. Bugbee, Economic analysis of greenhouse lighting: Light emitting diodes vs. high intensity discharge fixtures, PLoS ONE 9 (2014).

[8] E. Kaiser, T. Ouzounis, H. Giday, R. Schipper, E. Heuvelink, L. Marcelis, Adding blue to red supplemental light increases biomass and yield of greenhouse-grown tomatoes, but only to an optimum, Frontiers in Plant Science 9 (2019) 1–11.

[9] C. Gomez, R. Morrow, C. Bourget, G. Massa, C. Mitchell, Comparison of intracanopy light-emitting diode towers and overhead high-pressure sodium lamps for supplemental lighting of greenhouse-grown tomatoes, HortTechnology 23 (2013) 93–98.

[10] S. Hemming, Use of natural and artificial light in horticulture - interaction of plant and technology, Acta Horticulturae 907 (2011) 25–35.

[11] P. Rajendran, H. Smith, Modelling of solar irradiance and daylight duration for solar-powered UAV sizing, Energy Exploration and Exploitation 34 (2016) 235–243.

[12] S. Hemming, V. Mohammadkhani, T. Dueck, Diffuse greenhouse covering materials - Material technology, measurements and evaluation of optical properties, Acta Horticulturae 797 (2008) 469–476.

[13] J. Ruigrok, G. Swinkels, Lichtmeetprotocol Kasdekmaterialen Samenvatting (2010) 27.

[14] G. Swinkels, S. Hemming, V. Mohammadkhani, J. Van Ruijven, Rapport GTB-1252 Protocol for measuring light transmission of horticultural screens (2012).

[15] G. Swinkels, Transvision: A light transmission measurement system for greenhouse covering materials, Acta Horticulturae 956 (2012) 563–568.

[16] Nederlands Normalisatie-instituut, NEN 2675+C1 Greenhouse glass - Determination of optical properties of greenhouse covering materials and screens, Tech. rep. (2018).

[17] S. Hemming, G. Swinkels, A. Van Breugel, V. Mohammadkhani, Evaluation of diffusing properties of greenhouse covering materials, Acta Horticulturae 1134 (2016) 309–316.

[18] C. Cho, G. Bosco, E. van der Kolk, The potential of SiO_2:Al^{3+},Eu^{2+} blue phosphor coatings in greenhouse application, Optical Materials 157 (2024) 2–8.

[19] K. Mishra, C. Stanghellini, S. Hemming, Technology and Materials for Passive Manipulation of the Solar Spectrum in Greenhouses, Advanced Sustainable Systems 7 (2023).

[20] S. K. Jakka, M. Silva, M. Soares, K. Pavani, Exploring the potential of Eu^{3+} and Mn^{4+} activated $LaAlO_3$ phosphors as red and far-red emitters for horticulture lighting, RSC Advances 13 (2023) 31314–31320.

[21] C. Parrish, D. Hebert, A. Jackson, K. Ramasamy, H. McDaniel, G. Giacomelli, M. Bergren, Optimizing spectral quality with quantum dots to enhance crop yield in controlled environments, Communications Biology 4 (2021) 1–9.

[22] R. Yalcın, H. Ertürk, Improving crop production in solar illuminated vertical farms using fluorescence coatings, Biosystems Engineering 193 (2020) 25–36.

[23] S. Hemming, T. Dueck, J. Janse, F. Van Noort, The effect of diffuse light on crops, Acta Horticulturae 801 (2008) 1293–1300.

[24] F. Kempkes, C. Stanghellini, N. Victoria, M. Bruins, Effect of diffuse glass on climate and plant environment: First results from an experiment on roses, Acta Horticulturae 952 (2012) 255–262.

[25] T. Dueck, J. Janse, T. Li, F. Kempkes, B. Eveleens, Influence of diffuse glass on the growth and production of tomato, Acta Horticulturae 956 (2012) 75–82.

[26] R. Yalcin, H. Erturk, Improving photosynthetic efficiency using greenhouse coatings with scattering and fluorescent pigments, Materials Research Express 6 (2019).

[27] A. Baille, C. Kittas, N. Katsoulas, Influence of whitening on greenhouse microclimate and crop energy partitioning, Agricultural and Forest Meteorology 107 (2001) 293–306.

[28] H. Aldaftari, J. Okajima, A. Komiya, S. Maruyama, Radiative control through greenhouse covering materials using pigmented coatings, Journal of Quantitative Spectroscopy and Radiative Transfer 231 (2019) 29–36.

[29] T. Li, Y. Gao, K. Zheng, Y. Ma, D. Ding, H. Zhang, Achieving better greenhouse effect than glass: Visibly transparent and low emissivity metal-polymer hybrid metamaterials, ES Energy and Environment 5 (2019) 102–107.

[30] H. Gonome, M. Baneshi, J. Okajima, A. Komiya, S. Maruyama, Controlling the radiative properties of cool black-color coatings pigmented with CuO submicron particles, Journal of Quantitative Spectroscopy and Radiative Transfer 132 (2014) 90–98.

[31] Nederlands Normalisatie-instituut, NEN-EN-ISO 13468-2 Plastics - Determination of the total luminous transmittance of transparent materials - Part 2: Double-beam instrument (ISO 13468-2:2021,IDT) (2021).

[32] Labsphere, Integrating Sphere Radiometry and Photometry Technical Guide, PB-16010-000 Rev.00 (2017).

[33] J. Jonsson, G. Smith, C. Deller, A. Roos, Directional and angle-resolved optical scattering of high-performance translucent polymer sheets for energy-efficient lighting and skylights, Applied Optics 44 (2005) 2745–2753.

[34] S. Hemming, V. Mohammadkhani, J. Van Ruijven, Material technology of diffuse greenhouse covering materials - Influence on light transmission, light scattering and light spectrum, Acta Horticulturae 1037 (2014) 883–896.

[35] C. Gueymard, A simple model of the atmospheric radiative transfer of sunshine: algorithms and performance assessment, Florida Solar Energy Center (1995).

Appendix

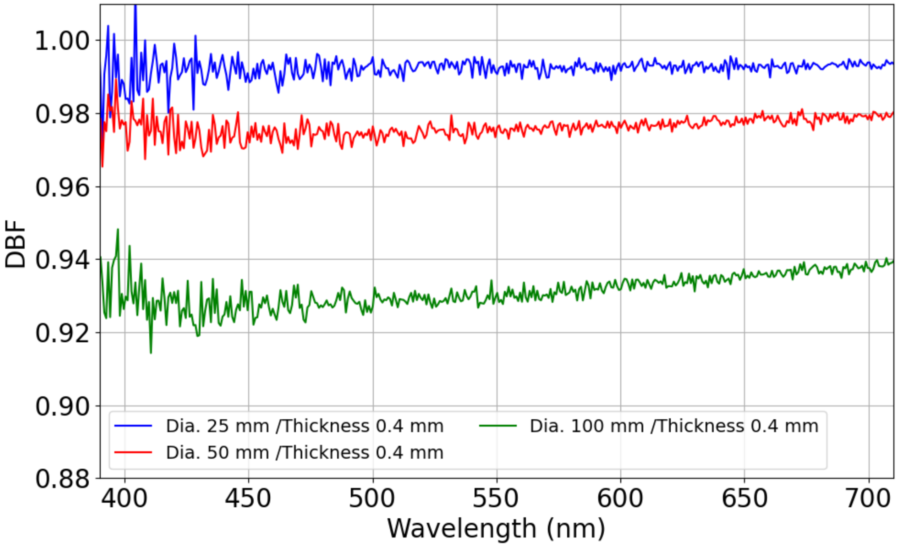

Figure 3.13: The double-beam coefficient of 25 mm, 50 mm and 100 mm ports across the wavelength from 400 nm to 700 nm.

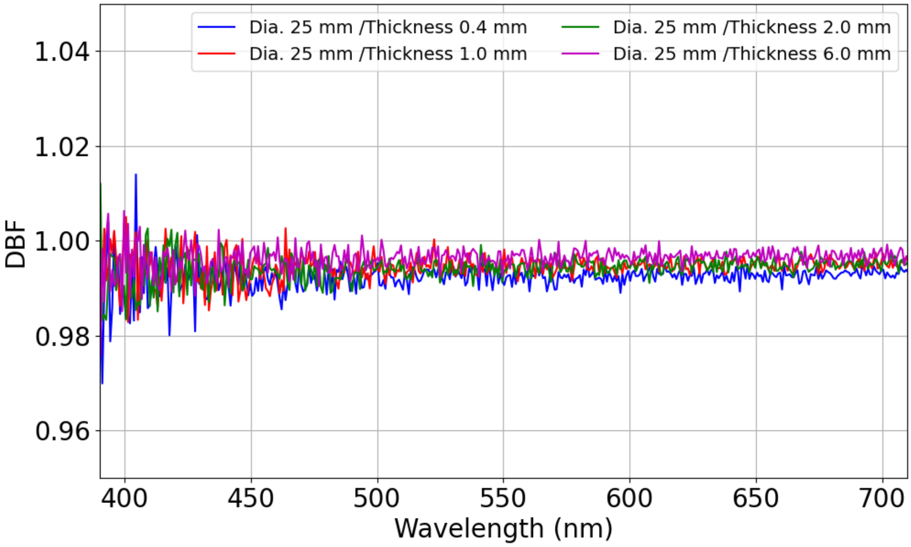

Figure 3.14: The double-beam coefficient of 25 mm ports with different edge thicknesses 0.4, 1, 2, and 6 mm across the wavelength of 400 nm to 700 nm.

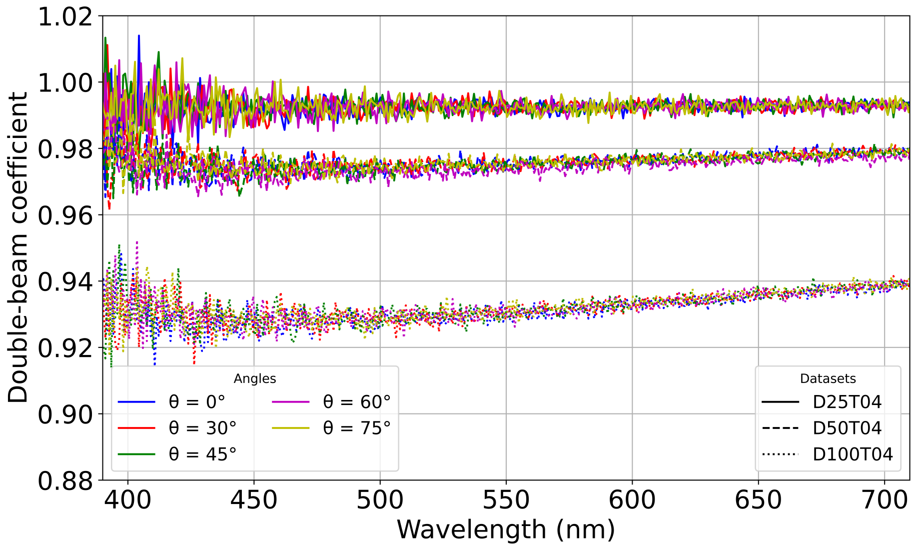

Figure 3.15: The double-beam coefficient 25, 50, 100 mm ports with different incident angles.

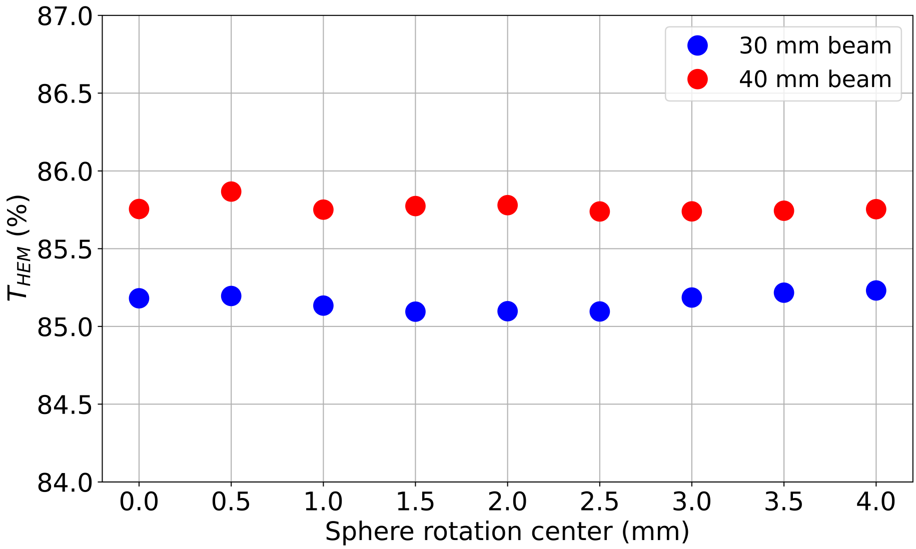

Figure 3.16: The $\mathrm{T_{HEM}}$ measured at the different positions of the sphere rotation center. The sphere rotation center was changed from the same plane as the sample port (0 mm) to the front side of the sample (4 mm).

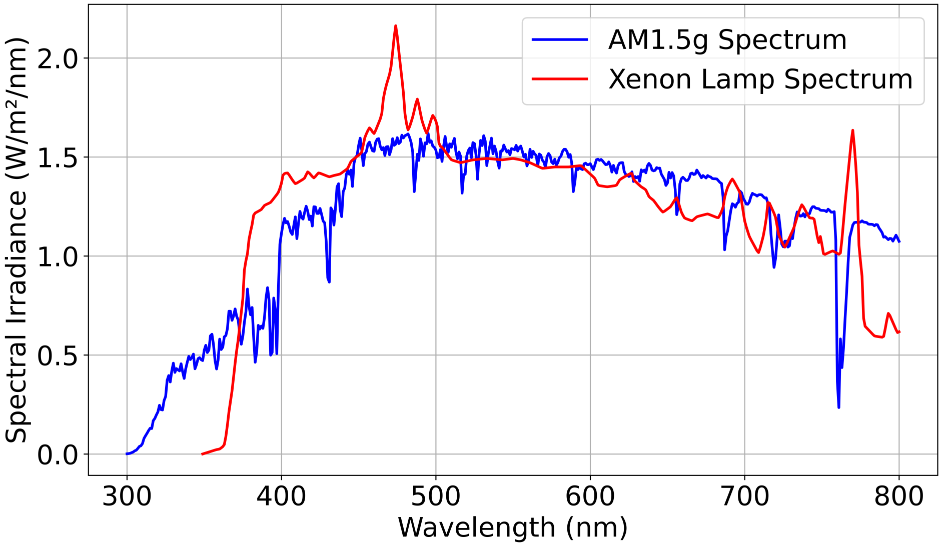

Figure 3.17: A comparison of spectral irradiance of AM1.5g and Xenon lamp. Both the raw data are acquired from the website “PV Lighthouse”, which are Aescusoft colsim single Xe lamp and AM1.5g [35], respectively.

4

Study of ZnS:Ag and $BaMgAl_{10}O_{17}:Eu^{2+}$ phosphor for UV-to-PAR spectral conversion greenhouse coatings

Spectral conversion films and coatings based on photoluminescent materials have attracted increasing attention for greenhouse applications and are reported to provide a net benefit through spectral control. However, there is little experimental data on spectral conversion coating that quantifies their optical properties, including absorption, transmittance, scattering, and the influence of the phosphor intrinsic parameters. In this work, UV-to-PAR spectral conversion coatings based on two commercial phosphors ZnS:Ag and $BaMgAl_{10}O_{17}:Eu^{2+}$ (BAM:Eu), with different particle loading and thickness, were fabricated and assessed by direct transmittance, hemispherical light transmittance (T_{HEM}), and diffuse reflectance. Transmittance decreased with increasing coating thickness and particle loading, whereas backward scattering showed the opposite trend. Performance indicators derived from direct transmittance revealed that host-absorption ZnS:Ag coatings exhibited greater UV absorption and higher PAR Enhancement than activator-absorption BAM:Eu coatings, resulting from their higher absorption coefficient. Quantum yield had a minimal impact because both phosphors displayed close PLQY values. However, the backward scattering of ZnS:Ag coatings was more pronounced than that of BAM:Eu coating due to the high refractive index of ZnS:Ag ($n \approx 2.3$), as confirmed by diffuse reflectance measurements. The 18 mass%, 200 µm ZnS:Ag coating showed the highest 1.3% PAR Enhancement, but its T_{HEM} was reduced by about 45%, demonstrating that backward scattering can counteract the benefits of spectral conversion. A general discussion for phosphor selection in greenhouse applications is also provided in this work.

4.1. Introduction

Food insecurity currently affects hundreds of millions of people worldwide [1,2]. Greenhouses are emerging as a critical solution offering reduced reliance on weather conditions and significantly higher crop yields per unit area compared to traditional open-field agriculture [3–5]. With the advancement of greenhouse technology, interest in innovative greenhouse roofs featuring functionalities such as scattering, anti-reflection, and spectrum shifting has grown rapidly over the past decade [6–16].

A growing number of research articles on spectral conversion greenhouse covers are published each year. Fan et al. provided a comprehensive overview of spectral conversion strategies (i.e., down-converting high-energy radiation to lower-energy radiation) and the phosphor materials suitable for each approach, and discussed the potential economic benefits of deploying luminescent conversion films for crop yield enhancement [17]. UV radiation constitutes 7 - 10% of the solar spectrum relative to photosynthetically active radiation (PAR, 400 - 700 nm), depending on air mass and weather conditions [18]. UV is often considered detrimental to crops because it can damage plant cells and is therefore typically absorbed or reflected by greenhouse roofs [19–21]. Following the generally accepted rule that "1% extra light can lead to 1% extra crop yield", greenhouse production can be increased if UV radiation is efficiently converted to PAR [22,23]. Shabalina et al. reviewed photoconversion cover (PCC) developments from 2020 to 2024 and summarized greenhouse test outcomes across 58 PCC studies [24]. Although greenhouse studies increasingly report yield gains from spectral conversion covers, quantitative characterization of the cover's optical properties and accompanying optical trade-offs, particularly PAR losses arising from reduced transmittance and enhanced backward scattering, remains limited [24,25].

In this work, we present the next stage in the development of "UV-to-PAR" solar spectral conversion phosphor coatings for greenhouse applications by fabricating commercially viable spray-on coatings with varying thicknesses and particle mass loadings, and systematically characterizing the coating's optical properties. Using three different integrating sphere setups, we measured photoluminescence, diffuse reflectance, perpendicular transmittance, and hemispherical light transmittance (T_{HEM}). From these measurements, we determined key optical properties relevant for greenhouse applications, including the photoluminescence quantum yield (PLQY), UV absorption, UV-to-PAR conversion efficiency, and PAR Enhancement. This study quantifies both the gains and losses associated with such coatings by examining a set of commercially available UV-absorbing, PAR-emitting phosphors, namely ZnS:Ag and $BaMgAl_{10}O_{17}:Eu^{2+}$. We investigate how coating performance correlates with intrinsic material properties such as quantum yield, refractive index, and absorption strength (by the doping ions or the host matrix). This work is intended as a practical reference for greenhouse stakeholders and materials developers. By presenting fundamental optical metrics, this study provides guidance for selecting appropriate phosphors for specific performance objectives.

4.2. Material and method

4.2.1. Coating preparation

Selected phosphor

One host-absorption phosphor ZnS:Ag and one activator-absorption phosphor $BaMgAl_{10}O_{17}:Eu^{2+}$ (BAM:Eu) were purchased from Phosphor Technology. The dopant content of Eu^{2+} is 0.35 mol%. The dopant content of Ag is too little to be detected by a scanning electron microscope, but the emission property and supplier confirms the existing of Ag dopant in the ZnS phosphor. The mean particle size, provided by the supplier, is 4.1 µm for BAM:Eu and 8 µm for ZnS:Ag. The density of the phosphor is 4.0 g/cm^3 for ZnS:Ag, and 3.7 g/cm^3 for BAM:Eu. The refractive index (n) is 1.7 for BAM:Eu, and 2.3 for ZnS:Ag. The theoretical absorption coefficient at 340 nm is approximately $10^4 \sim 10^5$ cm^{-1} for ZnS and $10^3 \sim 10^4$ cm^{-1} for 1 mol% Eu^{2+} in oxide host [26, 27]. The photoluminescence quantum yield (PLQY) of the two phosphors was characterized using a 340 nm LED and an integrating sphere. BAM:Eu and ZnS:Ag exhibited high PLQY values of 92% and 86%, respectively.

ZnS:Ag is used here primarily as a host-absorption benchmark because it combines strong UV absorption with a PLQY comparable to BAM:Eu, allowing a controlled comparison between host-absorption and activator-absorption phosphors. We note that ZnS host can darken under prolonged UV exposure due to photo-oxidation/defect formation. Stabilization strategies (e.g., surface passivation/coatings and dopant/defect engineering) are therefore essential for long-term deployment.

Luminescent coating's formulation

The luminescent coating consists of a dispersing agent, defoamer, acrylic resin, thickeners, and the selected phosphor. The loading of phosphors are 9 mass% and 18 mass%. The applied wet thickness of coating was 50, 100, 150, 200 µm on a 1 mm thick fused silica substrate by a bar-coater (TQC film applicator, Industrial Physics). A batch of coatings with the same wet thicknesses but without the addition of phosphor was produced following the same recipe, which are referred to as "no-phosphor coatings". All the results will be presented using the wet thickness values. The dry thickness measured by a profilometer (Dektak 8, Bruker), which are typically 4 times smaller than the wet thickness, is presented in the Appendix.

Because ZnS:Ag has a larger mean particle size than BAM:Eu, dispersion uniformity and mechanical-property impacts (e.g., flexibility and tensile strength) may differ in practical film processing. These particle–host compatibility aspects, including dispersion stability and mechanical testing, are outside the scope of the present optical benchmarking study and therefore not addressed in the work.

4.2.2. Characterization Methods

Photoluminescence and photoluminescence excitation measurement

The photoluminescence emission (PL) and excitation (PLE) spectra of the phosphors were recorded by a photomultiplier tube (R7600U-20, Hamamatsu) connected to a monochromator (SP2300, Princeton Instruments). A xenon lamp connected to another monochromator (Gemini 180, HORIBA) was used as an excitation light source. The photoluminescence spectrum of both phosphors were recorded under excitation of 340 nm light. The photoluminescence excitation spectrum was recorded by monitoring emission at 450 nm and corrected for the lamp spectrum intensity by a calibrated silicon diode

UV-to-PAR performance indicators

The UV-to-PAR performance indicators quantify the luminescent coating's capability of converting UV to additional PAR. These indicators include coating's absorption spectrum $A_{coating}(\lambda)$ (%), UV-to-PAR conversion efficiency $\eta_{coating}$ (%), and PAR Enhancement (%). $\eta_{coating}$ in short is the number of emitted PAR photons entering the greenhouse per absorbed UV photon. PAR Enhancement equals the ratio of luminescence-generated PAR photons entering the greenhouse to the total PAR photons in the AM1.5 solar spectrum. The detailed characterization methodology is described in our previous work [23]. $A_{coating}(\lambda)$ and $\eta_{coating}$ of the luminescent coating in the UV region were determined using a direct transmittance system with a deuterium lamp (AvaLight-DH-S, Avantes) as the light source. The transmitted light spectra of a fused-silica substrate ($I_{substrate}(\lambda)$) and the luminescent coating on the substrate ($I_{coating}(\lambda)$) were collected by a spectrometer (QE65Pro, Ocean Optics) connected with an optical fiber (FC-UVIR600, Avantes) to an integrating sphere located behind the sample. This detection system was calibrated with a calibrated deuterium light source (UV40, Optronic Laboratories) and tungsten light source (EV81, EPLAB). $A_{coating}(\lambda)$ and $\eta_{coating}$ are defined as follows:

$$A_{coating}(\lambda) = 1 - \frac{I_{\text{coating}}(\lambda)}{C_{\text{Ref}} * I_{\text{substrate}}(\lambda)} \tag{4.1}$$

$$\eta_{\text{coating}} = \frac{\int_{400}^{700} [I_{\text{coating}}(\lambda) - C_{\text{Ref}} * I_{\text{substrate}}(\lambda)] d\lambda}{\int_{250}^{400} [C_{\text{Ref}} * I_{\text{substrate}}(\lambda) - I_{\text{coating}}(\lambda)] d\lambda} \tag{4.2}$$

$I_{coating}(\lambda)$ and $I_{substrate}(\lambda)$ are the transmitted signals collected by an integrating sphere. In our measurement configuration, the following equation holds: 1=A+T+R+W, in which W equals the wave-guided fraction escaping through the sample edges. Although we measured the backward reflection R (through diffuse reflectance measurement) and transmission T, we cannot reliably measure W. Therefore, we have introduced a more practical and reliable metric C_{Ref} that takes into account the influence of both the backward scattering and waveguiding effects on the loss of incident PAR photon flux. C_{Ref} was determined within a near-infrared (NIR) spectral range, 700-750 nm, unaffected by both emission and absorption. By applying C_{Ref}, the influence of backward scattering and waveguiding effects (R+W) can be removed from the calculations of $A_{coating}(\lambda)$ and $\eta_{coating}$. An assumption of constant backward scattering and waveguiding effects between 250 to 900 nm was made.

The PAR Enhancement was subsequently calculated using $A_{coating}(\lambda)$ and $\eta_{coating}$ according to

$$\text{PAR enhancement} = \frac{\eta_{\text{coating}} * \int_{250}^{400} [A_{\text{coating}}(\lambda) * I_{\text{solar}}(\lambda)] d\lambda}{\int_{400}^{700} I_{\text{solar}}(\lambda) d\lambda} \tag{4.3}$$

in which the integration part on the right hand side of this equation eliminates the influence of the lamp spectrum as if the measurements was done with the solar spectrum. The AM1.5 solar spectrum, $I_{solar}(\lambda)$, expressed in number of photons, was derived from the ASTM G173-03 Reference Spectra [28].

Hemispherical light transmittance

The hemispherical light transmittance T_{HEM} of all the coated samples was measured by a tabletop characterization system developed in Chapter 3. The calculation of T_{HEM} considers the wavelength range from 400 nm to 700 nm (PAR). A detailed description of the measurement procedure and calculation can be found in the cited work. Note that the T_{HEM} system employs a tungsten lamp as the light source, which emits mainly within the PAR region. Consequently, the obtained T_{HEM} values reflect not only PAR transmittance but also account for the absorption of blue photons and emission of red photons. The T_{HEM} of 1 mm-thick fused silica substrate was measured to be 87.7%.

Diffuse reflectance

The diffuse reflectance of all samples was measured using an integrating sphere (IS2004, Thorlabs) and in combination with a deuterium light source (AvaLight-DH-S, Avantes). The integrating sphere was positioned directly above the coating sample to collect the backward scattered (reflected) light (R) signals from the incident deuterium illumination. A reference measurement was obtained using the same reflective material as the inner surface of the integrating sphere. The diffuse reflectance of all coatings was measured by taking the average value in the NIR wavelength range (700-750 nm), where no absorption and emission occurred. The diffuse reflectance of 1 mm-thick fused silica substrate was measured to be 8.0%.

4.3. Results and discussions

The final appearance of the coating samples is presented in Fig 4.1 and Fig. 4.2.

4.3.1. Photoluminescence excitation (PLE) and photoluminescence (PL) spectra

The photoluminescence excitation (PLE) and photoluminescence (PL) spectra of the selected phosphors are shown in Figure 4.3. The absorption and emission mechanism of BAM:Eu originates from the activator ions, Eu^{2+}, characterized by the electronic transition from the ground state $4f^7$ to the excited state $4f^65d^1$. The two excitation peaks at 250 nm and 310 nm arise from the crystal field splitting of the 5d configuration. A broad emission peak at 450 nm is a distinctive feature of Eu^{2+} luminescence [29, 30]. ZnS:Ag phosphor exhibited a sharp peak at 340 nm in the PLE spectrum corresponding to the band gap of ZnS (3.6 eV). The blue emission peak at 450 nm arises from electron-hole recombination after bandgap excitation from the valence band (VB) to the conduction band (CB), involving radiative relaxation via an intermediate energy level created by Ag^+ dopants located just above the VB of ZnS [31, 32].

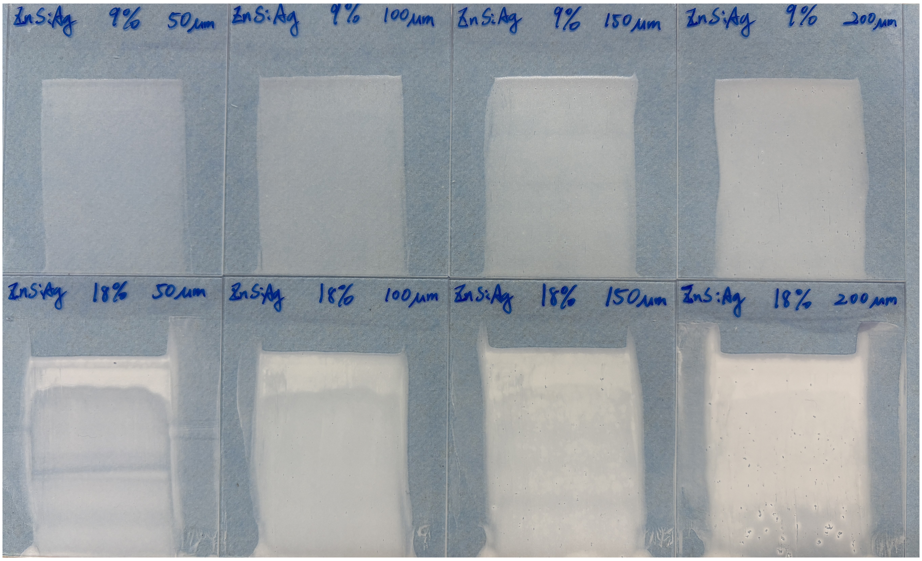

Figure 4.1: Final appearance of ZnS:Ag coatings.

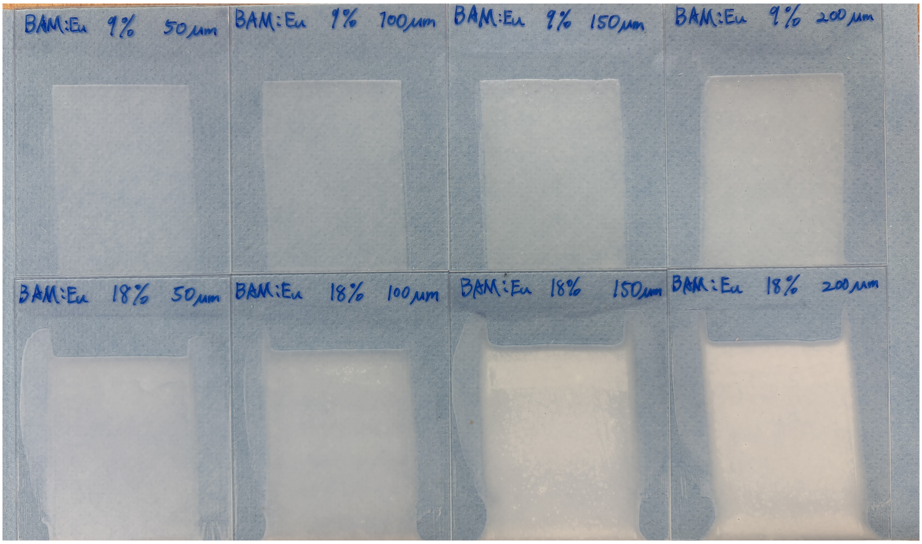

Figure 4.2: Final appearance of BAM:Eu coatings.

4.3.2. UV-to-PAR performance indicators

PAR Enhancement quantifies how much extra PAR light in the form of luminescence is entering the greenhouse due to UV absorption. Its efficiency is therefore a crucial quantity for UV-to-PAR type spectral conversion greenhouse coating. As explained in the

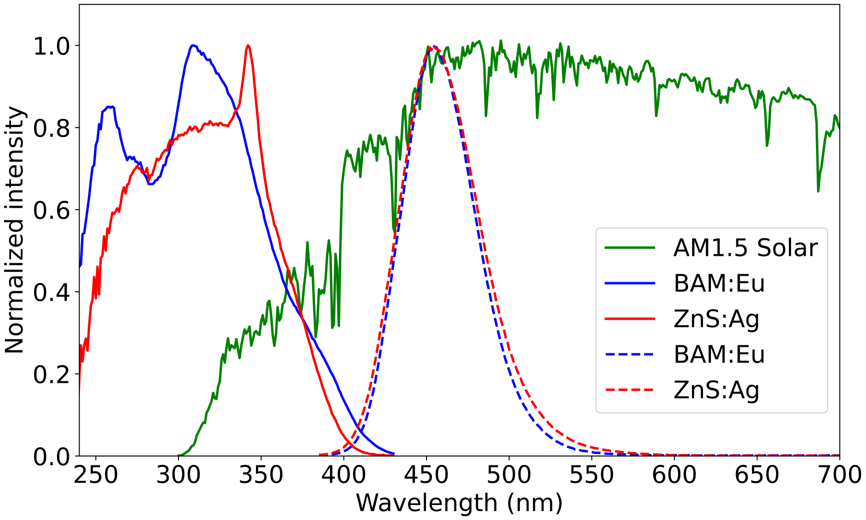

Figure 4.3: Normalized photoluminescence excitation (solid lines) and photoluminescence (dashed lines) spectra with AM1.5 solar spectrum.

methodology section, PAR Enhancement is derived from the coating's correction factor C_{Ref}, absorption spectrum $A_{\mathrm{coating}}(\lambda)$, and UV-to-PAR conversion efficiency η_{coating} of the coating. The influence of these quantities on PAR Enhancement is discussed in the following section.

Figure 4.4 shows the transmittance spectra of all luminescent coatings ($I_{\mathrm{coating}}(\lambda)$) relative to that of the fused silica substrate ($I_{\mathrm{substrate}}(\lambda)$) derived from the original transmitted light signals (provided in the Appendix). Three wavelength intervals are discussed below: the UV range (250-400 nm), where absorption occurred; the PAR range (400-700 nm), where photoluminescence was observed; and the NIR range (700-750 nm), where neither absorption nor photoluminescence took place.

The transmittance values in the 250-400 nm range were generally below unity due to waveguiding, backward scattering, and UV absorption. This range of data was converted into the coating's absorption spectrum $A_{\mathrm{coating}}(\lambda)$ in Fig. 4.6 and discussed later. In the 400-700 nm range of the transmittance spectra, a pronounced emission from the luminescent coatings was clearly observed. A transmittance value exceeding unity indicates that additional photosynthetically active radiation (PAR) enters the greenhouse as a result of luminescence generated through UV-to-PAR conversion. This effect was particularly prominent because the deuterium lamp emitted a disproportionately high amount of UV radiation relative to the AM1.5 solar spectrum. To correct for this, the AM1.5 solar spectrum was applied in the PAR Enhancement calculation, effectively removing the influence of the lamp features as explained by $I_{\mathrm{solar}}(\lambda)$ in Eq. 4.3. The use of a deuterium lamp improves the accuracy of UV absorption measurements and PAR Enhancement, while our calculation method conveniently allows the use of any lamp type. The dips at 650 and 660 nm resulted from intense lamp spectral peaks that are difficult to correct for.

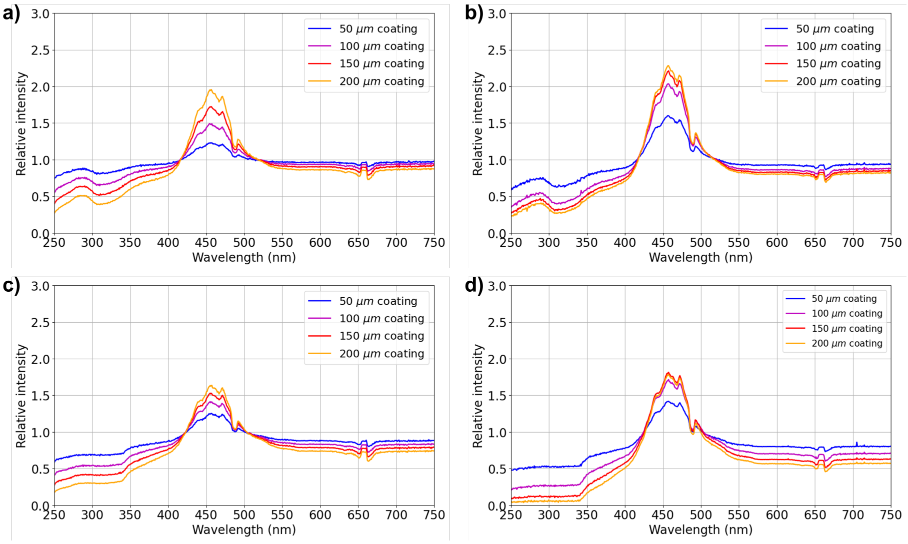

Figure 4.4: The transmittance spectrum of all samples, relative to the substrate, measured using an integrating sphere. a) BAM:Eu 9 mass% with various coating thickness. b) BAM:Eu 18 mass% with various coating thickness. c) ZnS:Ag 9 mass% with various coating thickness. d) ZnS:Ag 18 mass% with various coating thickness.

In the NIR range, transmittance was governed by backward scattering and waveguiding effects, with no contribution from either emission or absorption, as discussed before. The C_{Ref} value was determined by averaging the transmittance of the sample relative to the substrate over this spectral region.

Figure 4.5 presents the C_{Ref} values of all samples. A small C_{Ref} value indicates substantial backward scattering and waveguiding effects in the coating. Both backward scattering and waveguiding effects lead to a general reduction in the incident photon flux of PAR entering a greenhouse. Moreover, a small C_{Ref} value may indirectly reduce PAR Enhancement because fewer incident UV photons remain available for absorption and conversion due to the backward scattering and waveguiding effects.

Both increased coating thickness and higher particle loading result in a smaller C_{Ref}, demonstrating enhanced scattering and waveguiding effects. ZnS:Ag coatings showed a smaller C_{Ref} compared to the oxide-based phosphor BAM:Eu, indicating that backward scattering and waveguiding effect were more pronounced in ZnS:Ag coatings. This difference is primarily attributed to the refractive index contrast between the phosphor particles and the surrounding medium: ZnS has a higher refractive index ($n \approx 2.3$) than BAM:Eu ($n \approx 1.7$), which increases reflection at particle–polymer interfaces and thereby strengthens scattering. In a simplified picture, the Fresnel relations predict higher interfacial reflectance for larger refractive-index mismatch, leading to more frequent changes in photon propagation direction and a higher probability of photons being redirected backward or guided laterally within the coating. The influence of refractive index is

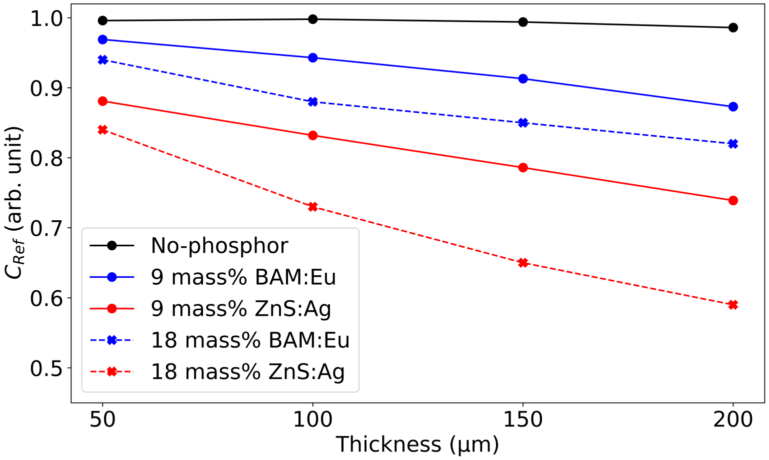

Figure 4.5: C_{Ref} of all coating samples

further discussed together with T_{HEM} in Section 4.3.3. All no-phosphor reference coatings showed C_{Ref} values between 0.99 and 1.00, consistent with their high optical transparency in the absence of scattering particles.

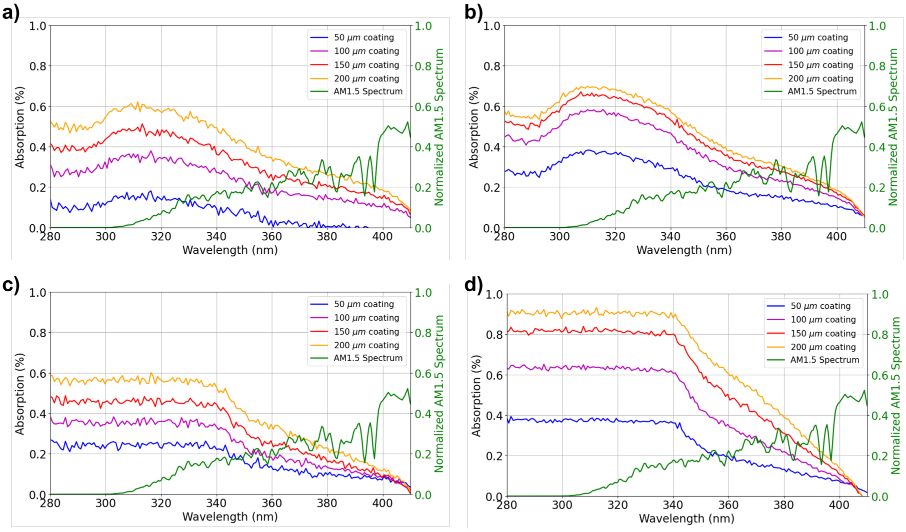

Figure 4.6: The absorption spectrum of all samples, derived from the transmitted light signals in Figure 4.4. The green curve is the normalized AM1.5 solar spectrum. a) BAM:Eu 9 mass% coatings with various thickness. b) BAM:Eu 18 mass% coatings with various thickness. c) ZnS:Ag 9 mass% coatings with various thicknesses. d) ZnS:Ag 18 mass% coatings with various thicknesses.

Figure 4.6 shows the absorption spectra of all coatings derived from Eq. 4.1. ZnS:Ag coatings exhibited a step like absorption edge near 340 nm, whereas BAM:Eu displayed an absorption band around 310 nm. These features are consistent with the corresponding PLE spectra of the phosphors in Fig. 4.3. The coating's absorption strength increased as both the particle loading and coating thickness increased.

Across all coating formulations, ZnS:Ag exhibited only a slightly higher absorption strength than BAM:Eu. Despite ZnS:Ag having a substantially higher absorption coefficient ($10^4 \sim 10^5$ cm^{-1}) due to the CB→VB transitions, up to two orders of magnitude higher than Eu^{2+} 4f→5d transitions in BAM ($10^3 \sim 10^4$ cm^{-1}), the measured absorption of ZnS:Ag coatings was only slightly higher than that of BAM:Eu coatings. The most plausible explanation lies in the diameter of the used phosphor particles. Although BAM:Eu has a lower intrinsic absorption coefficient, its particle size of 4 µm provides a sufficiently long optical path allowing UV photons to be absorbed, leading to a high absorption %.

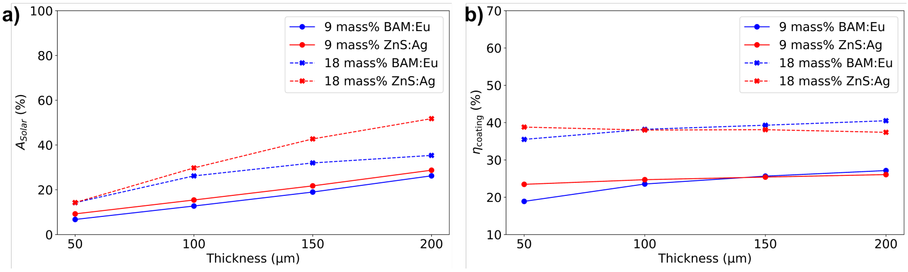

Figure 4.7: a) The absorption of total UV photon, $A_{solar}(\%)$, within 280-400 nm range in AM1.5 solar spectrum of all coating samples. b) UV-to-PAR conversion efficiency $\eta_{coating}$ of all coating samples.

In Eq. 4.3, the absorption spectrum $A_{coating}(\lambda)$ of each luminescent coating is applied to the AM1.5 solar spectrum $I_{solar}(\lambda)$ to calculate the total number of solar UV photons absorbed within the 280-400 nm range which is the more relevant absorption quantity when considering greenhouse applications. To demonstrate how much UV light was absorbed by each coating, the ratio of absorbed UV photons to the total incident UV photons in the AM1.5 spectrum, $A_{coating}(\lambda)$, was calculated according to Eq. 4.4 below and shown in Fig. 4.7a.

$$A_{\text{solar}}\,(\%) = \frac{\displaystyle\int_{250}^{400} [A_{\text{coating}}(\lambda) * I_{\text{solar}}(\lambda)]\,\mathrm{d}\lambda}{\displaystyle\int_{250}^{400} I_{\text{solar}}(\lambda)\,\mathrm{d}\lambda} \tag{4.4}$$

In general, ZnS:Ag coatings absorbed more solar UV photons than BAM:Eu coatings at the same particle mass loading. The absorption strength clearly influenced the amount of absorbed UV photons. In addition, the shape of the absorption spectrum also played a role in the amount of total absorbed UV photons. The absorption spectrum of BAM:Eu coatings showed a peak at 310 nm and then decreased toward longer wavelengths, while

ZnS:Ag coatings showed a step-like feature until 340 nm and gradually decreased toward longer wavelengths. Since the UV photon flux in the AM1.5 solar spectrum is not uniform, as illustrated in Fig. 4.6, this spectral feature also contributed to the higher solar UV absorption in ZnS:Ag coatings compared to BAM:Eu coatings. Therefore, coatings that maintain a high absorption across the entire solar UV range or exhibit stronger absorption at longer UV wavelengths (close to 400 nm) are more effective at capturing available UV photons, ultimately resulting in greater total UV absorption and enhancing PAR generation.

The number of luminescence-generated PAR photons entering the greenhouse per absorbed UV photon, denoted as η_{coating}, depends primarily on the photoluminescence quantum yield (PLQY), which is an intrinsic property of each phosphor and does not vary with particle loading or coating thickness. Under the assumption of isotropic emission, only 50% of the emitted photons are directed toward the interior of the greenhouse, while the remaining 50% escape outward, leaving the greenhouse. Under these idealized conditions, η_{coating} should not exceed half the PLQY, which results in 46% for BAM:Eu coatings and 43% for ZnS:Ag coatings.

As shown in Fig. 4.7b, η_{coating} exhibits only a weak dependence on coating thickness, particularly for ZnS:Ag coatings, but increases markedly with particle loading. In the 9 mass% series, both phosphors showed similar η_{coating} values in the range of 20-25%. However, in the 18 mass% series, both BAM:Eu and ZnS:Ag coatings approached the theoretical limit of η_{coating} at 200 µm, reaching 40% for BAM:Eu and 37% for ZnS:Ag. The increase in η_{coating} observed at a higher particle mass loading may be partly attributed to the configuration of the measurement setup. When the coating sample covers the port of the integrating sphere, photons that have entered the sphere after transmitting through the coating are retained within the sphere due to back-reflection at the coating, thereby enhancing the detected signal. Coatings that exhibit stronger backward scattering can further increase this internal retention, which is consistent with the trend in C_{Ref} values observed in Fig. 4.5.

It should be noted that this “photon retention” contribution is specific to the integrating-sphere configuration and may lead to a modest overestimation of η_{coating} for highly scattering coatings, because a fraction of photons that would otherwise escape the detection geometry can be redirected into the sphere and collected. In practical greenhouse operation, the space beneath the coating is not an ideal reflective cavity; consequently, backward scattering at the coating is expected to primarily reduce the net transmitted PAR flux rather than enhance photon collection. Therefore, η_{coating} is interpreted here mainly as an intrinsic conversion metric, whereas application-relevant performance must be assessed by jointly considering η_{coating} with other performance indicators.

Although η_{coating} was primarily determined by the PLQY of the phosphors used, the result indicated it can be influenced by formulation parameters such as particle loading and thickness. Since a higher η_{coating} directly contributes to greater PAR Enhancement, optimizing η_{coating} is essential for maximizing the overall performance of the coating.

Finally the PAR Enhancement values are presented in Fig. 4.9. PAR Enhancement increased with both coating thickness and particle loading. At 9 mass% loading, ZnS:Ag coatings exhibited only slightly higher PAR Enhancement than BAM:Eu. Both ZnS:Ag

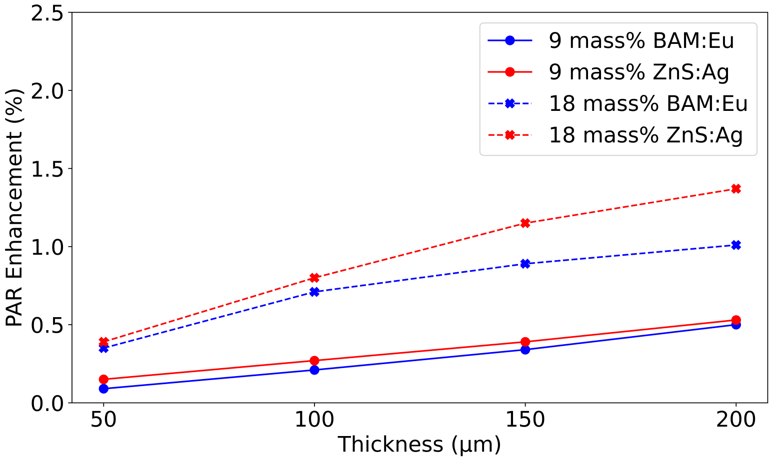

Figure 4.8: PAR Enhancement of all coating samples.

and BAM:Eu coatings reached 0.5% PAR Enhancement at 200 µm thickness. At 18 mass% loading, ZnS:Ag coatings again showed a larger PAR Enhancement than the BAM:Eu coatings. Both phosphors achieved the highest PAR Enhancement values at 200 µm, which was 1.0% for BAM:Eu and 1.3% for ZnS:Ag.

Despite the strong backward scattering effect for ZnS:Ag coatings, as indicated by C_{Ref}, and its slightly lower PLQY, the PAR Enhancement was higher due to its higher UV absorption as shown in Fig. 4.7a. These results demonstrate that both $\eta_{coating}$ and the total UV absorption are primary factors controlling PAR Enhancement. The UV absorption can be tuned by adjusting coating thickness and particle loading, while $\eta_{coating}$ is influenced primarily by the particle mass loading.

4.3.3. Hemispherical light transmittance T_{HEM} and diffuse reflection

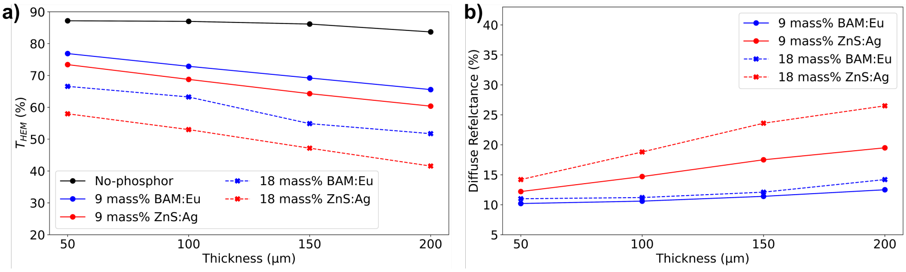

Figure 4.9: a) Hemispherical light transmittance (T_{HEM}) of all coating samples. b) Diffuse reflectance of all coating samples.

The T_{HEM} of luminescent coatings with 9 mass% and 18 mass% particle loading is presented in Fig. 4.9a. For all luminescent coating series, including the no-phosphor series,

T_{HEM} decreased with increasing thickness and particle loading. The attenuation of the light signal is a combined effect of the backward scattering and waveguiding in the polymer matrix and substrate. Needless to say, PAR enhancement values by luminescence presented in Fig. 4.8 are far smaller than the losses by backward scattering evidenced by the T_{HEM} values presented in Fig. 4.9a.

BAM:Eu coatings showed higher T_{HEM} values than ZnS:Ag coatings at the same thickness and loading, meaning more PAR light penetrating through the coating into the greenhouse. This difference can be explained by the refractive index of the phosphors. BAM:Eu, an oxide material, has a lower refractive index ($n \approx 1.7$), while ZnS:Ag, a sulphide material, has a higher value ($n \approx 2.3$). As discussed when presenting C_{Ref} values, a larger refractive index results in a greater reflectance.

To verify that the optical losses were primarily caused by backward scattering, diffuse reflectance measurements were performed on the coatings and presented in Fig. 4.9b. Unlike C_{Ref}, which accounts for light loss from both backward scattering and waveguiding effects, diffuse reflectance captures only the backward scattered light from the sample. As shown, diffuse reflectance increased with both coating thickness and particle loading. The generally higher reflectance observed in ZnS:Ag coatings compared to BAM:Eu coatings supports the conclusion that the refractive index of the phosphor plays a significant role in hemispherical light transmittance. Overall, the results demonstrated that particle loading, coating thickness, and refractive index all influence losses by scattering and consequently affect the hemispherical light transmittance of the coating.

4.3.4. General discussion

Incorporating 8 µm ZnS:Ag phosphor into a 200 µm-thick coating at a particle loading of 18 mass% increases the PAR level by 1.3%. The theoretical limit of 3.5% could be approached by engineering the coating formulation, for example, by increasing the coating thickness and/or phosphor loading. It should be noted that such modifications would likely increase cost, complicate practical implementation, and further reduce PAR transmittance.

The concept of spectral conversion in the greenhouse environment is intuitively beneficial for enhancing plant growth and increasing crop yield, but the potential gain from PAR-emitting coating is counteracted by light losses due to backward scattering at the coating. In our coating, such losses lowered the hemispherical light transmittance by as much as 45%. It is important to note that phosphors with a higher refractive index, such as ZnS ($n \approx 2.3$), exhibited a larger scattering efficiency, lowering T_{HEM} to a larger extent than BAM:Eu ($n \approx 1.7$). Consequently, phosphors with similar or even higher refractive index that have been suggested for spectral conversion purposes such as (oxy)sulphides and (oxy)nitrides, including Ca(Sr)ZnOS:Eu^{2+}, (Ca,Sr)S:Eu^{2+}, and Ba_2ZnS_3:Eu^{2+}, are less suitable.

Reducing particles' backward scattering efficiency is therefore indispensable and could be achieved by employing larger particles that favour forward scattering as predicted by Mie theory, or particles with a radius much smaller than the wavelength of light [33]. Although this approach is conceptually sound, reducing scattering by changing radius also reduces absorption, which necessitates a higher particle density or coating thickness, both of which can reintroduce scattering losses. The true scientific challenge is to significantly reduce scattering strength without affecting or preferably even increasing absorption strength. Despite the fact that scattering significantly decreases PAR transmittance, scattering by itself, formally quantified as "hortiscatter," can also promote plant growth because it generates a more even light distribution on leaves [6,7]. Future research should explicitly evaluate the combined effects of hortiscatter and hemispherical light transmittance, including PAR Enhancement, on crop yield improvement.

Phosphors selected for greenhouse applications should exhibit a high PLQY, a low refractive index to minimize scattering losses, and sufficient chemical stability under operating conditions. Accordingly, a practical spectral-conversion greenhouse coating should combine low backward scattering with high PAR transmittance, strong UV absorption, and high UV-to-PAR conversion efficiency, thereby increasing the PAR photon supply in the greenhouse without reducing the baseline transmitted PAR from sunlight.

4.4. Conclusion

A series of luminescent coatings based on two commercial UV-absorbing, PAR-emitting phosphors (ZnS:Ag and $BaMgAl_{10}O_{17}:Eu^{2+}$) was fabricated to assess their suitability for greenhouse spectral conversion. Key optical performance metrics, including UV absorption and UV-to-PAR conversion efficiency, hemispherical light transmittance (T_{HEM}), and diffuse reflectance, were systematically quantified as a function of coating thickness and phosphor loading.

The results show that particle based spectral conversion coatings can provide measurable PAR enhancement inside the greenhouse, reaching up to 1.3% for a 200 µm coating containing 18 mass% ZnS:Ag. However, pronounced backward scattering, consistent with the high refractive index of ZnS, substantially reduced T_{HEM} and thus the total transmitted PAR photon flux, demonstrating that scattering losses can counteract the benefits of spectral conversion. By comparison, the activator-absorption phosphor $BaMgAl_{10}O_{17}:Eu^{2+}$ achieved a slightly lower PAR enhancement (1.0%) while exhibiting a smaller reduction in hemispherical transmittance, attributable to its lower refractive index and correspondingly weaker backward scattering.

Overall, this work provides an experimental quantification of both the optical gains (PAR enhancement) and losses (transmittance reduction and backward scattering) associated with UV-to-PAR luminescent greenhouse coatings. The presented measurement workflow and performance indicators offer a practical framework for future studies to assess spectral conversion coatings under application-relevant conditions and to guide phosphor/coating design toward simultaneously high UV absorption and conversion efficiency with minimal scattering-induced PAR losses.

References

[1] Food Security Information Network, FSIN and Global Network Against Food Crises, Tech. rep. (2024).

[2] I. Miron, C. Linares, J. Dıaz, The influence of climate change on food production and food safety, Environmental Research 216 (2023) 1–6.

[3] U. Mc Carthy, I. Uysal, R. Badia-Melis, S. Mercier, C. O'Donnell, A. Ktenioudaki, Corrigendum to 'Global food security – Issues, challenges and technological solutions, Trends in Food Science and Technology 123 (2022) 404.

[4] D. Zhou, H. Meinke, M. Wilson, L. Marcelis, E. Heuvelink, Towards delivering on the sustainable development goals in greenhouse production systems, Resources, Conservation and Recycling 169 (2021).

[5] P. Zabel, M. Bamsey, D. Schubert, M. Tajmar, Review and analysis of over 40 years of space plant growth systems, Life Sciences in Space Research 10 (2016) 1–16.

[6] N. Victoria, E. Romero, B. van Breugel, C. Stanghellini, S. Hemming, Can extreme light diffusion still increase crop growth in greenhouses?, Acta Horticulturae 1423 (2025) 79–86.

[7] G. van Steekelenburg, S. Hemming, E. Kaiser, E. Heuvelink, Quantifying the effects of hortiscatter in greenhouse cover materials on crop yield, Acta Horticulturae 1423 (2025) 87–94.

[8] M. Teitel, H. Vitoshkin, F. Geoola, S. Karlsson, N. Stahl, Greenhouse and screenhouse cover materials: Literature review and industry perspective, Acta Horticulturae 1227 (2018) 31–44.

[9] R. Giacomelli, Gene A., Greenhouse covering systems, HortTechnology (1993).

[10] C. Maraveas, Environmental sustainability of greenhouse covering materials, Sustainability 11 (2019).

[11] K. Mishra, C. Stanghellini, S. Hemming, Technology and materials for passive manipulation of the solar spectrum in greenhouses, Advanced sustainable systems 7 (2023).

[12] H. Aldaftari, J. Okajima, A. Komiya, S. Maruyama, Radiative control through greenhouse covering materials using pigmented coatings, Journal of Quantitative Spectroscopy and Radiative Transfer 231 (2019) 29–36.

[13] T. Li, Y. Gao, K. Zheng, Y. Ma, D. Ding, H. Zhang, Achieving better greenhouse effect than glass: Visibly transparent and low emissivity metal-polymer hybrid metamaterials, ES Energy and Environment 5 (2019) 102–107.

[14] S. Hemming, T. Dueck, J. Janse, F. Van Noort, The effect of diffuse light on crops, Acta Horticulturae 801 (2008) 1293–1300.

[15] F. Kempkes, C. Stanghellini, N. Victoria, M. Bruins, Effect of diffuse glass on climate and plant environment: First results from an experiment on roses, Acta Horticulturae 952 (2012) 255–262.

[16] R. Yalcin, H. Erturk, Improving photosynthetic efficiency using greenhouse coatings with scattering and fluorescent pigments, Materials Research Express 6 (2019).

[17] Y. Fan, Y. Zhou, Z. Qiu, S. Lian, Photoluminescent materials for solar spectral conversion greenhouse films, Journal of Materials Chemistry C, 2025, **13**, 5462–5482.

[18] S. Hemming, D. Waaijenberg, G. Bot, P. Sonneveld, F. de Zwart, T. Dueck, C. van Dijk, A. Dieleman, N. Marissen, E. van Rijssel, B. Houter, Optimaal gebruik van natuurlijk licht in de glastuinbouw, Agrotechnology & Food Innovations, 2004, **100**, 154.

[19] F. Hollósy, Effects of ultraviolet radiation on plant cells, Micron, 2002, **33**, 179–197. doi:10.1016/S0968-4328(01)00011-7.

[20] E. Kovács, Keresztes, Effect of gamma and UV-B/C radiation on plant cells, Micron, 2002, **33**, 199–210. doi:10.1016/S0968-4328(01)00012-9.

[21] G. Nawkar, P. Maibam, J. Park, V. Sahi, S. Lee, C. Kang, UV-induced cell death in plants, International Journal of Molecular Sciences, 2013, **14**, 1608–1628. doi:10.3390/ijms14011608.

[22] S. Jakka, M. Silva, M. Soares, K. Pavani, Exploring the potential of Eu^{3+} and Mn^{4+}activated $LaAlO_3$ phosphors as red and far-red emitters for horticulture lighting, RSC Advances, 2023, **13**, 31314–31320. doi:10.1039/d3ra03241h.

[23] C. Cho, G. Bosco, E. van der Kolk, The potential of SiO_2:Al^{3+},Eu^{2+} blue phosphor coatings in greenhouse application, 2024, **157**, 2–8.

[24] A. Shabalina, V. Kozlov, M. Paskhin, I. Popov, S. Gudkov, A Mini-Review of Photoconversion Covers for Greenhouses: Assessment Parameters and Plant Experiment Results, Horticulturae, 2025, **11**, 680. doi:10.3390/horticulturae11060680.

[25] M. Ge, Y. Yuan, S. Liu, J. Li, C. Yang, B. Du, Q. Pang, S. Li, Z. Chen, Enhancing plant photosynthesis with dual light conversion films incorporating biomass-derived carbon dots, Carbon Capture Science and Technology, 2024, **13**. doi:10.1016/j.ccst.2024.100253.

[26] S. Adachi, S. Ozaki, Optical constants of cubic ZnS, Japanese Journal of Applied Physics 32 (1993) 5008–5013.

[27] A. Rocha, L. Andrade, S. Lima, A. Farias, A. Bento, M. Baesso, Y. Guyot, G. Boulon, Tunable color temperature of Ce^{3+}/$Eu^{2+,3+}$ co-doped low silica aluminosilicate glasses for white lighting, Optics Express 20 (2012) 10034–10041.

[28] C. Gueymard, D. Myers, K. Emery, Proposed reference irradiance spectra for solar energy systems testing, Solar Energy 73 (2002) 443–467.

[29] J. Zhang, Z. Zhang, Z. Tang, Y. Tao, X. Long, Luminescent Properties of the $BaMgAl_{10}O_{17}$:Eu^{2+}, M^{3+}(M = Nd, Er) Phosphor in the VUV Region, Chemistry of materials 14 (2002) 3005–3008.

[30] V. Singh, R. Chakradhar, J. Rao, H. Kwak, Photoluminescence and EPR studies of $BaMgAl_{10}O_{17}$:Eu^{2+} phosphor with blue-emission synthesized by the solution combustion method, Journal of Luminescence 131 (2011) 1714–1718.

[31] Y. Uehara, Electronic structure of luminescence center of ZnS:Ag phosphors, The Journal of Chemical Physics 62 (1974) 2982–2994.

[32] G. Blasse, b. Grabmaier, Luminescent Materials, Springer Berlin, Heidelberg, 1994.

[33] J. Meyer-Arendt, Introduction to classical and modern optics, Prentice-Hall, 1984.

Appendix

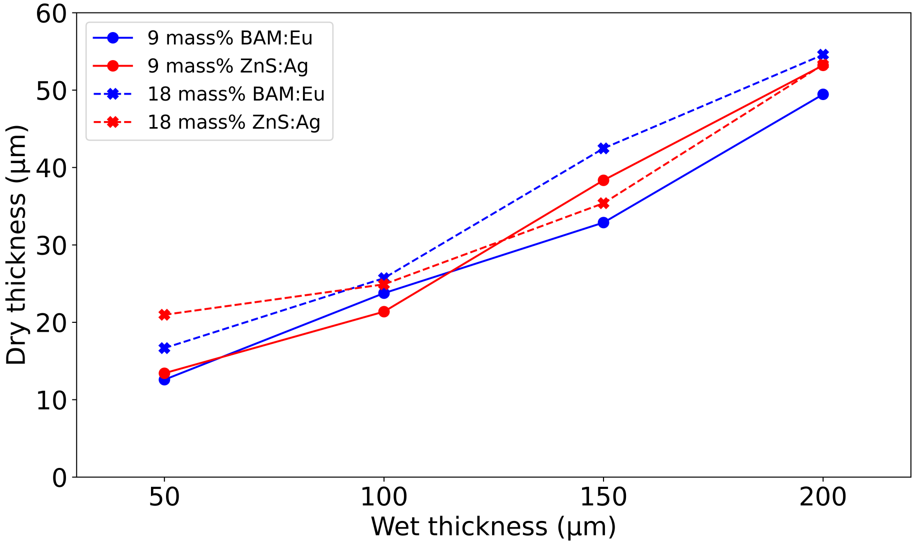

Figure 4.10: The dry thickness of the coating versus wet application thickness.

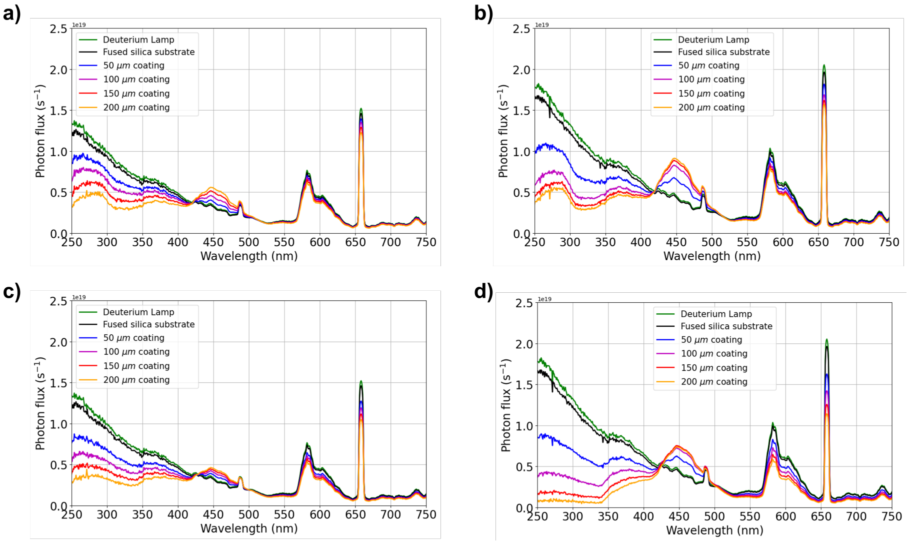

Figure 4.11: The transmittance light signals of all samples. a) BAM:Eu 9 mass% with various coating thickness. b) BAM:Eu 18 mass% with various coating thickness. c) ZnS:Ag 9 mass% with various coating thickness. d) ZnS:Ag 18 mass% with various coating thickness.

5

Investigating solar spectrum-shifting greenhouse roofing for enhancing crop performance

Previous studies have investigated phosphor-based luminescent coatings to convert UV radiation into extra photosynthetically active radiation (PAR), such as UV-to-red and UV-to-blue. However, the enhancement of PAR is limited by the small fraction of UV in the AM1.5 solar spectrum. In this study, we address this challenge by employing a high quantum efficiency phosphor, $Sr_2Si_5N_8:Eu^{2+}$, which converts both UV and blue light to the red part of the solar spectrum, in a luminescent coating that can be applied on a greenhouse roof. Four coatings (50-200 µm thick) with the same phosphor loading were fabricated. The hemispherical light transmittance of the coatings was measured using a customized tabletop system. Additionally, building upon the UV-to-PAR enhancement method proposed in Chapter Two, a new approach was established to quantify UV/blue-to-red conversion. The blue:red (B:R) light ratios under natural solar illumination were also examined. Results showed that while hemispherical light transmittance decreased with increasing coating thickness due to back scattering, the thicker coatings provided stronger red light emission. This trade-off indicates an opportunity for optimization - selecting a coating thickness that enhances red light without sacrificing overall transmittance. Notably, the B:R ratio can be altered from 1:1 to 1:5 by coating's thickness, and the absolute red photon flux is kept at 87% of the incident sunlight, which illustrates the potential of this luminescent coating to substantially enrich the red portion of the light spectrum through altering coating thickness. Such improved spectral management can be advantageous for certain crops, that respond favourably to higher red-light levels. Overall, this research highlights the potential of phosphor-based luminescent coatings to achieve a spectrum shift in greenhouse roofs, potentially optimizing plant growth conditions and enhancing crop yields.

The content of this chapter is published on the International Conference GreenSys2025.

5.1. Introduction

The principle of “1% extra light leads to 1% extra crop yield” has been widely accepted in horticulture [1]. Greenhouse operators commonly apply artificial lighting, such as high-pressure sodium lamps and LEDs, to increase the photon flux projected on plant leaves and to actively manipulate the light spectrum, thus maximizing crop yield [4–6]. Although this active modification allows for precise light management, it requires extra energy and raises overall production costs.

A passive approach modifying light involves applying photoluminescent materials, which convert high-energy radiation into low-energy radiation, potentially reducing energy demand while still improving light quality for crops [2,3,7]. Luminescent light conversion films are considered a direct and efficient approach to tailor the spectral quality of light reaching crops, and are manufactured by dispersing luminophores in polymer matrices [8]. Mao et al. produced polyethylene (PE) and polyvinyl alcohol (PVA) films containing $Ca_{0.5}Sr_{0.5}S$:Cu,Eu phosphor, which exhibits a strong red emission under ultraviolet (UV, 250-400 nm) excitation [24]. Zhu et al. synthesized Bi^{3+} and B^{3+} co-doped $CaAl_{12}O_{19}$:Mn phosphor and fabricated a photoluminescent film that is capable of converting UV light to red light [10]. Yang et al. reported a Eu^{2+}-based conversion film designed to shift UV light to blue light [11].

Luminescent materials can also be applied as a coating on greenhouse glazing to provide a semi-permanent spectral conversion function. In chapter 2, we have developed a UV-to-blue luminescent coating based on SiAlO:Eu^{2+} phosphor. A method that quantifies the performance in converting UV radiation to photosynthetically active radiation (PAR, 400-700 nm) was also introduced. The results demonstrated the feasibility of SiAlO:Eu^{2+} luminescent coating to enhance PAR by converting UV radiation. However, assuming a luminescent coating could convert all UV photons in the AM1.5g solar spectrum to PAR photons with a 50% emission entering the greenhouse, a theoretical maximum of only 3.5% PAR enhancement could be achieved [12]. This rough calculation indicates that the limited fraction of UV in the solar spectrum fundamentally constrains how much additional PAR can be generated.

While all PAR wavelengths help growth, photosynthetic pigments absorb them differently. Crops can benefit from a higher red-to-blue photon ratio, and such an optimal value varies by species and growth phase. The commercial phosphor, $Sr_2Si_5N_8$:Eu^{2+}, is particularly suitable for this requirement, as it offers a high quantum yield with strong absorption from 250 nm up to 550 nm and emission in the 550–750 nm range, matching perfectly with crops requiring a high red light environment [13–18].

In this study, we fabricate luminescent coatings incorporating $Sr_2Si_5N_8$:Eu^{2+} phosphor at 50, 100, 150, and 200 µm wet thicknesses and characterize their optical properties, including emission, absorption, reflectance, and hemispherical light transmittance. A method is presented for quantifying “UV/blue-to-red” spectral conversion efficiency of a luminescent coating. In addition, the B:R ratio of the luminescent coating is characterized using natural sunlight.

5.2. Material and method

5.2.1. Coating preparation

Selected phosphor

The activator-absorption phosphor $Sr_2Si_5N_8:Eu^{2+}$ (SSN:Eu) was acquired from Leuchtstoffwerk Breitungen GmbH. The Eu^{2+} ion is incorporated into the $Sr_2Si_5N_8$ host by substituting Sr site. The actual stoichiometric composition of the SSN:Eu used in this work was $Sr_{1.86}Si_5N_8:Eu_{0.14}{}^{2+}$, determined by energy-dispersive X-ray spectroscopy (JSM-IT100, JEOL). The photoluminescent quantum yield (PLQY) of this phosphor was reported to be 90% by the supplier. The phosphor particle has a size range of 6 to 10 µm. The refractive index (n) of $Sr_2Si_5N_8$ is 2.5 [19].

Luminescent coating's formulation

The luminescent coating consisted of a dispersing agent, defoamer, acrylic resin, thickeners, and the selected phosphor. The loading of phosphors was 9 mass%. The applied wet thickness of coating were 50, 100, 150, 200 µm on a 1 mm thick fused silica substrate by a bar-coater (TQC film applicator, Industrial Physics). The detailed coating formulation is listed in the appendix of Chapter 2.

5.2.2. Characterization Methods

Hemispherical light transmittance

The hemispherical light transmittance of all the coated samples was measured by a tabletop characterization system developed in Chapter 3. The calculation of T_{HEM} considers the wavelength range from 400 nm to 700 nm (PAR). A detailed description of the measurement procedure and calculation can be found in the cited work. Note that the T_{HEM} system employs a tungsten lamp as the light source, which emits mainly within the PAR region. Consequently, the obtained T_{HEM} values reflect not only PAR transmittance but also account for the absorption of blue photons and emission of red photons. The T_{HEM} of 1 mm-thick fused silica substrate was measured to be 87.7%.

Diffuse reflectance

The diffuse reflectance of all coating samples was measured using an integrating sphere (IS2004, Thorlabs) and in combination with a deuterium light source (AvaLight-DH-S, Avantes). The integrating sphere was positioned directly above the coating sample to collect the backward-scattered/reflected light signals from the incident deuterium illumination. A reference measurement was obtained using the same reflective material as the inner surface of the integrating sphere. The value of diffuse reflectance was obtained by taking the average value in the NIR wavelength range (800-850 nm), where neither absorption nor emission occurred. The diffuse reflectance of 1 mm-thick fused silica substrate was measured to be 8.0%.

Direct transmittance

The direct transmittance measurement provided the transmitted light signals of the luminescent coating samples using a deuterium lamp as a light source (AvaLight-DH-S, Avantes). The transmitted signal of a fused-silica substrate $\mathrm{I}_{\mathrm{substrate}}(\lambda)$ and the luminescent coating on the substrate $\mathrm{I}_{\mathrm{coating}}(\lambda)$ were collected by a spectrometer (QE65Pro, Ocean Optics) connected with an optical fiber (FC-UVIR600, Avantes) connected to an integrating sphere (15", Labsphere) located behind the sample. The setup configuration is presented in Fig. 5.1. This detection system was calibrated with a calibrated deuterium light source (UV40, Optronic Laboratories) and a tungsten light source (EV81, EPLAB).

From the direct transmittance measurements, the coating's absorption and emission ranges (and their relative strengths) can be extracted, thereby demonstrating the photoluminescent response of the coating samples under illumination. The "UV/Blue-to-red" spectral conversion efficiency, η_{coating}, quantifies the coating's ability to convert incident UV and blue photons into red photons transmitted into the greenhouse. In other words, η_{coating} is defined as the number of emitted red photons entering the greenhouse per absorbed UV/blue photon, and is given by:

$$\eta_{\mathrm{coating}} = \frac{\int_{550}^{750} [I_{\mathrm{coating}}(\lambda) - C_{\mathrm{Ref}} * I_{\mathrm{substrate}}(\lambda)] d\lambda}{\int_{250}^{550} [C_{\mathrm{Ref}} * I_{\mathrm{substrate}}(\lambda) - I_{\mathrm{coating}}(\lambda)] d\lambda} \tag{5.1}$$

Based on the optical properties of the applied phosphors, the emission range for the coating samples was defined as 550–750 nm, while the absorption range was defined as 250–550 nm. Since $\mathrm{I}_{\mathrm{coating}}(\lambda)$ and $\mathrm{I}_{\mathrm{substrate}}(\lambda)$ are the transmitted signals collected by an integrating sphere, any incident light that is backward scattered or guided to the sample edges may escape detection. This results in an overestimation of UV/blue absorption and an underestimation of red emission. In our measurement configuration, the following equation holds, A=1-T-R-W, in which W equals the guided fraction escaping through the sample edges. Although we measured the backward reflection R (through diffuse reflectance measurement) and direct transmission T, we cannot reliably measure W. Therefore, we have introduced a more practical and reliable metric $\mathrm{C}_{\mathrm{Ref}}$ that takes into account the influence of the backward scattering and waveguiding effects on the loss of incident PAR photon flux. $\mathrm{C}_{\mathrm{Ref}}$ was determined within a near-infrared spectral range (800–850 nm), unaffected by both emission and absorption, which was calculated from the transmittance of the coating sample relative to the uncoated fused silica substrate. A small $\mathrm{C}_{\mathrm{Ref}}$ value represents a substantial light loss from scattering and waveguiding effects. By applying $\mathrm{C}_{\mathrm{Ref}}$, the influence of backward scattering and waveguiding effects can be removed from the calculations of η_{coating}. An assumption of constant backward scattering and waveguiding effects between 250 to 900 nm was made.

Direct transmittance with sunlight illumination

Because a deuterium lamp emits a disproportionately large UV component compared with the AM1.5 solar spectrum, its UV-rich excitation can exaggerate a coating's emission. Results obtained under deuterium illumination are therefore not directly transferable to greenhouse conditions under sunlight. Using the same configuration of direct transmittance with natural sunlight as a light source can provide a clear and visible output. The characterization was performed on a clear, sunny day (April 23rd, 2025) at 14:00 in Delft, The Netherlands. Direct (non-diffuse) sunlight was incident perpendicularly on the luminescent coating sample. Through this measurement, the total PAR flux

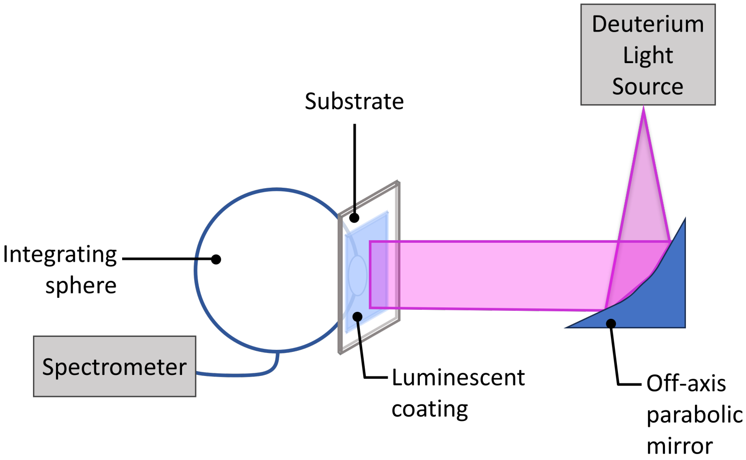

Figure 5.1: Illustration of direct transmittance measurement configuration.

and Blue:Red (B:R) light ratio of the coating samples were determined. The total PAR flux was calculated by integrating the photon flux from 400 to 700 nm. Blue photon flux was integrated over 400–500 nm region, while the red photon flux was integrated over 600–700 nm region. A reference measurement was conducted using an uncoated fused silica substrate.

5.3. Results and discussions

5.3.1. Hemispherical light transmittance and diffuse reflectance

Final appearance of the produced luminescent coating samples are presented in Fig. 5.2. The thickness after drying, T_{HEM}, and diffuse reflectance values of the four luminescent coatings are presented in Table 5.1. After drying, the coating thickness reduced to one-fourth of the wet-applying thickness. Despite the additional red photons generated by the luminescent coatings through conversion of UV/blue photons, the T_{HEM} decreased from 63.9% (50 µm) to 38.2% (200 µm) while the uncoated substrates had 87.7% T_{HEM}. The reduction of the light signal was a combined effect of absorption of blue light, backward scattering (including angular reflectance), and waveguiding effects in the polymer matrix and substrate. To verify that the observed reduction in T_{HEM} arose from the backward scattering effect, diffuse reflectance measurements were performed on the coatings and presented in Table 5.1. Diffuse reflectance rose from 13.5% at 50 µm to 26.3% at 200 µm. This upward trend supports the conclusion that the decline in T_{HEM} is partly due to enhanced backward scattering and confirms that thicker coatings suffer a greater light loss from this effect. The extent of backward scattering is linked to the refractive index of the phosphor, which will be explained in the next section.

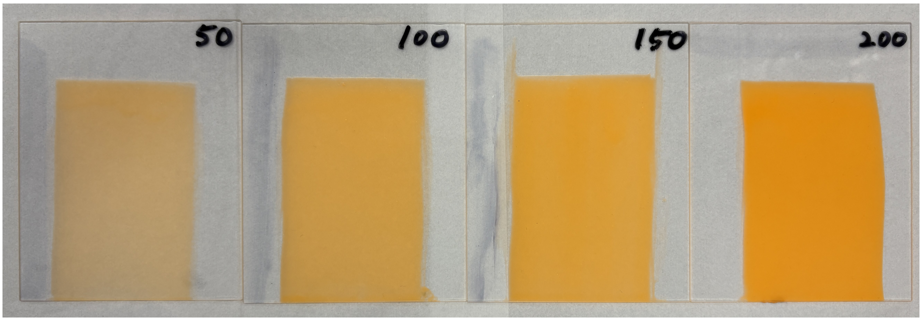

Figure 5.2: Final appearance of the SSN:Eu coatings, which are 50 µm, 100 µm, 150 µm, 200 µm from left to right.

Table 5.1: Dried thickness, T_{HEM}, diffuse reflectance, C_{Ref}, and η_{coating} of the SSN:Eu luminescent coatings.

Sample	Dried thickness (μm)	T_{HEM} (%)	Diffuse reflectance (%)	C_{Ref}	η_{coating} (%)
50 μm	14.0	63.9	13.5	0.85	32.2
100 μm	29.7	52.9	18.3	0.77	34.7
150 μm	40.3	47.9	20.6	0.73	36.0
200 μm	51.7	38.2	26.3	0.65	38.0

5.3.2. Direct transmittance

Figure 5.3 shows the transmitted light signals of all luminescent coatings (I_{coating}) and fused silica substrate ($I_{\mathrm{substrate}}$). The spectrum can be divided into three wavelength intervals. First, the UV/blue range (250–550 nm), where absorption occurred, and the transmitted light signals of the coatings were lower than those of the fused silica. Second, the emission range (550–750 nm), where photoluminescence was observed, and the transmitted signals of the coatings were higher than those of the fused silica. Third, the NIR range (800–850 nm), where neither absorption nor emission occurred.

Figure 5.4 shows the relative absorption and emission intensities of the four luminescent coatings with respect to the fused-silica substrate, as derived from the transmitted-light spectra in Fig. 5.3. Due to a spike in the deuterium lamp output near 660 nm, the derived relative emission spectrum exhibits an artificial sharp dip at 660 nm. Consequently, it should be noted that the calculated "UV/Blue-to-red" spectral-conversion efficiency, η_{coating}, is underestimated for these coating samples.

The absorption and emission spectra were consistent with the photoluminescent characteristics of Eu^{2+} activator ions, which originated from the transition between the ground state $4f^7$ and the excited state $4f^6 5d^1$ [17–20]. Both absorption and emission intensities increased with coating thickness because a thicker coating provides a longer optical path for UV and blue photons to travel through, increasing the probability of absorption and emission.

The C_{Ref} values and the coating's "UV/Blue-to-red" spectral conversion efficiency

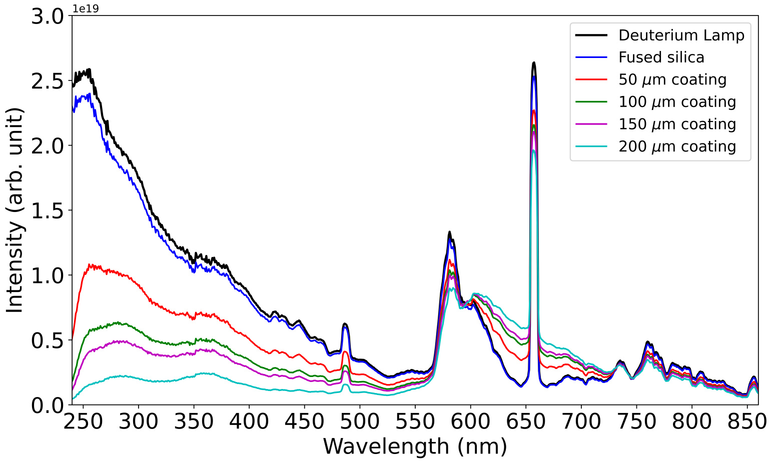

Figure 5.3: The transmitted light signals of the SSN:Eu coatings under illumination of deuterium light source.

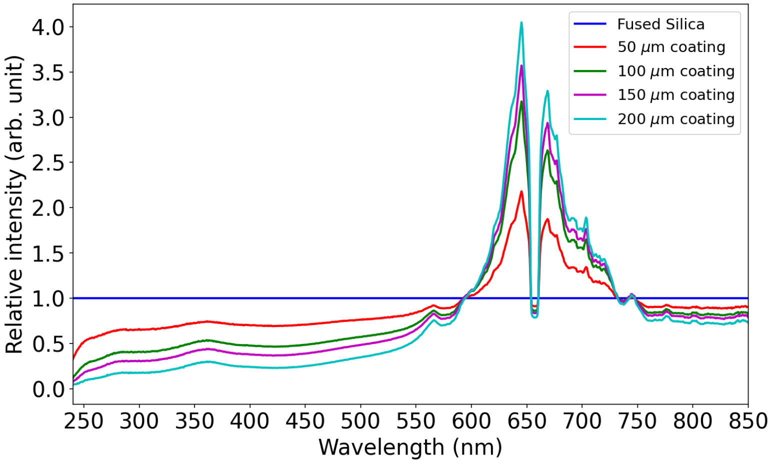

Figure 5.4: The relative intensity of transmitted light signals between SSN:Eu coatings and fused silica substrate. The dip at 660 nm was due to the deuterium lamp spectrum.

$\eta_{coating}$ are presented in Table 5.1. C_{Ref} decreased from 0.85 (50 µm) to 0.65 (200 µm), demonstrating an enhanced light loss from scattering effects as shown in the reduction of T_{HEM} falling from 63.9% (50 µm) to 38.2% (200 µm).

The strong scattering effect was attributed to the high refractive index (n = 2.5) of SSN:Eu. In our previous research (Chapter 4), BAM:Eu, an oxide material, has a lower refractive index (n = 1.7), while ZnS:Ag, a sulphide material, has a higher value (n = 2.3). Under the same 9 mass% particle loading, BAM:Eu coatings displayed C_{Ref} of 0.96

(50 µm) to 0.88 (200 µm), while ZnS:Ag coatings exhibited C_{Ref} of 0.88 (50 µm) to 0.78 (200 µm). The small C_{Ref} values of SSN:Eu coatings, from 0.85 (50 µm) to 0.65 (200 µm), aligned with the conclusion in our previous research that a higher refractive index leads to a higher scattering effect and thus a small C_{Ref} value as well as a large diffuse reflectance. The spectral conversion efficiency, $\eta_{coating}$, exhibited only a weak dependence on film thickness and remained within 32–38%. This behavior is expected for two reasons. First, the spike in the deuterium-lamp output in the direct transmittance measurement introduces an artificial dip near 660 nm in the derived emission spectrum, leading to an underestimation of $\eta_{coating}$. Second, because photoluminescence is emitted isotropically, at most half of the emitted photons propagate toward the integrating sphere and can be collected. As a result, the measurable $\eta_{coating}$ is inherently capped at approximately one-half of the phosphor's PLQY (90%).

5.3.3. Direct transmittance with sunlight illumination

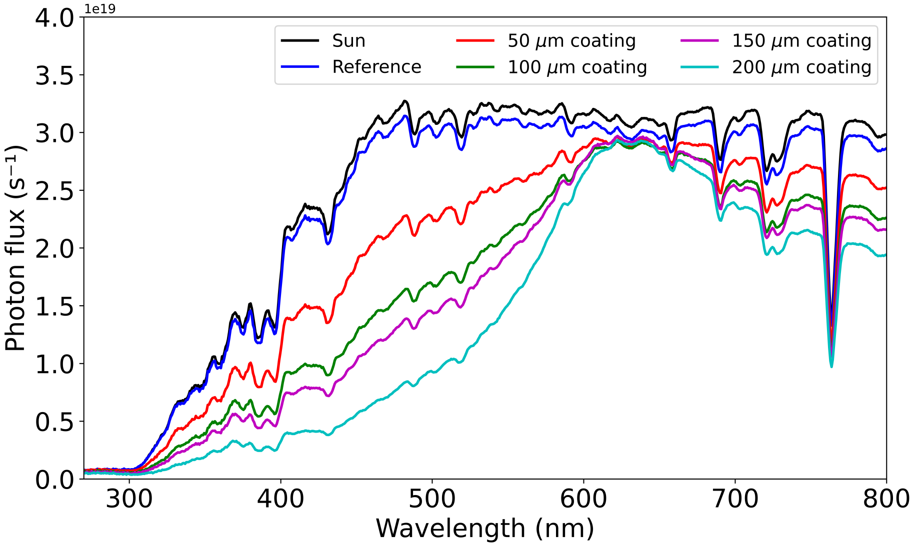

Figure 5.5: The transmitted light signals of the SSN:Eu coatings under illumination of natural sunlight on a clear day.

Figure 5.5 displays the transmitted light signals of the four SSN:Eu luminescent coatings under direct sunlight illumination on a clear day. Applying the SSN:Eu luminescent coatings caused a pronounced net loss of photon flux in the PAR region, most noticeably in the blue range, because of phosphor absorption and backward scattering effects. As coating thickness increased, the blue absorption, backward scattering, and waveguiding effect within the film all intensified, further reducing the total transmitted PAR flux. The fractions of transmitted PAR photons relative to the uncoated fused-silica reference are listed in Table 5.2. Applying the SSN:Eu luminescent coating reduced the total PAR photons from 83.4% for the thinnest film to 57.1% for the thickest. Despite the overall drop in total PAR photons, the absolute red-band photon count was kept at a high level (over 87% absolute red flux of the incident sunlight) across the four coating thicknesses because the absorbed UV/blue photons were re-emitted as red photons. In addition, the SSN:Eu luminescent coatings could shift the B:R ratio from 1:1 to 1:5 by adjusting the coating thickness.

Table 5.2: The transmitted PAR photon flux, and Blue:Red light ratio of the luminescent coatings under direct sunlight illumination.

Sample	PAR (%)	Blue (%)	Red (%)
Fused silica substrate	100.0	45.9	54.1
SSN:Eu 50 μm	83.4	38.1	61.9
SSN:Eu 100 μm	71.6	30.4	69.6
SSN:Eu 150 μm	67.5	26.4	73.6
SSN:Eu 200 μm	57.1	17.3	82.7

5.3.4. Use cases

The optimal balance between blue and red light (B:R ratio) varies depending on plant species and growth stages. For instance, reducing blue-light exposure negatively affects the dry weight of lettuce (Lactuca sativa) [15], but it can enhance both growth and quality in cabbage (Brassica oleracea) [16]. The pronounced red enrichment afforded by applying SSN:Eu phosphor luminescent coatings provides a valuable spectral-management strategy for crops that require high-red-light conditions for optimal growth. To demonstrate their practical value, we present three representative cases in which SSN:Eu coatings can be advantageous.

Dong et al. reported that under the blue:red light ratio of 25:75, the soluble sugar, total soluble solids, glucose, and sucrose contents in the developing tomato (Micro-Tom) were highest [21]. A recent study by Paponov et al. on tomato (Solanum lycopersicum L.) concluded that a Blue:Red ratio of 20:80 was beneficial for overall plant growth. Moreover, it increased the size of fruits in the middle and distal positions of the truss, resulting in a more even size and weight for each fruit. The B:R ratio also increased the root pressure, improving the water supply to the fruits, promoting fruit growth [22]. In a more extreme case, 10% blue and 90% red was the optimal ratio for lettuce (Lactuca sativa var. Youmaicai). Although there were some beneficial effects of a small amount (5-20%) of blue light on the growing stage, such as enhanced photosynthesis rate, the shoot biomass dropped significantly in the case of 25-50% blue light [23]. All the examples demonstrate the potential of applying $Sr_2Si_5N_8$:Eu^{2+} luminescent coating in greenhouse systems.

5.4. Conclusion

$Sr_2Si_5N_8$:Eu^{2+} luminescent coatings with various thicknesses were produced and their optical properties, including transmittance, reflectance, and spectral conversion for greenhouse applications, were successfully characterized. Applying $Sr_2Si_5N_8:Eu^{2+}$ UV/blue-to-red phosphor coatings reduced the total PAR photon flux, primarily due to absorption of blue light (as expected) and strong backward scattering caused by the high refractive index (n=2.5) of the phosphor. Despite the overall loss in PAR region, the $Sr_2Si_5N_8:Eu^{2+}$ luminescent coatings show the capability of modifying the Blue:Red light ratio from 1:1 to 1:5 while keeping more than 87% absolute red-band photon flux of the incident sunlight. This research provides a practical demonstration of light management through spectral shifting for greenhouse systems, indicating the potential to optimize light quality for specific species.

Acknowledgement

The author thanks Dr. Bert Hintzen for his assistance in selecting the phosphor. The author also thanks the students: A. Elerte, Y. ter Denge, I. Oskam, O. van de Rijt for their help in conducting the experiments.

References

[1] L. Marcelis, A. Broekhuijsen, E. Meinen, E. Nijs, M. Raaphorst, Quantification of the growth response to light quantity of greenhouse grown crops, Acta Horticulturae 711 (2006) 97–103.

[2] S. Jakka, M. Silva, M. Soares, K. Pavani, Exploring the potential of Eu^{2+} and Mn^{4+} activated $LaAlO_3$ phosphors as red and far-red emitters for horticulture lighting, RSC Advances 13 (2023) 31314–31320.

[3] C. Cho, G. Bosco, E. van der Kolk, The potential of SiO_2:Al^{3+},Eu^{2+} blue phosphor coatings in greenhouse application, Optical Materials 157 (2024) 2–8.

[4] D. Singh, C. Basu, M. Meinhardt-Wollweber, B. Roth, LEDs for energy efficient greenhouse lighting, Renewable and Sustainable Energy Reviews 49 (2015) 139–147.

[5] J. Nelson, B. Bugbee, Economic analysis of greenhouse lighting: Light emitting diodes vs. high intensity discharge fixtures, PLoS ONE 9 (2014).

[6] J. Blain, A. Gosselin, M. Trudel, Influence of HPS supplementary lighting on growth and yield of greenhouse cucumbers, HortScience 22 (2022) 36–38.

[7] K. Mishra, C. Stanghellini, S. Hemming, Technology and materials for passive manipulation of the solar spectrum in greenhouses, Advanced Sustainable Systems 7 (2023).

[8] Y. Fan, Y. Zhou, Z. Qiu, S. Lian, Photoluminescent materials for solar spectral conversion greenhouse films, Journal of Materials Chemistry C (2025) 5462–5482.

[9] J. Mao, H. Fan, S. Lian, G. Waterhouse, S. Ai, Red luminescent metal–organic framework phosphor enhanced by CaSrS:Cu,Eu for agricultural film, Applied Physics A: Materials Science and Processing 125 (2019) 2–9.

[10] Y. Zhu, Z. Qiu, B. Ai, Y. Lin, W. Zhou, J. Zhang, L. Yu, Q. Mi, S. Lian, Significant improved quantum yields of $CaAl_{12}O_{19}$:Mn^{4+} red phosphor by co-doping Bi^{3+} and B^{3+} ions and dual applications for plant cultivations, Journal of Luminescence 201 (2018).

[11] S. Yang, M. Wu, C. He, Y. Wu, Y. Zhang, J. Yu, High quantum efficiency blue phosphor $K_2SrCa(PO_4)_2$:Eu^{2+} for plant growth, Journal of Alloys and Compounds 989 (2024).

[12] S. Hemming, D. Waaijenberg, G. Bot, P. Sonneveld, F. de Zwart, T. Dueck, C. van Dijk, A. Dieleman, N. Marissen, E. van Rijssel, B. Houter, Optimaal gebruik van natuurlijk licht in de glastuinbouw, Agrotechnology & Food Innovations B.V. (2004) 154.

[13] Y. Liang, C. Kang, E. Kaiser, Y. Kuang, Q. Yang, T. Li, Red/blue light ratios induce morphology and physiology alterations differently in cucumber and tomato, Scientia Horticulturae 281 (2021).

[14] C. Piovene, F. Orsini, S. Bosi, R. Sanoubar, V. Bregola, G. Dinelli, G. Gianquinto, Optimal red: Blue ratio in LED lighting for nutraceutical indoor horticulture, Scientia Horticulturae 193 (2015) 202–208.

[15] H. Saito, H. Shimizu, K. Ohdoi, The effect of light quality on growth of lettuce Yuta, IFAC Proceedings Volumes 43 (2010) 294–298.

[16] K. Demir, G. Sarikamis, G. Seyrek, Effect of LED lights on the growth, nutritional quality and glucosinolate content of broccoli, cabbage and radish microgreens, Food Chemistry 401 (2023).

[17] S. Brinkley, N. Pfaff, K. Denault, Z. Zhang, H. Hintzen, R. Seshadri, S. Nakamura, S. Denbaars, Robust thermal performance of $Sr_2Si_5N_8:Eu^{2+}$: An efficient red emitting phosphor for light emitting diode based white lighting, Applied Physics Letters 99 (2011).

[18] C. Yeh, W. Chen, R. Liu, S. Hu, H. Sheu, J. Chen, H. Hintzen. Origin of Thermal Degradation of $Sr_{2x}Si_5N_8:Eu_x$ Phosphors in Air for Light-Emitting Diodes. Journal of the American Chemical Society 134 (2012) 14108 - 14117.

[19] O. Ten Kate, M. De Jong, H. Hintzen, E. van der Kolk, Efficiency enhancement calculations of state-of-the-art solar cells by luminescent layers with spectral shifting, quantum cutting, and quantum tripling function, Journal of Applied Physics 114 (2013).

[20] Y. Li, J. van Steen, J. van Krevel, G. Botty, A C. Delsing, F. DiSalvo, G. de With, H. Hintzen, Luminescence properties of red-emitting $M_2Si_5N_8:Eu^{2+}$ (M = Ca, Sr, Ba) LED conversion phosphors, Journal of Alloys and Compounds 417 (2006) 273–279.

[21] F. Dong, C. Wang, X. Sun, Z. Bao, C. Dong, C. Sun, Y. Ren, S. Liu, Sugar metabolic changes in protein expression associated with different light quality combinations in tomato fruit, Plant Growth Regulation 88 (2019) 267–282.

[22] M. Paponov, D. Kechasov, J. Lacek, M. Verheul, I. Paponov, Supplemental light-emitting diode inter-lighting increases tomato fruit growth through enhanced photosynthetic light use efficiency and modulated root activity, Frontiers in Plant Science 10 (2020) 1–14.

[23] Y. Tang, S. Guo, W. Ai, L. Qin, Effects of red and blue light emitting diodes (LEDs) on the growth and development of lettuce (var. Youmaicai), SAE Technical Papers 4970 (2009).

[24] J. Mao, H. Fan, S. Lian, G. Waterhouse, S. Ai, Red luminescent metal–organic framework phosphor enhanced by CaSrS:Cu,Eu for agricultural film, Applied Physics A: Materials Science and Processing 125 (2019) 2–9

6

Conclusion

6.1. Concluding Remarks

The goal of this dissertation is to bridge the gap between phosphor research and horticulture and to explore the potential of photoluminescent materials in greenhouse applications. With a growing global population and weather conditions becoming more extreme, securing the food supply is getting more attention. Greenhouse systems have been widely utilized to produce food around the world. Their importance in tackling food insecurity is widely recognized. Crops convert the absorbed photon energy into the chemicals required for growth through photosynthesis. The absorbed photon energy is referred to as photosynthetically active radiation (PAR), which has a defined spectral range from 400 to 700 nm. The concept of "1% extra light can lead to 1% extra yield" is commonly accepted in horticulture. This general rule makes transmittance an important optical property for greenhouse roofing. Apart from transmittance, the scattering property of roofing materials is of vital importance as well. A high-scattering roof can evenly distribute sunlight over the leaves, which avoids light saturation during photosynthesis, keeps leaf temperature lower, and increases light-use efficiency. A phosphor-based luminescent coating can be tailored to meet the optical properties required to enhance crop yield. This research aims to investigate the potential of luminescent materials in greenhouses, which raises three research challenges including a) a lack of physical luminescent coating sample demonstrating the feasibility of this concept, b) a lack of clear and standardized measurable quantities for quantifying how effectively these coatings perform spectral conversion, and c) a lack of equipment to characterize the hemispherical light transmittance properties of coating samples.

The review published by Fan et al. categorizes spectral-conversion greenhouse films for different purposes, such as UV-to-blue or blue-to-NIR, and includes the potential luminescent materials for each function [1]. However, these works did not present definitions and quantification methods for determining the capability of spectral-conversion coatings for greenhouse applications. In **Chapter Two**, a cheap UV-to-blue SiO_2:Al^{3+},Eu^{2+} phosphor was synthesized through a sol-gel process. For 1 mol% Eu^{2+}, a minimum of 4 mol% Al^{3+} is required to avoid Eu^{2+} clustering and minimize energy transfer that causes a red shift due to concentration quenching. The energy-transfer phenomena were confirmed by a rise time in the decay curves of the low-energy Eu^{2+} emission and a short decay time of high-energy Eu^{2+} emissions. The sample SiO_2:$Al_{0.12}Eu_{0.03}$ showed the highest quantum yield of 70%. Apart from the material study, we took the next step in phosphor research for greenhouse applications: a spectral-conversion luminescent greenhouse coating was fabricated. It showed a bright blue emission under UV excitation. In order to quantify the coating's capability to convert UV to extra PAR, several coating performance indicators, including a correction factor C_{Ref}, conversion efficiency $\eta_{coating}$, absorption spectrum $A_{coating}(\lambda)$, and PAR Enhancement were proposed. These performance indicators can be determined using any type of lamp with UV emission, an integrating sphere, and a spectrometer, and it serves as a tool for other researchers to assess a coating's UV-to-PAR performance quantitatively and go beyond presenting the concept.

Since sunlight rarely enters greenhouse roofing with a perfect 0-degree angle of incidence (AOI), hemispherical light transmittance (T_{HEM}) is the generally accepted quantity replacing direct transmittance measurements in the Netherlands. T_{HEM} integrates not only the transmittance from 0 to 90 degrees AOI but also the relative solar spectral radiation density and relative plant sensitivity functions. The currently available T_{HEM} characterization system, Transvision, developed by Wageningen University and Research (WUR), features a 1-meter integrating sphere; therefore, it requires a sample size of at least 200 cm^2. This size requirement, together with extra work and waiting time to characterize samples, hinder research progress in functional roofing materials. In **Chapter Three**, a tabletop setup that can characterize T_{HEM} for small-scale samples was designed, built, and systematically studied. To obtain a stable output, the integrating sphere sample port edge thickness should be minimized to avoid light scattering at high incident angles, which cannot be corrected by a double-beam measurement. The port's opening area should be smaller than 1% of the sphere's surface area so that less light can escape from the sphere which leads to measurement errors. Although this error can be eliminated by a double-beam measurement, a larger port requires a larger correction, which is not favored. Furthermore, the cross-section of the incident beam should be at least 50% larger than the port‘s opening area to obtain a stable output. A commercial sample was used to benchmark this tabletop setup, and the results were compared with those characterized by WUR. A 20-time repeat measurement demonstrated a stable output with a standard deviation of 0.05% and good agreement between our setup and the WUR Transvision system, showing only a 1% difference in T_{HEM}. The tabletop system showed its feasibility for characterizing small-scale uniform samples with high accuracy. The development of this tabletop system accelerates the research progress of advanced greenhouse roofing.

In Chapter One, the first greenhouse luminescent coating was fabricated using a phosphor synthesized in our group. As phosphors have been studied for many decades, there are currently hundreds of commercially available phosphors. Investigating luminescent greenhouse coatings produced by existing commercial phosphors can speed up research progress because commercial phosphors are usually fully optimized for the best photoluminescent properties. Commercial phosphors fall into two main categories: “activator-absorption” and “host-absorption.” Photon energy is absorbed by electrons through transitions from the ground state to the excited state in activator ions, or through transitions from the valence band to the conduction band in the host lattice.

In **Chapter Four**, we fabricated luminescent coatings using these two types of commercially available phosphors, $BaMgAl_{10}O_{17}:Eu^{2+}$ (activator-absorption) and ZnS:Ag (host-absorption), and investigated their differences in optical properties, such as excitation, emission, quantum yield, absorption, and greenhouse performance indicators listed in Chapter Two. The absorption strength of the coatings increased with higher mass loading and larger coating thickness, following approximately the Beer-Lambert law despite strong scattering besides absorption. Interestingly, although the absorption coefficient of host-absorption phosphors is two orders of magnitude larger than that of activator-absorption phosphors, the final coating's absorption strength did not show such a large difference. This is mainly because the phosphor particle size provides a long absorption path for photons. The highest PAR Enhancement, 1.3%, was achieved with a 200 μm thick 18 mass% ZnS:Ag coating. However, such high PAR Enhancement was accompanied by considerable backward scattering, which reduced the hemispherical light transmittance and the total transmitted PAR flux. Backward scattering can be potentially lowered by employing larger particles that favour forward scattering as predicted by Mie theory, or particles with a radius much smaller than the wavelength of light. Engineering the coating's polymer matrix, such as refractive index matching or applying anti-reflection layer can also lower the backward scattering effect. The optimization of luminescent coating is not a single approach; for example, reducing particle size may necessitate particle loading to achieve enough absorption. Significantly reducing scattering strength without affecting or preferably even increasing absorption strength should be the focus of future research.

Throughout the research, it was found that the concept of UV-to-PAR is restricted by the small fraction of UV in the AM1.5 solar spectrum. The accompanying scattering loss is greater than the enhanced PAR flux in greenhouses. To further expand the potential of phosphor-based luminescent coatings, a demonstration of greenhouse spectral quality control using a UV/blue-absorbing and red-emitting phosphor is presented in **Chapter Five**. Luminescent coatings based on a commercial phosphor, $Sr_2Si_5N_8:Eu^{2+}$, which absorbs both UV and blue radiation (250–550 nm) and emits red light (550–750 nm), was fabricated to assess their capability for spectral control. The coating's optical properties were studied using the method and definitions explained in Chapters Two and Four. Specifically, we characterized the coating with a direct-transmittance setup using natural sunlight as a light source, which provides a direct and intuitive output of the spectral quality when applying such a coating in a greenhouse. Such UV/blue-absorbing luminescent coating reduces total PAR flux by 40% and T_{HEM} by 60% due to absorption and strong backward scattering. However, the absolute photon flux of the red band (600–700 nm) remained at 87% of the incident sunlight, but, more importantly, the Blue:Red ratio of the obtained spectrum can be manipulated from 1:1 to 1:5. The $Sr_2Si_5N_8:Eu^{2+}$ luminescent coating is beneficial for crops requiring a rich red-light environment in an area that is full of sunshine, such as Spain or Africa.

The overarching conclusion of this work is that UV-to-PAR conversion in an optimized phosphor layer can closely approach the theoretical maximum of approximately 3.5%, but it cannot offset the order-of-magnitude higher loss of PAR caused by backward scattering unless specific strategies are developed to reduce scattering losses. Instead, phosphor-based particle coatings can be most fruitfully applied when the goal is to modify the greenhouse light color ratio rather than to maximize the absolute PAR level.

6.2. Future research directions

6.2.1. Commercial Phosphors for greenhouse applications

Phosphors have been investigated for several decades; consequently, many have already been optimized and commercially produced in large quantities. This dissertation examines only three commercial phosphors for greenhouse applications: $BaMgAl_{10}O_{17}:Eu^{2+}$, ZnS:Ag, and $Sr_2Si_5N_8:Eu^{2+}$. Nevertheless, numerous other phosphors are available that enable different spectral conversion functions, such as UV-to-green, blue-to-red, and UV-to-NIR. Another important advantage of using commercial phosphors in greenhouse applications is that they are typically mass-produced and therefore less expensive than developing and commercializing new phosphors from scratch. Shabalina et al. reviewed spectral conversion coatings and films based on commercial luminescent agents, including quantum dots and carbon dots [2]. With the methods presented in this dissertation, the spectral conversion (not limited to UV-to-PAR) performance of such coatings and films can be quantified readily for greenhouse use. Investigating readily available phosphors thus accelerates research and prevents redundant resource expenditure.

6.2.2. Luminescent films/foils

The luminescent coatings examined in this dissertation are designed for glass greenhouses, which predominate in the Netherlands, other Northern European countries, and North America. Applying such a coating to glass glazing allows active manipulation of the spectrum entering the structure without the need of installing new glass. Glass greenhouses, however, are far more expensive than plastic-covered greenhouses, the most common greenhouse type worldwide. Future research could therefore investigate incorporating phosphor particles into “luminescent films/foils” that directly replace the white covers of plastic greenhouses or are placed between the roof and the crop canopy as an extra layer. This concept is considered by start-ups such as UbiGro and LLEAF, which use quantum dots as luminescent agents. Inorganic-based phosphors have much better stability and a lower production cost than quantum dots [3, 4].

6.2.3. Hortiscatter

Plants prefer a scattered-light environment over direct light because diffuse illumination is distributed more evenly across the foliage, reducing photosynthetic saturation and increasing light-use efficiency. The degree of light scattering, formally termed Hortiscatter, has been shown to promote plant growth: every additional 10% of Hortiscatter can raise crop yield by 1.8–2.2% [5]. A particle-based luminescent coating with high Hortiscatter could therefore boost yields through both spectral conversion and enhanced scattering. This avenue merits further study, as scattering can be tuned by adjusting particle size, shape, and loading [6]. In addition, the characterization of Hortiscatter is difficult and not easily accessible. Future research can focus on the development of an accessible and reliable Hortiscatter characterization system to advance greenhouse roofing.

References

[1] Y. Fan, Y. Zhou, Z. Qiu, S. Lian, Photoluminescent materials for solar spectral conversion greenhouse films, Journal of Materials Chemistry C (2025) 5462–5482.

[2] A. Shabalina, V. Kozlov, M. Paskhin, I. Popov, S. Gudkov, A mini-review of photoconversion covers for greenhouses: Assessment parameters and plant experiment results, Horticulturae 11 (2025) 680.

[3] L. Shen, X. Yin, Solar spectral management for natural photosynthesis: from photonics designs to potential applications, Nano Convergence 9 (2022).

[4] D. Hebert, J. Boonekamp, C. Parrish, K. Ramasamy, N. Sakarov, C. Castanede, L. Schuddebeurs, H. McDaniel, M. Bergren, Luminescent quantum dot films improve light use efficiency and crop quality in greenhouse horticulture, Frontiers in Chemistry 10 (2022) 1-12.

[5] G. van Steekelenburg, S. Hemming, E. Kaiser, E. Heuvelink, Quantifying the effects of hortiscatter in greenhouse cover materials on crop yield, Acta Horticulturae 1423 (2025) 87–94.

[6] J. Meyer-Arendt, Introduction to classical and modern optics, Englewood Cliffs (1972).

Summary

This research aims to investigate the potential of utilizing particle-based luminescent coatings for light management in greenhouses. Light management includes solar spectral conversion, transmittance, and scattering. Phosphor materials perform energy conversion from high-energy radiation to low-energy radiation through photoluminescent mechanisms. These phosphor materials are applied in the form of a sprayable coating intended to be employed on greenhouse roofing. Through energy conversion, a luminescent phosphor coating can achieve spectral conversion, adding light for crop growth, and will at the same time affect both light transmittance and scattering in greenhouse roofing. The application of phosphors as luminescent coatings on greenhouse roofing is a young research topic with very few published results; therefore, it presents several research challenges. The first is the lack of practical work on luminescent greenhouse coatings, demonstrating what type of spectral conversion is beneficial to plants and even the general feasibility of phosphors for greenhouse applications. The second challenge is to define clear and standardized measurable quantities that determine the success of a greenhouse coating, for example, the coating's UV-to-PAR conversion efficiency. The third challenge is to design and build a measuring system that can characterize these quantities, especially the hemispherical light transmittance of small-scale luminescent coating samples.

The first research challenge of demonstrating a phosphor-based greenhouse coating is addressed in Chapter Two: the first luminescent greenhouse coating based on a cheap and scalable Eu^{2+}/Al^{3+}-doped SiO_2 phosphor was manufactured and optimized. A significant increase in the solubility of Eu^{2+} in the SiO_2 host was achieved. For every 1 mol% of Eu^{2+}, at least 4 mol% of Al^{3+} is required to avoid concentration quenching of Eu^{2+}. Such an optimization ratio holds up to 3 mol% of Eu^{2+} being applied in the SiO_2 host. A luminescent greenhouse coating using this phosphor and polymer matrix materials was fabricated. Several indicators were developed to assess the optical properties of this coating for greenhouse applications, including the coating's absorption spectrum, the UV-to-PAR conversion efficiency and the PAR Enhancement, tackling the second challenge. These indicators can be determined through a direct transmittance setup using a deuterium lamp, an integrating sphere, and a spectrometer. The $SiO_2{:}Al^{3+},Eu^{2+}$ phosphor coating provides 0.3% PAR Enhancement and demonstrates the application of a phosphor as a greenhouse luminescent coating.

The hemispherical light transmittance (T_{HEM}) of roofing material is important to greenhouse light management because it directly impacts the PAR flux arriving at leaves. A tabletop T_{HEM} characterization system for small-scale samples was developed and presented in Chapter Three to tackle the third research challenge. Several design parameters of the setup, including port-to-sphere surface area ratio, port edge thickness, and beam-to-port area ratio, were systematically adjusted to study their influence on the

measurement accuracy of a benchmark sample. It was found that the port surface area of the tabletop system should stay below 1% of the total sphere area with a wall thickness as thin as possible (smaller than 1 mm). Furthermore, the light beam should be at least 50% larger than the port opening area. This tabletop system allows researchers to characterize T_{HEM} of small research samples and offers the possibility of reducing the required sample size compared to the over 200 cm^2 needed by the current characterization system, while providing a cheap, quick, and easy means to characterize their own samples. This work provides clarifications that improve the interpretability and practical implementation of NEN2675 C1:2018.

To further address the first challenge of demonstrating phosphor-based greenhouse coatings, a comparison of utilizing host-absorption phosphors and activator-absorption phosphors in greenhouse luminescent coatings with varying coating thicknesses and particle loadings for UV-to-PAR applications is conducted in Chapter Four. The results demonstrate that although the intrinsic absorption coefficient of $BaMgAl_{10}O_{17}:Eu^{2+}$ (BAM:Eu) is two orders of magnitude smaller than that of ZnS:Ag, the observed UV absorption difference between BAM:Eu coatings and ZnS:Ag coatings is smaller than an order of magnitude due to the large particle size providing a long absorption path for UV radiation in the BAM:Eu phosphor. Despite the 1.3% PAR Enhancement observed for the 200 μm thick 18 mass% ZnS:Ag coating, this increase should be compared with a decline of T_{HEM} from 87% to 40% due to backward scattering. Besides absorption strength and photoluminescent quantum yield, the refractive index of the applied phosphor should be considered when selecting candidates for greenhouse applications. For the same 18 mass%, the diffuse reflectance of BAM:Eu ($n \approx 1.7$) increased from 11% to 15%, while that of ZnS:Ag ($n \approx 2.3$) increased from 14% to 26% when the coating thickness was increased from 50 to 200 μm. This result demonstrates that a higher refractive index contributes to larger backward scattering and reduced total transmitted PAR flux.

The research from horticultural science indicates that a high flux of red light (600–700 nm) is more beneficial for plant growth than blue light (400–500 nm). In addition, the UV-to-PAR concept was limited to the small fraction of UV in the AM1.5 spectrum. This inspires the utilization of a $Sr_2Si_5N_8:Eu^{2+}$ (SSN:Eu) phosphor in a coating that can convert UV/blue to red light and further demonstrates different types of spectral conversion greenhouse coatings. As presented in Chapter Five, the T_{HEM} of the SSN:Eu coating dropped from 64% to 38% due to its high backward scattering problem, in accordance with previous results. Despite the large reduction in T_{HEM}, the results show the capability of the SSN:Eu coating in spectral conversion and manipulation. The Blue:Red (B:R) light ratio can be adjusted from 1:1 to 1:5 while maintaining a high red light absolute flux (≈ 87%) compared to the incident sunlight. The results demonstrate the feasibility of phosphor-based luminescent coatings to adjust the spectral quality of greenhouses in areas full of sunshine, such as the Mediterranean region.

In this research, we pioneered the production of phosphor-based greenhouse luminescent coatings and established indicators to evaluate the coating's performance in UV-to-PAR spectral conversion functions. Besides the introduction of performance indicators, a tabletop experimental system was developed to assess T_{HEM} of small-scale samples. Finally, we demonstrated the spectral influence of using different types of phosphors in greenhouse luminescent coatings and provided guidance for selecting phosphors. This research bridges the gap between phosphor technology/materials and its emerging application in horticulture by providing materials research, establishing definitions of easily measurable quantities, and developing a characterization system.

Samenvatting

De focus van dit onderzoek ligt op het bestuderen van de applicatie van deeltjes bevattende luminescerende coatings voor lichtbeheer in kassen. Onder het begrip lichtbeheer valt zowel omzetting van het zonnespectrum, als de transmissie en verstrooiing van fotonen. De omzetting van hoog naar laag energetische straling vindt plaats in fosforen door middel van fotoluminescentie. Deze fosforen kunnen worden aangebracht op het dak van een kas in de vorm van spuitbare coatings. Eenmaal aangebracht kan de desbetreffende coating, dankzij spectrale omzetting van zonlicht, extra licht voor gewasgroei genereren. De coating kan tegelijkertijd worden gebruikt voor het beïnvloeden van zowel de transmissie als verstrooiing van het invallende zonlicht. Onderzoek naar luminescerende kasdakcoatings staat nog in zijn kinderschoenen; het aantal gepubliceerde resultaten is miniem. Dit brengt dan ook een aantal uitdagingen met zich mee. Ten eerste, het gebrek aan experimenteel werk wat aantoont welke vorm van spectrale conversie het gunstigst is voor planten. Tevens ontbreekt ook een algemene haalbaarheidsstudie voor de applicatie van luminescerende coatings in glastuinbouw. De tweede uitdaging is het ontbreken van een meetstandaard voor het beschrijven van de prestaties van een dergelijke coating, denk hierbij aan de UV-naar-PAR omzettingsefficiëntie. De laatste uitdaging betreft het ontwerpen en realiseren van een opstelling die deze meetstandaard vervolgens ook daadwerkelijk kan meten, met name de hemisferische lichttransmissie van kleine coatingmonsters.

De eerste uitdaging, het demonstreren van een luminescerende coating voor kas daken, wordt behandeld in Hoofdstuk 2. In dit hoofdstuk wordt een goedkope doch schaalbare fosforcoating van Eu^{2+}/Al^{3+} gedoteerd SiO_2 zowel gefabriceerd als geoptimaliseerd. Dit laatste heeft dan ook geleid tot een significante toename van de oplosbaarheid van Eu^{2+} in het SiO_2 gastrooster. Voor elk mol% Eu^{2+} dat wordt toegevoegd aan het SiO_2 gastrooster dient op zijn minst 4 mol% Al^{3+} te worden toegevoegd ter voorkoming van concentratiedoving van de Eu^{2+} emissie. Deze ratio blijft geldig tot een doteringspercentagevan 3 mol% Eu^{2+}. Het geoptimaliseerde fosformateriaal is, in combinatie met een polymeer, gebruikt voor de fabricage van een kasdakcoating. Tevens zijn verscheidenen indicatoren ontwikkeld ter evaluatie van de optische eigenschappen van de coating. Hieronder vallen het absorptiespectrum van de coating, de UV-naar-PAR omzettingsefficiëntie, en de PAR-versterkingsgraad. Dit ten behoeve van het aanpakken van de tweede uitdaging. De voorgenoemde indicatoren kunnen worden bepaald met behulp van een directe transmissie opstelling bestaande uit een deuteriumlamp, integrerende bol en een fotospectrometer. Voor de op $SiO_2{:}Al^{3+},Eu^{2+}$ gebaseerde fosforcoating werd een PAR-versterkingsgraad van 0.3% gevonden. Dit demonstreert dan ook de potentiële toepassing van luminiscerende coatings in glastuinbouw.

De hemisferische lichttransmissie (T_{HEM}) van het kasdak is een belangrijke parameter in het lichtbeheer van een kas. Het heeft een directe invloed op de PAR-flux die het blad

van de gewassen bereikt. In Hoofdstuk 3 wordt een compacte opstelling gepresenteerd voor de bepaling van de hemisferische lichttransmissie van kleine onderzoeksmonsters. Dit biedt dan ook een oplossing voor de derde uitdaging. Voor de realisatie van de opstelling zijn een aantal ontwerpparameters systematisch onderzocht om hun invloed op de meetnauwkeurigheid van een referentie coatingmonster in kaart te brengen. De onderzochte parameters zijn: de verhouding tussen de grootte van de opening in de integrerende bol en de grootte van de bol zelf, de dikte van de wand van de bol rond de opening en de verhouding tussen de grootte van de lichtbundel en de opening. Uit dit onderzoek is gebleken dat de grootte van de opening in de integrerende bol minder dan 1% van het totale oppervlak dient te omvatten. De wanddikte rond de opening dient zo klein mogelijk zijn, idealiter kleiner dan 1 mm. Tot slot dient de lichtbundel op zijn minst 50% groter te zijn dan de opening in de integrerende bol. De ontworpen opstelling stelt onderzoekers in staat om T_{HEM} te bepalen voor kleine onderzoeksmonsters. Het biedt de mogelijkheid om met onderzoeksmonsters kleiner dan 200 cm^2 te werken, wat een vereiste is voor het huidige system van de WUR. De nieuwe opstelling zorgt voor een goedkope, snelle, en makkelijke manier voor het karakteriseren van onderzoeksmonsters.

In Hoofdstuk 4 komen we terug bij de eerste onderzoeksvraag. In dit hoofdstuk wordt een vergelijking gemaakt tussen coatings bestaande uit fosforen die zonlicht absorberen door transities in het gastrooster en fosforen waar absorptie plaatsvindt door transities in een activator ion. Voor dit doel zijn coatings geproduceerd met variërende dikte en toegevoegde hoeveelheden fosfordeeltjes. Het is gebleken dat hoewel de intrinsieke absorptie coëfficiënt van $\mathrm{BaMgAl_{10}O_{17}{:}Eu^{2+}}$ (BAM:Eu) honderd keer kleiner is dan die van ZnS:Ag, het geobserveerde verschil in UV-absorptie tussen de twee coatings minder dan een factor tien is. Dit verschil wordt toegeschreven aan de grotere deeltjes in de op BAM:Eu gebaseerde coating, wat resulteert in een langer absorptie padlengte voor UV-straling. De 1.3% PAR-versterkingsgraad van de 200 micron dikke 18 mass% ZnS:Ag coating moet vergeleken worden met de T_{HEM} van deze coating. Dit laat namelijk een afname van 87 naar 40% zien, toegeschreven aan terugverstrooiing. Naast absorptiesterkte en fotoluminescente kwantumrendement moet ook de brekingsindex van de gebruikte fosfor in acht worden genomen in het selectieproces. Voor de 18 mass% BAM:Eu ($n \approx 1{,}7$) coating neemt de diffuse reflectie toe van 11 naar 15%, terwijl die van de ZnS:Ag ($n \approx 2{,}3$) coating toeneemt van 14 naar 26% als de coating dikte wordt veranderd van 50 naar 200 micron. Dit demonstreert dat een hogere brekingsindex bijdraagt aan grotere terugverstrooiing en een lagere totale doorgelaten PAR flux van de coating.

Onderzoek uit de tuinbouwwetenschap geeft aan dat een hoge flux van rood licht (600–700 nm) gunstiger is voor plantengroei dan blauw licht (400–500 nm). Dit vormt dan ook de inspiratie voor het gebruik van een op $\mathrm{Sr_2Si_5N_8{:}Eu^{2+}}$ (SSN:Eu) gebaseerde coating voor het omzetten van UV/blauw licht naar rood licht. Deze coating kan gebruikt worden voor het aantonen van een ander type spectrale conversie. Zoals gepresenteerd in Hoofdstuk 5, daalde T_{HEM} van de SSN:Eu coating van 64 naar 38% door een hoge mate van terugverstrooiing. Dit is in overeenstemming met eerder gepresenteerde resultaten. Ondanks de grote daling in T_{HEM} toont dit aan dat het mogelijk is om een SSN:Eu coating te gebruiken voor spectrale conversie en manipulatie. De blauw:rood (B:R)-lichtverhouding kan worden aangepast van 1:1 naar 1:5, terwijl een hoge absolute flux (≈ 87%) rood licht behouden blijft ten opzichte van de invallende zonneflux. Deze resultaten laten de haalbaarheid zien van een op fosforen gebaseerde luminiscente coating om de spectrale kwaliteit van kassen te regelen in gebieden met een hoge zonlichtintensiteit, denkt u hierbij aan bijvoorbeeld het Middellandse Zeegebied.

In dit onderzoek hebben wij als eersten de productie van op fosfor gebaseerde luminescente kasdakcoatings gerealiseerd en indicatoren vastgesteld om de prestaties van deze coatings in UV-naar-PAR spectrale omzetting te kunnen evalueren. Naast de introductie van prestatie-indicatoren is een opstelling ontwikkeld om de UV-naar-PAR omzettingsefficiëntie, PAR-versterkingsgraad en T_{HEM} van kleinschalige monsters te beoordelen. Tot slot hebben we het spectrale effect van verschillende typen fosforen in luminescente kasdakcoatings aangetoond en richtlijnen gepresenteerd voor de selectie van fosforen. Dit onderzoek overbrugt de kloof tussen fosfortechnologie/-materialen en de opkomende toepassing in de glastuinbouw, door materiaalkundig onderzoek te leveren, duidelijke definities van eenvoudige meetstandaarden op te stellen en een karakteriseringssysteem te ontwikkelen.

Acknowledgements

"Trust in the Lord with all your heart and lean not on your own understanding; in all your ways submit to Him, and He will make your paths straight." — Proverbs 3:5–6

Although I usually prefer to express my gratitude in person, I would like to take this opportunity to thank everyone who has supported me throughout my PhD journey.

First and foremost, I would like to express my deepest gratitude to my daily supervisor, **Erik**. You are a truly kind, patient, and open-minded mentor. I still remember our very first online meeting and, more importantly, the help, encouragement, and support you gave me during some of the most difficult moments of my PhD. Compared to many other PhD-supervisor relationships, I have been extremely fortunate that I could always reach out to you, whether it was about research problems or personal matters. Our communication is always relaxed, natural, and full of mutual respect. It has been my great privilege to be your student.

Next, I would like to thank **Pieter**, the wise leader of the LM group. You are an inspiring scientist whose contributions to luminescent materials are profound. Despite your vast experience, you are always generous in sharing your knowledge and answering even the most basic questions with patience and enthusiasm. You are, in many ways, our group's own "ChatGPT". You also created a warm and inclusive atmosphere through our daily Koffie Tijd, where we could talk not only about science but also about life, holidays, and history. Thank you sincerely for your guidance on my thesis and for being a true mentor.

Bert, our talkative researcher, you always view research from an industrial perspective and offer practical insights and support. Thanks to your professional connections, I was able to publish my third paper. Although we didn't meet very often, every conversation with you was inspiring and full of new ideas. Thank you for your interest in and knowledge about Taiwan, and for inviting scientists from industry to share their experiences with our group.

Speaking of the LM group, none of us could ever forget **Johan**, our most beloved technician. Your expertise in instrument operation, assembly, and design has been indispensable, from knowing where every small screw is stored to designing entire experimental systems from scratch. We all rely heavily on your knowledge and skills. Every time before you go on vacation, the students do their best to make sure the instruments will keep working while you're away, though sometimes we wonder if you secretly have a button that causes problems the moment your vacation starts. Do you? Thank you for helping me design the setup I needed; without you, my second publication would not have been possible. My gratitude also goes to **Trudy**, our secretary. Since you moved to your new office, we haven't met each other as often, yet whenever I encountered administrative issues, you were always there to help, even expediting my visa renewal. Thank you for your kindness and support.

Now, to my fellow LM group members: **Max**, you are one of the most unique and chill people I know. You always brought us together from the game of GO, GameStop, to AMC, and Friday drinks at RID. Thank you for making workdays brighter and for keeping our group connected. I wish you all the best in this new chapter of life with **Dimitra**. **Casper**, our coolest member and also the most thoughtful one. Thank you for answering my endless beginner-level questions, even multiple times, and for all the help you gave me during my thesis writing. I truly appreciate it. By the way, for our next trip, we can either rent a car or take the train, your call. **Jasper**, you are the first European I've met who loves tea even more than I do. I will always cherish those afternoon tea moments after lunch when we shared stories and laughed together. You are truly the man of culture. Thank you for your help in research and for teaming up with me to bother Casper and annoy him all the time. **Jeffrey**, among all of us, you have the most profound understanding of luminescent materials. From you, I learned to analyze research results from a more critical and scientific perspective. I wish you all the best in your final PhD year. **Henry**, **Jakob**, and **Julian**, although we didn't have many chances to work closely, I can tell you all are kind and friendly people, and we could have more fun together. I wish you success in your research and hope you'll continue supporting each other as colleagues and friends.

David, my favorite German colleague. Thank you for your kindness and gentleness toward everyone, whether it's offering snacks or simply greeting people with a warm smile. Please remember to be kind to yourself, too. And by the way, no matter how many times you ask, I am fine with the chocolate, thank you. **Jack**, I hate that every time you come by, my computer screen just happens to show something not research-related. I'm convinced you do it on purpose. You're nice, easy-going, and always yourself. Thanks, mate. **Mark**, the strongest PhD student at RID. I still remember the big smile on your face when we first talked about Federweisser. I wish you continued success in your PhD and enough time to stay strong, both academically and physically.

Giacomo, from our collaboration across the LM group, Physee, and Fotoniq, you have been one of the most inspiring people outside my supervisors. Thank you for all the fruitful discussions and guidance. I wish you success with your new project, and may little **Yara** grow up healthily and happily. **Joe**, you are the starting point of my entire PhD journey. Without your introduction, I wouldn't be here today. Thank you for recommending me and for inviting me to dinner. I want that three-cup chicken again!

I also want to thank my fellow TU Delft PhD friends — **Xiaolin He**, **Yueer**, **Xiaolin Wu**, and **Junhan**, for your valuable advice and help throughout these years. Your support made my Ph.D. and daily life here much smoother. To the Delft Taiwan PhD/PostDoc community — **Yufan**, **Emeline**, **Cinco**, **Queenie**, **Peiyu**, **Zack**, thank you for all our dinners together, where we shared life, research, frustrations, and laughter. I want more hot-pot dinner.

To my **2021 TUD squad** — **Josh**, **Lia**, **Chaya**, **Pinyu**, **Guanwei**, **Florence**, and **Jeff**, our gatherings have evolved from late-night parties to early bedtimes because, well, we've entered a new stage of life. Delft would have been much duller without you all. Thank you for the care and companionship. And **Jeff**, one day, we all will visit your beach villa house in California.

To my **Grandma's home family** — **Gary**, **Julie**, **Anny**, **Phoebe**, **Jinsen**, **Jessie**, **Chiachi**, and **Jeffrey**, every dinner with you made me laugh so hard that I aged three years afterward. You've brought so much color and joy to my life in the Netherlands and made the Dutch winters feel warm. Thank you all.

To my beloved friends who have accompanied me from Germany to the Netherlands, **Joe**, **Tim**, **Ting-Ting**, and **Wei-Wei**, thank you for supporting me emotionally, and for sharing all those unforgettable trips to Portugal, Spain, and Egypt. Let's continue exploring the world together.

I would also like to express my heartfelt gratitude to my family and friends in Taiwan. To my father, thank you for your constant support and prayers, for trusting me and allowing me to freely pursue what I love. To my sister, thank you for carrying the responsibility of taking care of our family during the night years I've been abroad. Without you, I could not have stayed here for such a long time.

I also want to thank myself for persevering through countless sleepless nights, rejected papers, and moments of self-doubt, and for never giving up until this thesis is completed.

Finally, I want to thank **God**. Without His grace and guidance, I would not have made it this far. All glory be to Him.

About the author

Chun-Ting Cho was born on 26th February 1995 in Tainan City, Taiwan. He completed his secondary education at Tainan First Senior High School. In 2013, he enrolled in the Department of Materials Science and Engineering at National Cheng Kung University. During his bachelor's studies, he noticed that most of the senior students joined semiconductor companies for high salaries but enjoyed a limited quality of life. At that time, he decided do something different from his schoolmates. In the final year of his bachelor's studies, he applied to Friedrich-Alexander-Universität Erlangen-Nürnberg for the master's program in Advanced Materials and Processes. During the COVID-19 pandemic, he obtained his MSc degree and faced a career decision: stay in Europe or return to Taiwan. After seven months of job searching, he received the opportunity to pursue a PhD under the supervision of Dr. Erik van der Kolk and Prof. Dr. Pieter Dorenbos, investigating the application of phosphors in greenhouse horticulture.

List of Publications

1. **Chun-Ting Cho**, Giacomo Bosco, Erik van der Kolk, "The potential of SiO_2:Al^{3+},Eu^{2+} blue phosphor coatings in greenhouse application", Opt. Mater. 157 (2024) 116047.
2. **Chun-Ting Cho**, Johan de Haas, Erik van der Kolk, "Design of tabletop hemispherical light transmittance characterization system for small scale samples", SMART AGR TECHNOL. 11 (2025) 100936.
3. **Chun-Ting Cho**, Iris Oskam, Yuri ter Denge, Agnese Elerte, Olav van de Rijt, Bert Hintzen, Erik van der Kolk, "Investigating Solar Spectrum-Shifting Greenhouse Roofing for Enhancing Crop Performance", Acta Horticulturae (2025).
4. Marco Locarno, Qiangrui Dong, Xin Meng, Cristiano Glessi, Nynke Marije Hettema, Nidas Brandsma, Sebbe Blokhuizen, Alejandro Castañeda Garcia, Srividya Ganapathy, Marco Post, Thieme Schmidt, Lars van Roemburg, Bing Xu, **Chun-Ting Cho**, Liedewij Laan, Miao-Ping Chien, Daan Brinks, "Plasmonic Enhancement of Protein Function", in preparation.


TU Delft